Tokyo University of Agriculture and Technology

Thesis for Doctor of Engineering

Development of analysis method of the size distribution and dispersion control in a liquid phase for nano-precipitates in steels

2020.3

Daisuke Itabashi

Contents

Abstract

Formation process of fine nanoparticles and sub-micrometer scaled particles which are called as precipitate in steel are used for the control of functional behavior of various steel sheets. For high-tensile strength steel, fine precipitates under 10 nm are mainly dispersed in crystal grains of steel. For a steel plate, sub-micrometer sized precipitates are generated at grain-boundary. It is difficult to measure the size distribution of these precipitates in steel due to the non-uniform distribution in the steel sheets and the co-existence of small and large particles with different chemical compounds. Conventionally, the image processing of electron microscope observation has been used for the size distribution measurement, however, for the quantitative analysis of the size and chemical compound distribution it is necessary to require a lot of images and spend for long time observation. New advanced characterization method needs to develop for the rapid characterization of nanometer scaled precipitate in steel.

The major aim of this study is to develop the analytical method for the macroscopically characterization of these precipitates and pre-treatment method for extraction of precipitates in steel samples for the above subjects. The selective potentio-static etching by electrolytic dissolution (SPEED) method is used for the extraction of the precipitates in steels into organic solution. The asymmetric flow field-flow fractionation (AF4)-inductively coupled plasma-mass spectrometry (ICP-MS) system is conducted to measure size and chemical compound distribution of precipitates in a liquid phase. Since controlled dispersion techniques are required for the determination of actual size information of nano-precipitates, the combination of dispersants, solvents and particles has to be considered for the avoidance of mass spectral interference in ICP-MS. Furthermore, the chemical reactivity between particles and other matrices in liquid phase is carefully to be avoided during the process of the pre-treatment and size measurement.

In this thesis, firstly, the chemical reaction between the sulfides and copper ion extracted from steel sheets *via* SPEED method was suppressed by using chelate reagents including polyamine structure. Next, the accuracy of AF4 analysis was investigated by the comparison among transmission electron microscope (TEM) and small-angle X-ray scattering (SAXS), using gold nanoparticles. The peak broadening detected by AF4 was discovered and the correction method for size distribution was developed. Thirdly, the scope of application of AF4-ICP-MS was expanded by the improvement of sample introduction efficiency using the mistral-desolvating system. Finally, the detection sensitivity of AF4-ICP-MS for titanium carbide and vanadium carbide particles in steels was improved by the application of sulfur-free surfactant which can avoid the mass spectral interferences from sulfur. Based on the above approaches, a rapid

characterization method to determine the size distribution of various nanometer scaled precipitates with different chemical composition in steel has been developed by using SPEED and AF4-ICP-MS.

Chapter 1

Introduction

<u>**Chapter 1: Introduction**</u>

Chapter 1. Introduction

1.1 Mechanical properties of steels given by precipitates

1.1.1 Outline of steel products manufacturing process

In these days, steel materials are widely used as the social infrastructure for buildings, bridges, trains, rails, ships and auto-mobiles etc. or daily necessities for home appliances and beverage cans. There are some advantages for us to use these steel materials compared with other materials as follows.

(1) Iron ore involving iron oxides are abundant under the ground and it is easy to reduce, resulting in becoming the low cost.

(2) Mechanical strength is larger than other metallic materials (e.g. aluminum alloys, copper alloys), concretes, and plastics and it is easy for processing.

(3) Various mechanical properties are given by the design of adding alloy elements, heat treatment and rolling.

Fig.1-1 shows each tensile strength at each microstructure in carbon steels [1]. The general heat treatment of steels is conducted as follows. Firstly, steels have ferrite (α; bcc) in a room temperature. Adding heat treatment over Ac_3 point (1184 K) induces transformation to austenite (γ; fcc). Ferrite can dissolve less carbon compared with austenite. Ferrite can dissolve maximum 0.025% carbon at 996 K, on the other hand, austenite can dissolve maximum 2.11%. If austenite is cooled, the crystal phase changes to ferrite by a phase-transformation. At that time, due to the difference of amounts of dissolving carbon, carbon transfer to other microstructures. If the austenite is cooled slowly, because carbon cannot exist much in a ferrite, and new compounds are generated, which is called cementite (Fe_3C). Here, the layered microstructure is formed by ferrite and cementite, which is called perlite. Also, the more rapid cooling than the diffusion of carbon caused the change of bcc crystal structure because of carbon staying in ferrite. This is called non-diffusion transformation, and formed microstructure is named martensite. Moreover, the bainite is obtained by cooling at middle rate between perlite transformation and martensite transformation. Therefore, bainite has ferrite and cementite phases, however, the form, size and dispersion state are much different compared with perlite. As mentioned above, various microstructures (perlite, bainite and martensite) are obtained by the controlling the cooling speed. Fig. 1-2 shows continuous cooling transformation (CCT) diagram in 0.8% carbon steel [2]. This figure shows the transformation behavior with cooling at constant rate, and used well at the design of new materials.

Additionally, the design of alloying element and the adjustment of rolling condition could give influences to the phase transformation, grain size of microstructure and crystal orientation. Thus, the mechanical properties of steels could be easily varied using the above conditions.
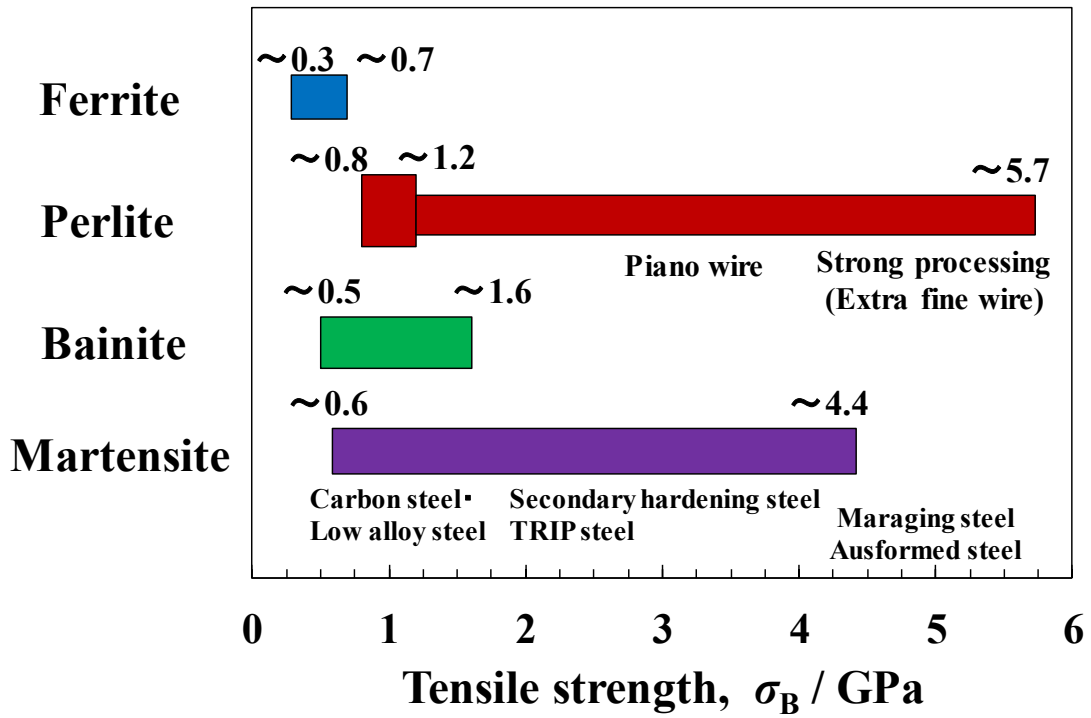
Fig. 1-1 Tensile strength at each microstructure in carbon steels [1].
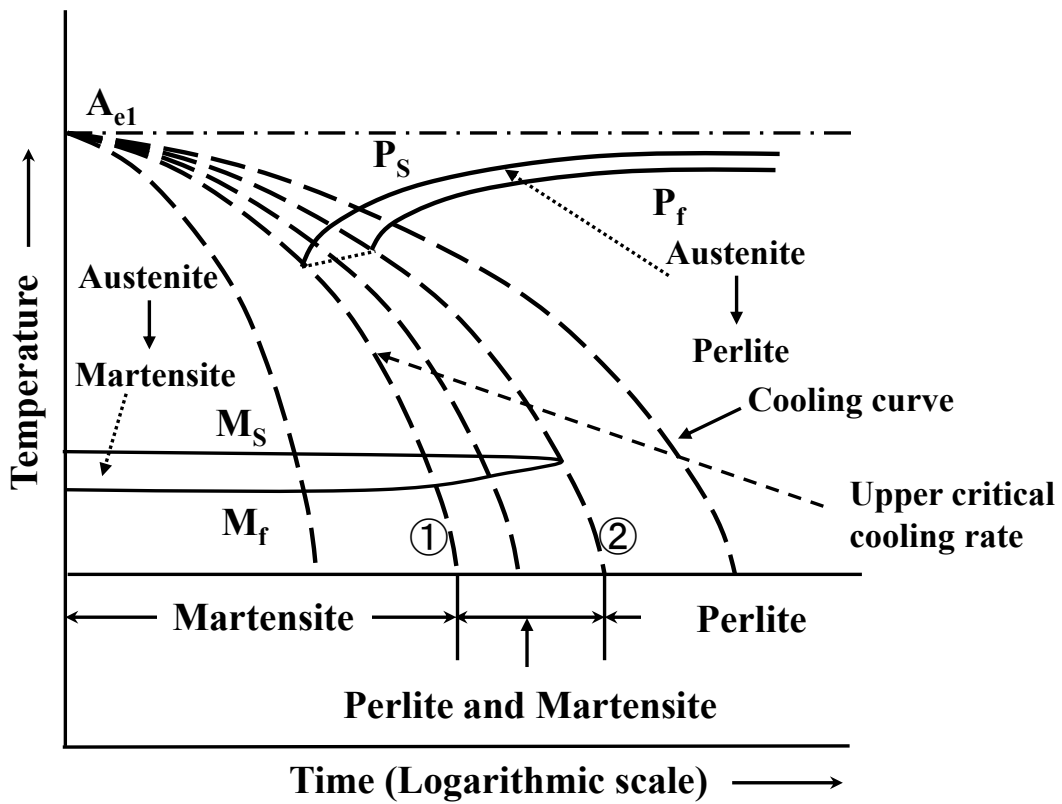
Fig. 1-2 CCT diagram in 0.8% carbon steel [2].

Chapter 1: Introduction

Next, the process of manufacturing steel products is described as follows. Fig.1-3 shows the representative manufacturing process of the hot-rolled steels. The main flow is conducted following procedure; the reduction of iron ores in the blast furnace (BF), the adjustment of elemental composition in the steel making process, casting, hot-rolling, cool-rolling and surface treatment process.
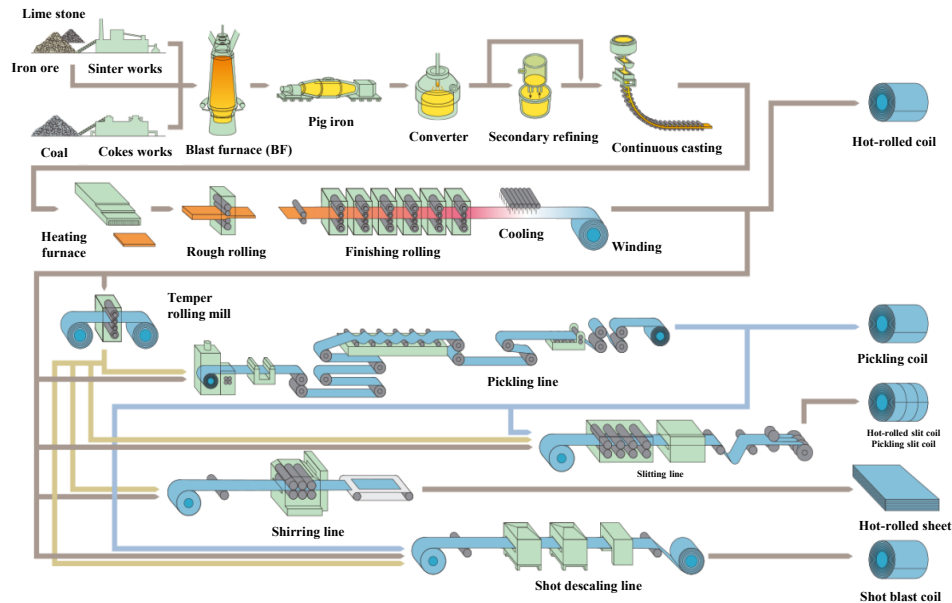
Fig. 1-3 Manufacturing process of hot rolled steels [3].

At first, the BF process is explained as follows. The raw materials of steels are mainly iron ores, coals and limestone. Firstly, the iron ore is reduced in BF process. Prior to the introduction of the iron ore to the BF, the sintered ores are made from the iron ore and limestone at the sinter works. Following that, the coal is transformed to cokes to be ease to use at the BF. After that, the sinter ores and cokes are introduced to the BF, and iron oxides are reduced to be iron according to the solid-gas reaction with equation 1-1 and 1-2, as shown in Fig.1-4. The cokes make carbon mono-oxide (CO) by blowing hot oxygen in the BF. The generated CO has the reductive characteristics and high temperature. The sinter ores are melt and reduced by the CO gases. Finally, the reduced iron with a few percentages of carbon (called as pig iron) and slags are obtained from the bottom of BF. This reductive reaction is very efficient to reduce iron ores and the huge amount of iron ores is daily processed.

$$C(s) + O_2(g) \rightarrow 2CO(g) \qquad \qquad (Eq.1\text{-}1)$$

$$CO(g) + FeO_x(s) \rightarrow CO_2(g) + FeO_{x\text{-}1}(s) \qquad (Eq.1\text{-}2)$$
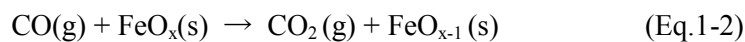
Chapter 1: Introduction
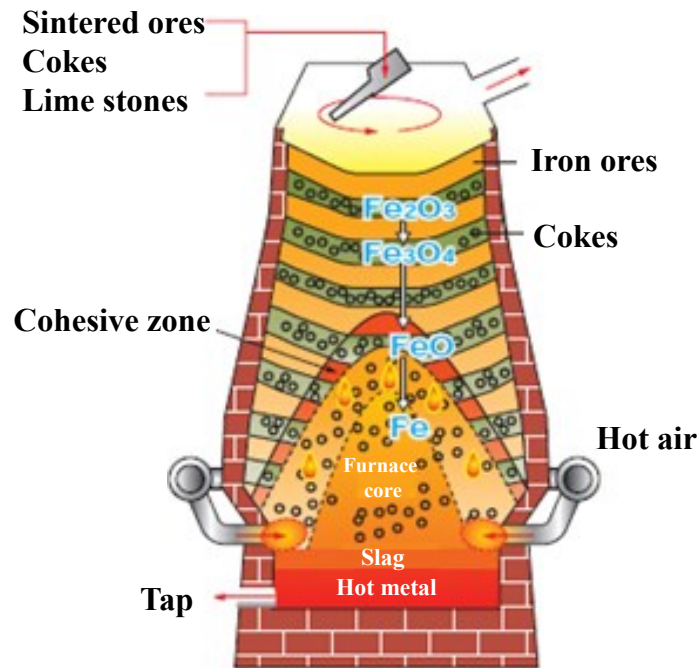
Fig. 1-4 The schematic of the blast furnace process [4].

Secondly, the steel making process is conducted for the adjustment of other element other than iron. The converter method is mainly used for the steel making process in these days. This method has three steps of refining as follows.

1. The elimination of sulfur and phosphorus at the pretreatment of the pig iron
2. The reduction of carbon at the primary refining
3. The elimination of hydrogen, nitrogen and add the alloy-element at secondary refining
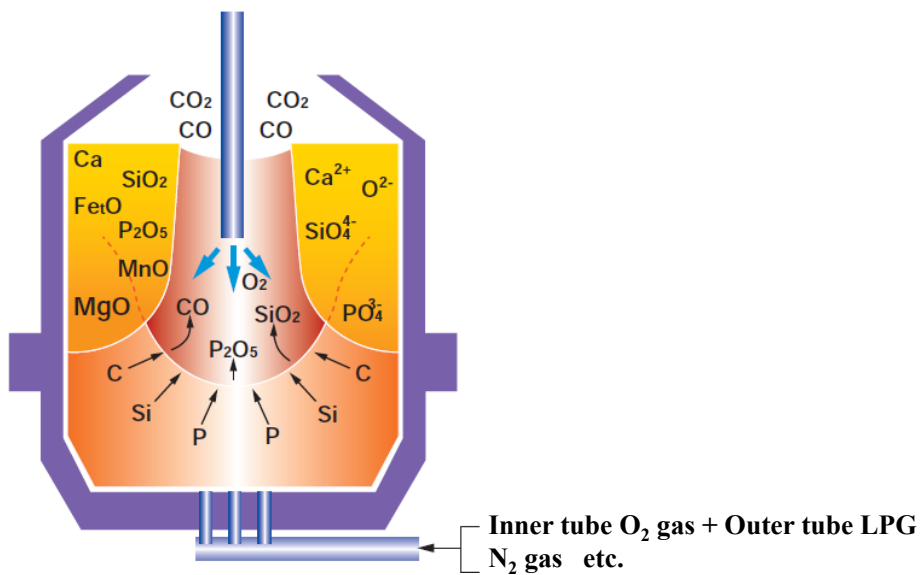
Fig. 1-5 The schematic of the chemical reaction in the converter [5].

Chapter 1: Introduction

Fig.1-5 shows the schematic of the converter. In this process, the excessive elements such as carbon, and the unnecessary element such as sulfur, phosphorus, silicon and manganese are removed from the pig iron. A few amounts of iron scrap, pig iron and calcium carbonate are introduced into the converter. Following that, refining begins by the oxygen blowing at high pressure. Here, the top and bottom blowing method of oxygen is adopted in the converter method. The oxygen reacts with carbon, silicon, phosphorus and manganese and generates high heats by the combustion. The CO and CO_2 are removed as gases, on the other hand, other oxides react with calcium carbonate and stabilize as slags. The slags float to the top by the difference of the density and it is easy to be removed from the steels. As a result, the pure steels with low percentage carbon and few impurities are generated. After that, trace amounts of oxygen and impurities are removed and elemental composition is adjusted at the secondary refining. There are a lot of ways about the secondary refining. For example, the vacuum degassing is conducted by blowing inert argon gas, resulting in removal of carbon, oxygen, nitrogen and hydrogen as gases. The generated steels here are called as the molten steel. The molten steel is delivered to next casting process.

Thirdly, the casting process is described as follows. In this process, the continuous casting (CC) method is mainly adopted and the semi-finished products called as slab are made. Fig.1-6 shows the schematic of the CC process. The important role of CC is the removal of inclusions which brings the cracks and the reduction of mechanical properties of steels. These inclusions generate by re-oxidation of any elements in the molten steel, contamination by the refractory from pots and involving powder from the tundish. The size of inclusions is mainly micrometer order. Prior to the coagulation of the molten steel, the inclusions are floated and removed as possible. The CC machine has many characteristics for removing inclusions. For example, the residence time of molten steel is increased by deploying the several weirs at the tundish, resulting in the increase of floated inclusions. Moreover, the in-mold electromagnetic stirrer (EMS) is used for the uniform stirring. The EMS makes flow in the molten steel by the magnetic force and achieved the removal of inclusions from surface of the slabs. As a result, the cleanliness of the slabs is improved. Here, the demanded cleanliness is different at each steel product. Table.1-1 summarizes the size upper levels of inclusions for each steel product. Especially, the inclusions in the steel code are strictly controlled.

Chapter 1: Introduction
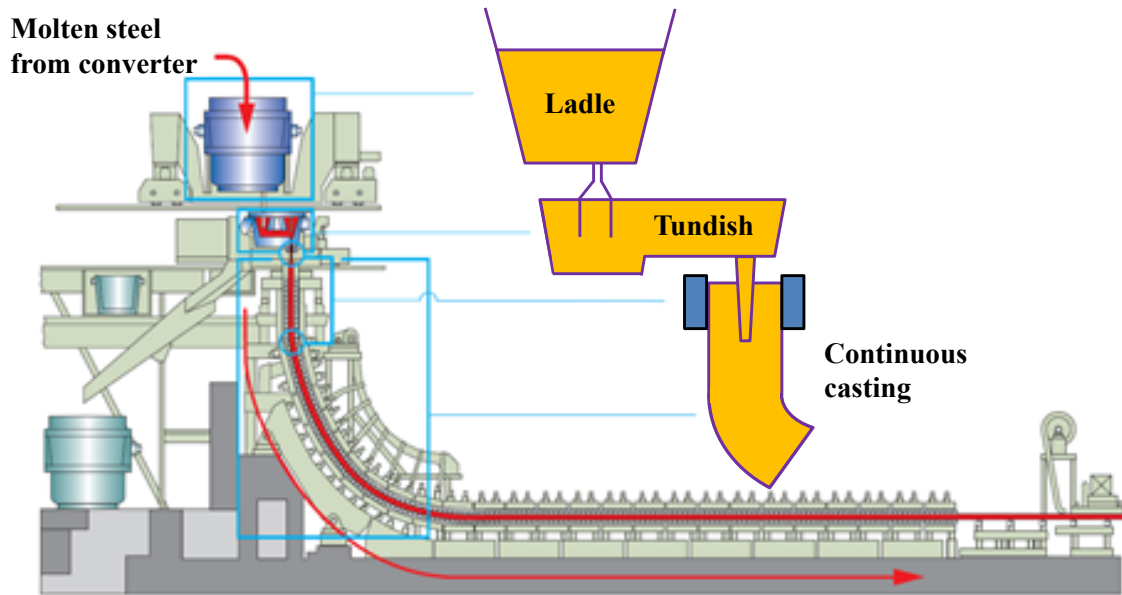
Fig. 1-6 The schematic of the continuous casting [6].

Finally, rolling process of steels is briefly mentioned as following paragraph. The slabs are transported to hot-rolling works and processed. At first, the slabs are heated again and softened for the hot-rolling. Following that, the rough rolling and finishing rolling are conducted to control the thickness of steels precisely. After that, rolled steels are taken up as hot-coil and transported to each product works and processed by the additional cool-rolling and surface treatment. The form of steel products is classified like as thick plate (steel plate, for ships), as sheet (steel sheet, for vehicle), and bar (steel bar, for steel code) and so on. Either steel product must be satisfied with the required qualities of thickness, width, forms and cleanliness of surface. Also, the controlled cooling is conducted for controlling the internal microstructure, crystal grain size, elemental composition of precipitates and size distributions of precipitates, which results in the achievement of the required tensile strength, toughness and magnetic properties and so on. Especially, the relationships between precipitates (mainly has a diameter in nanometer order) and mechanical characteristics in steels will be explained in next subsection.

Chapter 1: Introduction

Table. 1-1 Summary of inclusion control at each steel product [6].

Classification	Use of steel products	Purpose	Upper level of the size of inclusions
Sheet steel	For DI cans	・Prevention of cracks at processing cans	$d < 40$ μm
	For ultra-deep drawing sheet steels	・Lankford value; $r < 2.0 \sim 3.0$ ・High tensile and low thickness	$d < 100$ μm
	For rim	・Prevention of cracking	$d < 100$ μm (Al_2O_3)
	For disc	・Hole spreading processing	$d < 20$ μm (MnS)
Steel plate	For line pipe	・Anti-HIC property (HIC: hydrogen Induced Cracking) ・Addition of stress	Precise control of the forms of inclusions
Steel bar	For bearing	・ Improvement of the rolling fatigue life	・$d < 15$ μm ・Total oxygen concentration < 10 ppm
Steel wire	For tire cord	・High strength ・ Prevention of the disconnection at wire drawing	・$d < 15$ μm ・Total oxygen concentration < 10 ppm
	For spring steel	・ High strength and improvement of fatigue life	

1.1.2　Design of steel products using nanoparticles

The precipitates are defined as nanoparticles which generates during the rolling with the heat treatment. The main role of precipitates is categorized into two types, which is the strengthening of steel sheets and controlling of the size of crystal grains in steels.

Firstly, the strengthening effect is described as follows. For example, the carbides precipitate during the phase transformation from austenite to ferrite. This is well-known as the interface-precipitation and forms like dotted lines of carbides [7]. There are NbC, VC, TiC, Mo_2C, Fe_3C, $Cr_{23}C_6$ and these complex carbides as interface precipitates [8-10]. The spacing

between these carbides is dependent on the temperature of phase transformation, carbon dissolved contents in austenite and the change of precipitation timing by adding manganese, chromium and nickel. Also, the size of carbides is largely dependent on the temperature of phase transformation. It is known that the larger temperature of isothermally transformation, the bigger the size of carbides is obtained [10]. The size distribution (size and number density) of precipitates affects the amount of strengthening in steels. Ashby reported that the smaller size and higher number density of precipitates is given, the larger amount of strengthening in materials [11]. This is called as precipitation strengthening. Additionally, Ashby and Orowan proposed the following equation about precipitation strengthening [12-13].

$$\sigma_{Ashby-Orowan} = \frac{0.8MGb}{2\pi\sqrt{1-\nu}L} \cdot \ln\left(\frac{x}{2b}\right) \quad (MPa) \quad (Eq.1\text{-}3)$$

where σ is the amount of precipitation strengthening, M is the Taylor factor, G is the rigidity, b is the Burgers vector, ν is the Poisson's ratio, L is the average spacing between precipitates and x is the average diameter of precipitates.

According to Eq.1-3, only the average size and number density of precipitates is dependent on the amount of precipitation strengthening. Kamikawa reported that the relationship between the average size of carbides in steels and the precipitation strengthening which is experimentally determined, as shown in Fig.1-7 [10]. These results are well consistent the Ashby-Orowan's relationships. The controlling the size distribution of nano-precipitates by the heat treatment and rolling is important to give the precipitation strengthening to the steels.
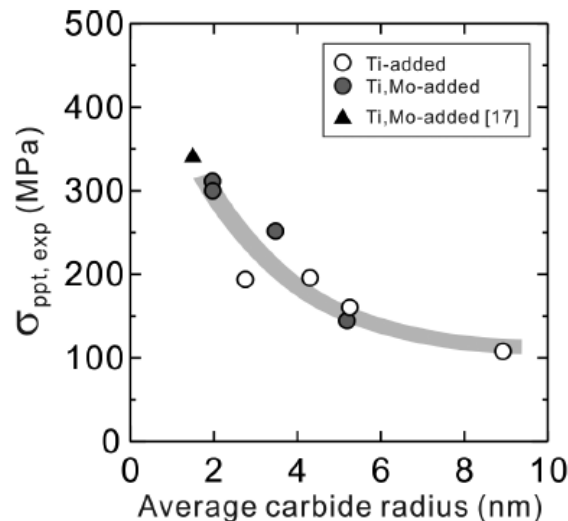
Fig. 1-7 Precipitation strengthening experimentally determined as a function of average carbide radius for the Ti-added and Ti, Mo-added steels transformed at 700°C for different holding periods [10].

Chapter 1: Introduction

Next, the techniques for controlling the crystal grain size by the precipitates are explained as follows. The controlling of crystal grain size is effective for obtaining various mechanical properties in steels. For example, the steel plate is required the high toughness in the high temperature. To use the steel plate for welded structure, high-heat-input welding is generally conducted. In case of this welding method, the position around welding is heated at 1673 K or higher for a considerable time period. This position is called heat affected zone (HAZ) and austenite (γ) grains grow significantly. Moreover, a low cooling rate in the transformation temperature zone brings the coarse HAZ microstructure and its toughness becomes lower as a consequence. In many cases, the coarse grain boundary ferrite (GBF) and/or ferrite side plates (FSPs) generates at the coarse austenite grain boundary. The grain size of the coarse GBF is several hundred micrometers, which causes fracture. It is considered that the GBF is soft structure and the impact strain concentrated easily on the coarse GBF. As a result, the fracture is induced by the coarse GBF. Also, it has been confirmed that a similar effect is detrimental to toughness at the coarse FSPs. The morphology of the coarse GBF and/or FSPs is influenced by the size of γ grains. Fig.1-8 shows two HAZ microstructures which consist of different sizes of γ grains, GBF and/or FSPs [14]. The smaller γ grains bring the smaller GBF and/or FSPs. Additionally, the toughness of steels is improved by the smaller GBF and/or FSPs. Thus, it is important to keep the small size of γ grains during the high-heat-input welding.
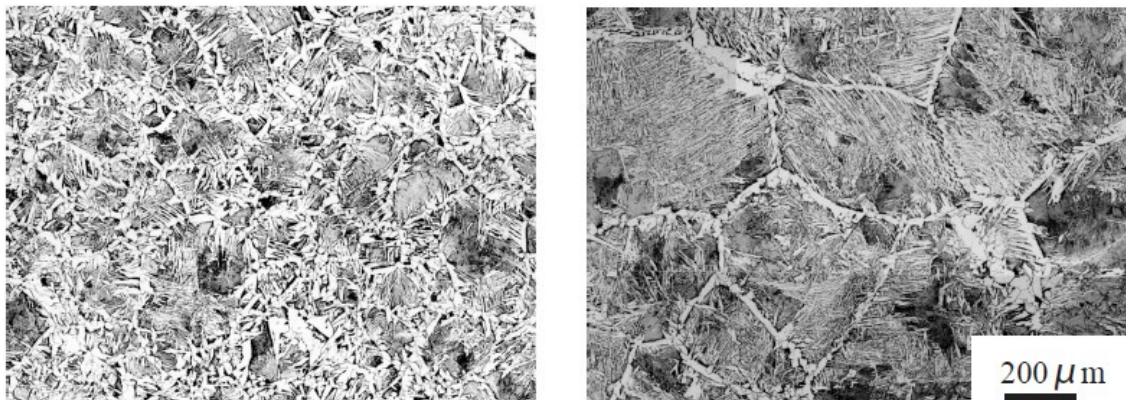
Fig. 1-8 Simulated HAZ microstructure of 490 MPa class steel corresponding to submerged arc welding with 10 kJ/mm.
 (a) γ grain size: approx. 100 μm, (b) γ grain size: approx. 400 μm [14].

Chapter 1: Introduction

To control the size of γ grains, the precipitates ranging from the nanometer to sub-micrometer are used for the purpose of pinning the grain growth. Generally speaking, pinning effect is known the following Zener's equation (Eq.1-4) [15-16].

$$R = (4/3) \cdot (r/f) \qquad \text{(Eq. 1-4)}$$

where R is the radius of a crystal grain, r is the radius of a second phase particle and f is the volume fraction of second phase particles.

According to Eq.1-4, it is needed to make smaller the term of (r/f) for the suppression of the γ grains growth. Besides this, the thermal stability of precipitates in above steel plate is required because the steels are exposed at high temperature (1673 K) during the high-heat-input welding. If the precipitates are dissolved or grown in this situation, reduced f and increased r are obtained. As a result, r/f becomes larger, pinning effect will be weak. Additionally, the grown coarse precipitates could be the initiation site of a fracture. Thus, it is important to select the kind of precipitates and control the size distribution of precipitates for the above requirement.

From above demands, it is necessary to analyze quantitatively the size distribution of precipitates in steels for the development of various steels. If their knowledge is obtained, the operating conditions for manufacturing process, such as heating temperature, cooling rate, and alloy designing, could be determined optimally in a production line. Additionally, the both feedback between these analytical and manufacturing results will become more important between laboratories and plants for the most efficient production. In the next section, how to analyze these precipitates is explained in detail.

1.2 Conventional analytical method and the problems for nanometer-sized precipitates in steels

1.2.1 Transmission electron microscope (TEM)

The most general method to measure the precipitates in steels is using the electron microscope. For transmission electron microscope (TEM) observation, steel samples are processed by scanning electron microscope (SEM) with focused ion beam (FIB) [17] and the micro-area to be observed is extracted from bulk samples. The observed steel samples are sharpened to be the thickness of about 30 micrometer (called as a thin-film TEM method). Fig.1-9 shows examples of a titanium carbide precipitate in thin steel sample by TEM observation. The observed area was much small and the number of observed precipitates was only one. Due to the small observed area and localization of precipitation like Fig.1-9, it is hard to obtain the statistically significant difference about size distribution of precipitates among

Chapter 1: Introduction

several steel samples. However many researchers discuss the mechanism of precipitation phenomenon using results of a few precipitates measured by TEM, it is difficult to understand these mechanisms in steels made at plants. Because the various extrinsic factors (temperature slope at heating, the distributions of rolling reduction and thermal history at cooling etc.) exist in the machines to make the steel products. Thus, the differences between laboratory and plants often occur and would become the hurdles in case of manufacturing the developed steel products in a production line.
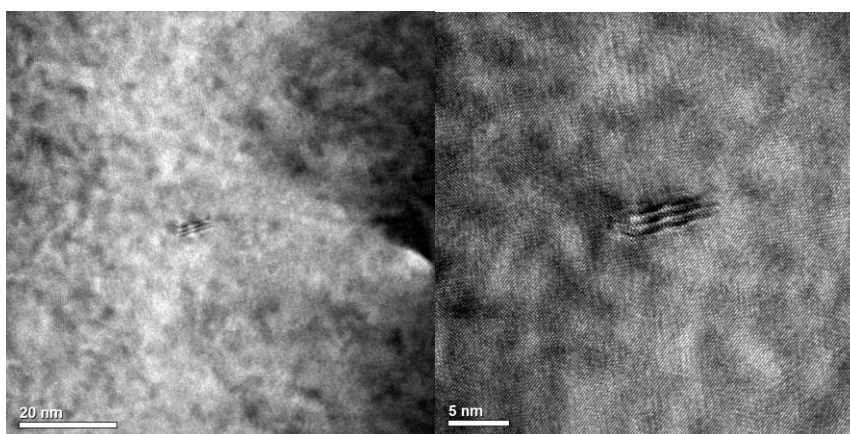
Fig. 1-9 Examples of titanium carbide precipitates in thin steel samples by TEM observation. Left picture is low magnification and right picture is high magnification.

To overcome this problem, the carbon extracted replica TEM method was developed. Fig.1-10 shows the schematic of the carbon extracted replica TEM method. In this method, the precipitates are emerged by selectively etching of iron. After the carbon deposition, the precipitates are fixed on the carbon film. Finally, samples are immersed to the stripping solution, resulting in separation from the steel samples of carbon film with the precipitates. The carbon film samples are easily observed using TEM. Fig.1-11 shows the example of cementite (Fe_3C) and sulfide precipitates. Compared to a thin-film TEM method, the precipitates in the carbon film are clearly observed and the more precipitates are observed and counted.

Chapter 1: Introduction
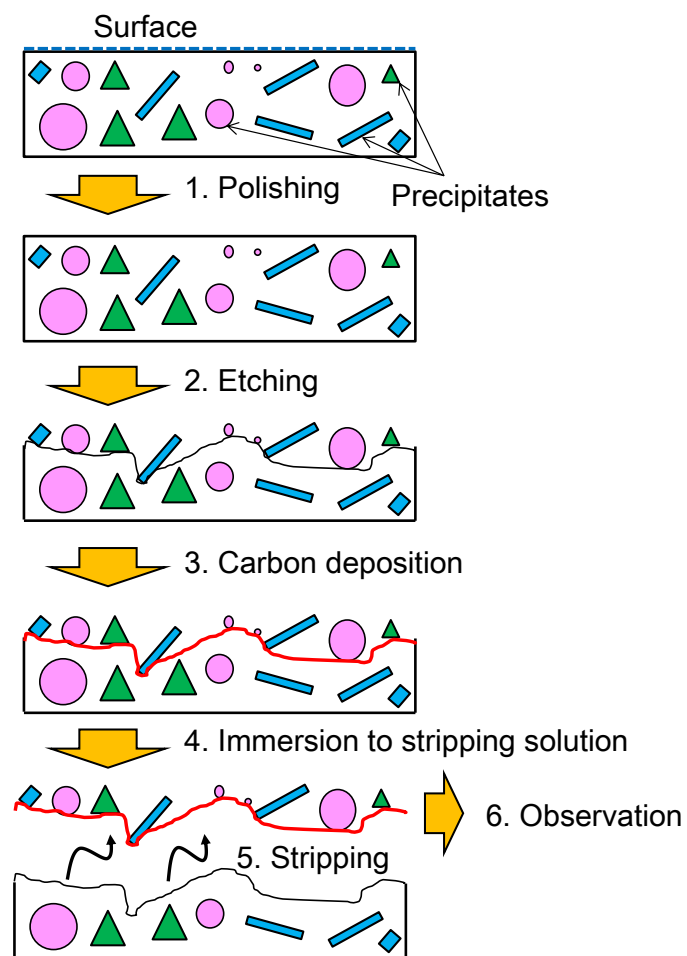
Fig. 1-10 The schematic of the carbon extracted replica TEM method.
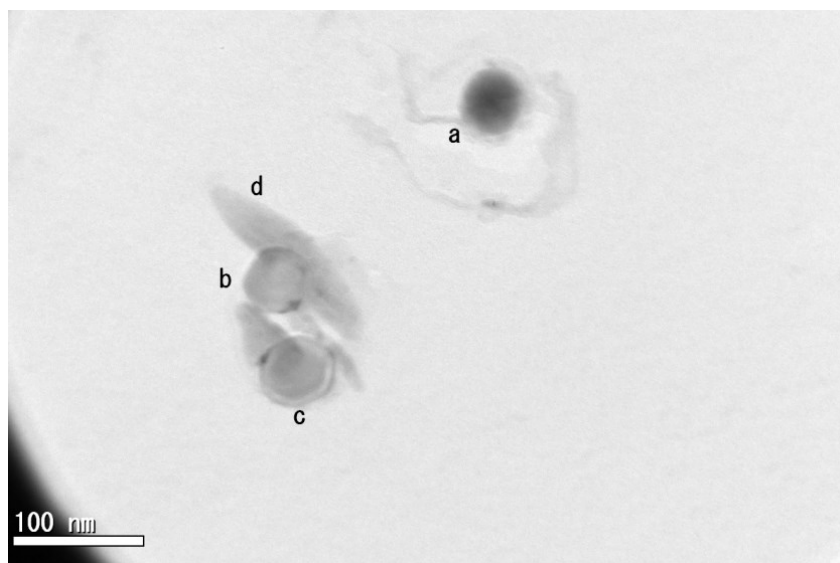
Fig. 1-11 Observation of precipitates by the carbon extracted replica TEM method.

(a), (b) and (c) are sulfide precipitates and (d) is cementite.

Chapter 1: Introduction

However, this method has two problems as follows. Firstly, there is an uncertainty that may not be possible to obtain all precipitates in steel samples. It has been pointed out that a part of precipitates might be lost in the stripping solution. Secondly, as shown in Fig.1-11, the physical hiding between several particles often occurs. It is because the coarse particles hind easily the fine particles, the fine particles might be missed in a counting method using TEM. In steel samples, the coarse and fine particles are generally co-existed. There is a possibility that the incorrect size distribution is obtained. Thus, it is considered that using TEM is not suitable for counting these particles accurately. On the other hand, the morphology of precipitates, the lattice analysis in precipitates and the relationship about oriental direction between particles and iron matrices are observed well using TEM [18-19]. To understand about the mechanism of the precipitation phenomenon, TEM observation is very useful.

1.2.2 Chemical analysis

In the characterization of precipitates, it is also important to know the amount of precipitates using the chemical analysis. The chemical separation methods for precipitates in steels are summarized in Table.1-2. The chemical separation method are the ways which dissolves iron matrix using the chemical reagents and/or electrolytic dissolution and separate the target precipitates, has been researched most widespread. These methods can be distinguished to chemical dissolution method and electrolytic dissolution method. In the following paragraph, these details are described.

Table. 1-2 Chemical separation methods for precipitates in steels

Major classification	Minor classification	Reagent
Chemical dissolution	Acid dissolution method	HCl, H_2SO_4, HNO_3, HCOOH, CH_3COOH
	Halogen method	I_2, Br_2, Cl_2
	Others	Cu, Fe, Hg solutions
Electrolytic dissolution	With constant current	Aqueous solution (Citric acid, Phosphoric acid, etc.)
	With constant potential	Non-aqueous solution (10%AA, 4%MS, etc.)

Chapter 1: Introduction

(1) Acid dissolution method

In chemical dissolution method, the solvency differences for chemical reagents (acid or halogen) are used for the dissolution of matrix and the separation of precipitates. The acid dissolution method is widely utilized for the reason of the simplicity and less time taken to be conducted. However, the solvency is stronger than the electrolytic dissolution method mentioned later, the instable precipitates sometimes dissolves partly. Thus, not to dissolve the precipitates, they are applied to the stable precipitates. For example, the oxides are known as compounds with poor solubility for acids. Aluminum oxide (Al_2O_3), silicon oxide (SiO_2), chromium oxide (Cr_2O_3), titanium (Ⅳ) oxide (TiO_2) and hibonite ($CaO \cdot 6Al_2O_3$) are extracted quantitatively with any concentration of acids [20]. On the other hand, it was discussed whether vanadium oxide (V_2O_5) [21] and niobium oxide (Nb_2O_5) [22, 23] were dissolved by acids. It was also reported that titanium(Ⅲ) oxide (Ti_2O_3), zirconium oxide (ZrO_2) and iron-niobium oxide (Fe-Nb oxides) were extracted quantitatively [24]. Thus, this method could not completely extract the all oxides and it is considered that this method is not suitable to extract instable precipitates.

(2) Halogen dissolution method

The aqueous solution or non-aqueous solution with either of iodine, bromine and chlorine are used for the halogen dissolution method. First of all, the iodine method is explained as follows. Iodine is the weakest oxidizing power among halogen dissolution method and many precipitates (oxides, carbides, sulfides and nitrides) are extracted stably, but part of precipitates are dissolved partly (e.g. V_2O_5, MnS, CaO etc.). And also, there are problems that the iodine has a less solvency for the water and it is taken much time for the iron dissolution by aqueous solution. Moreover, the aqueous solution changes to the acidity during the dissolution, resulting in the dissolution of (Fe, Mn) oxides or the pollution by the deposits (iron hydroxide derived from dissolved iron). Therefore, the non-aqueous solvent is used now. Especially, for the reasons that methanol has a large solvency of the iodine and less amount of water, it is suitable for the extraction of oxides (Al_2O_3, SiO_2, FeO and MnO) in steels. Next, bromine has stronger oxidizing power than iodine and can dissolve carbides, sulfides, nitrides which are hard to dissolve by iodine. Therefore, bromine methanol method is used for the extraction of stable oxides. Additionally, it was reported that the bromine methyl acetate could extract aluminum nitride (AlN) [25]. Finally, the chlorine has the strongest oxidizing power among halogen dissolution method. All of Al_2O_3, SiO_2, and most part of (Fe, Mn) oxides could be extracted [26], but this method is not used now to keep the safety on the experimental operations.

Thus, the chemical dissolution method is effective for the extraction of the stable oxides, however, this is not suitable for other precipitates which are relatively instable.

Chapter 1: Introduction

(3) Electrolytic dissolution method

The electrolytic dissolution method is the method using the electrolysis process of metal matrices in steel samples and the extraction process of precipitates not dissolved by the electrolysis. At the first ages, the electrolytic dissolution method with citric acid solutions and constant current or potential was used for oxides and other precipitates [27, 28]. However, as shown in Fig.1-12 (a), part of instable precipitates is dissolved in aqueous solutions. Additionally, the surface of steel samples is oxidized and passivated. Thus, to control these current and potential in aqueous solutions to extract quantitatively precipitates is difficult.

After that, the electrolytic dissolution method with constant potential using non-aqueous solutions was developed to overcome above problems (called as selective potentio-static etching by electrolytic dissolution (SPEED) method) [30]. It was reported that the solution with 10 (v/v) % acetylacetone (AA) and 1 (w/v) % tetramethyl ammonium chloride (TMAC) and methanol (called as 10% AA electrolytic solution) is most suitable to extract instable cementite (Fe_3C) and MnS in steels quantitatively [30]. Herein, the AA acts as the chelating agent for dissolved iron ions as shown in Fig. 1-13. These reaction proceeds easily and the transparent solution changes to a red color during operating the electrolytic dissolution of steel samples. The generated iron chelate ($Fe(acac)_2$) has a great solvency to the methanol and can be easily visible at a low concentration (approximately 10^{-4} mol L^{-1}). Additionally, $Fe(acac)_2$ is oxidized readily to the most stable $Fe(acac)_3$ which is difficult to be decomposed at the surface of steels. Thus, the pollution for residues from steels by dissolved iron ions can be avoided and the amount of precipitates can be analyzed quantitatively by the chemical analysis.

Next, Fig.1-12 (b) shows the relationship between potential and current at the electrolysis with 10% AA electrolytic solution. This method enables the selective dissolution of iron matrices throughout wide potentials at the electrolysis. It was also reported that 4 (v/v) % methyl salicylate and 1 (w/v) % salicylic acid and 1 (w/v) % TMAC and methanol solution (called as 4% MS electrolytic solution) was suitable for the extraction of instable sulfides such as FeS, CaS and RE_2S_3 (RE = Ce, La) [31, 32]. For the analysis of precipitates in titanium alloys, other electrolytic solution had been also investigated. The titanium clad steel has the heterogeneous matrices composed of the different solvency characteristics. To control these matrices dissolution evenly, the electrolytic solution of 10 (v/v) % methyl salicylate and 2 (w/v) % TMAC and methanol was developed [33]. The representative electrolytic solutions are summarized in Table.1-3. As mentioned above, these extraction methods had been investigated to analyze quantitatively the various precipitates in steels and alloys. Table.1-4 summarized the various extraction methods for precipitates in steels.

(a) Aqueous electrolytic solution

AlN   Fe   Fe₃C

Current (mA)

-1000   -500   0   500   1000

Potential (mV *vs.* SCE)
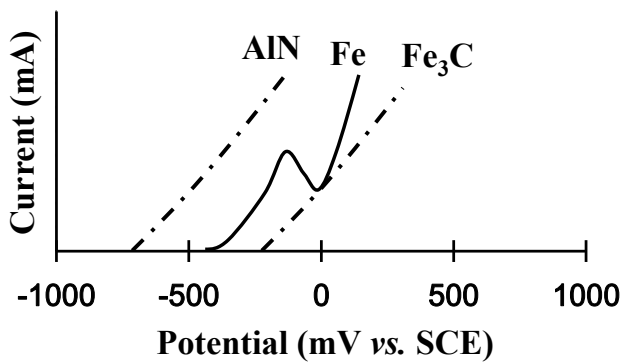
(First generation)
For carbon steel
Electrolytic solution:
5～15 wt. % Sodium citrate
1.2 wt.% KBr
0.5 wt.% KI
pH 6.0～9.0

(b) Non-aqueous electrolytic solution
(Selective dissolution)

Fe₃C

Stainless steel
Carbon steel   **Super alloy**   AlN
Pure titanium

Current (mA)

-1000   -500   0   500   1000

Potential (mV *vs.* SCE)
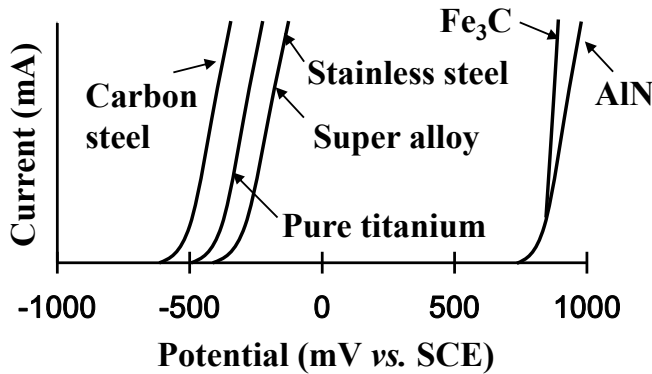
(Second generation)
For steel, super-alloy
and pure titanium
Electrolytic solution:
･10 (v/v) % Acetylacetone-
1 (w/v) % TMAC-methanol
･10 (v/v) % Maleic anhydride-
2 (w/v) % TMAC-methanol

(c) Non-aqueous electrolytic solution
(Uniform dissolution of matrix)

Carbon steel   Fe₃C
Stainless steel   **Pure titanium**   AlN

Current (mA)

-1000   -500   0   500   1000

Potential (mV *vs.* SCE)
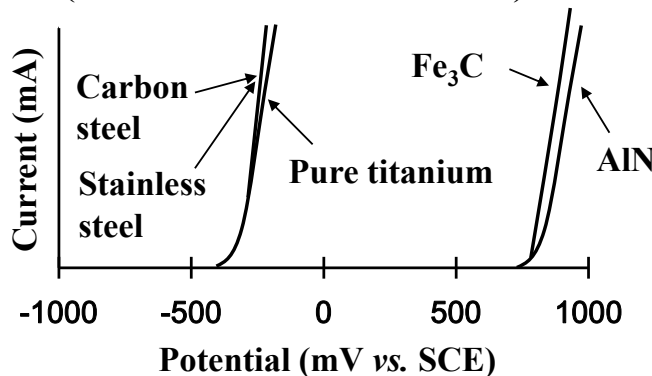
(Third generation)
For titanium alloy
and titanium clad steel
Electrolytic solution:
･10 (v/v) % Methyl salicylate
-2 (w/v) % TMAC-MeOH

Fig. 1-12 The relationship between potential and current at the electrolysis with various solutions. (a) Aqueous solution for carbon steels, (b) non-aqueous solution for steels, super alloy and pure titanium and (c) non-aqueous solution for titanium alloys [29].

Chapter 1: Introduction

(i) Ionization reaction of matrix

$$Fe \longrightarrow Fe^{2+} + 2e^{-}$$

(ii) Chelation reaction

Fe²⁺ + 2 CH₃—C—CH=C—CH₃ (with O below, lone pair ·· and O(-))

Transparent : Acetylacetone

(structure of ferric acetylacetonate with CH₃, CH, C=O, C—O, Fe central)

Red : ferric acetylacetonate (II)

(Appendix) Ionization reaction of electrolyte

$$(CH_3)_4N^+Cl^- \rightleftarrows (CH_3)_4N^+ + Cl^-$$
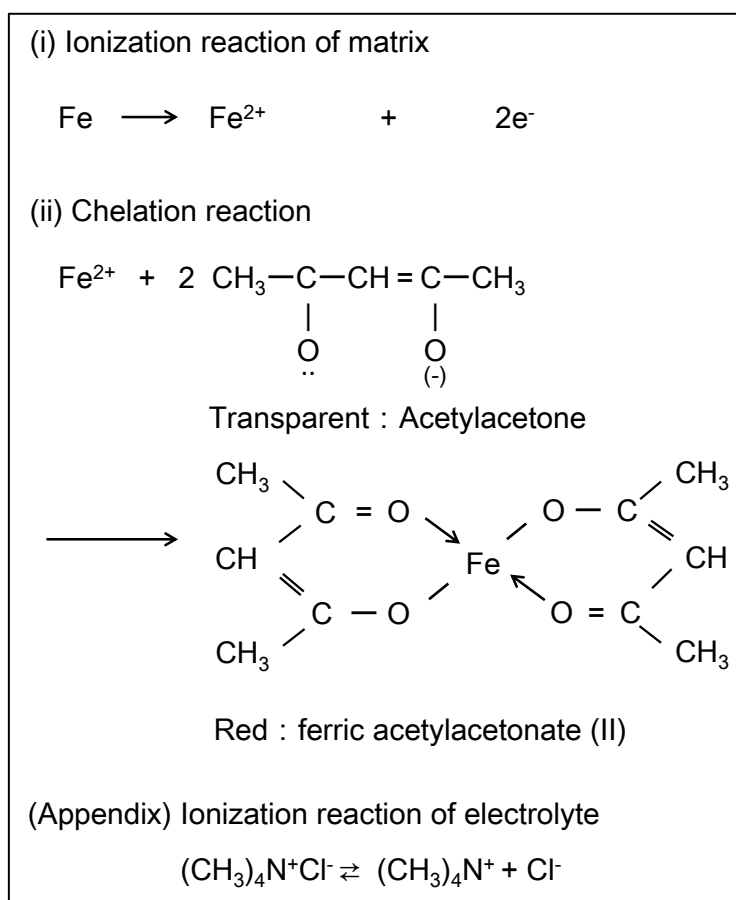
Fig. 1-13 The chemical reaction between chelating agent and dissolved iron ions
in the electrolytic solution (chelating agent :AA, electrolyte: TMAC).

Table.1-3 The representative electrolytic solutions for steels and alloys [29].

No.	Composition of the electrolytic solution	Materials	Purpose
1	10% acetylacetone-1% TMAC-methanol	Steels, Superalloy	General precipitates
2	10% acetylacetone-1% hydrochloric acid-methanol	Steels	σ phase in dual phase stainless steels
3	4% methyl salicylate-1% salicylic acid-1% TMAC-methanol	Steels	Sulfides
4	10% methyl salicylate-2% TMAC-methanol	Titanium alloy, Superalloy	Precipitates in titanium clad steels
5	10% maleic anhydride-2% TMAC-methanol	Steels, Superalloy	General precipitates
6	10% maleic anhydride-2% ZnCl$_2$-ethanol	Steels, Superalloy	δ-ferrite in stainless steels
7	1% tartaric acid-1% ammonium sulfate-water	Steels, Superalloy	γ' phase, β phase
8	3% nitric acid-2% perchloric acid-methanol	Steels, Superalloy	γ' phase, β phase

Chapter 1: Introduction

Table. 1-4 The summary of various extraction methods for precipitates in steels [34].

Forms of precipitates (Oxides)	Extraction methods	Comments
(Fe, Mn) O (Mn, Fe) O	None	Chemically instable, difficult to extract quantitatively.
MnO·SiO₂	・I₂-methanol method (in the 333 K bath) ・Br₂-methanol method (in the 333 K bath)	For carbon steels and low-alloyed steels ・In the case of Mn/Si ratio over 6, it was reported that the quantitative extraction is not able to be conducted. ・Almost not affected by MnS and cementite ・Spessartite, mullite and corundum are able to be also extracted.
CaO·SiO₂	・I₂-methanol method (in the 333 K bath)	For carbon steels and low-alloyed steels ・In the case of CaO over 50 mass%, it was reported that the quantitative extraction is not able to be conducted. ・Gehlenite is able to be also extracted.
CaO·Al₂O₃	・I₂-methanol method (in the 333 K bath) ・Br₂-methanol method (in the 333 K bath)	For carbon steels, low-oxygen steels and stainless steels ・In the case of CaO over 50 mass%, it was reported that the quantitative extraction is not able to be conducted. ・Spinel is able to be also extracted. ・In low-alloyed steels and stainless steels, Br₂-methanol method is preferable due to the rapid decomposition of matrices.
Al₂O₃	・I₂-methanol method (in the 333 K bath) ・Br₂-methanol method (in the 333 K bath) ・Hot mixed acid method ・Hot sulfuric acid method	・In the case of aluminum-deoxidized steels, it is able to be applied to carbon steels, low-alloyed steels and stainless steels. ・Silicon other than oxides is detected by using halogen methods. ・In the case of stainless steels, Br₂-methanol or hot sulfuric acid method are preferable due to the rapid decomposition of matrices.

Forms of precipitates (Carbides)	Extraction methods	Comments
M$_3$C type **Fe$_3$C**	10% AA electrolytic solution with constant potential of electrolytic dissolution	For carbon steels and low-alloyed steels. The fine cementite is extracted well.
MC type **TiC**	Hydrochloric acid (1+1), Phosphoric acid (2+1) dissolution method	For carbon steels and low-alloyed steels. For relatively coarse TiC.
	10% AA electrolytic solution with constant potential of electrolytic dissolution	For carbon steels and low-alloyed steels. The fine TiC is extracted well and M$_3$C carbides are simultaneously extracted.
MC type **VC**	10% AA electrolytic solution with constant potential of electrolytic dissolution	For carbon steels and low-alloyed steels. The fine VCs are extracted well and M$_3$C carbides are simultaneously extracted.
M$_7$C$_3$ type, **M$_{23}$C$_6$ type** **(Cr, Fe)$_7$C$_3$** **(Cr, Fe)$_{23}$C$_6$**	Phosphoric acid (2+1) dissolution method	For carbon steels, low-alloyed steels and stainless steels. M$_2$C type carbides are also extracted simultaneously.
	10% AA electrolytic solution with constant potential of electrolytic dissolution	For carbon steels, low-alloyed steels and stainless steels. M$_3$C, M$_2$C and M$_6$C type carbides are also extracted simultaneously. In the case of certain steels, 4 (w/v) % sulfosalicylic acid-1 (w/v) % lithium chloride-10 (v/v) % ethylene glycol-methanol solutions are applied with constant potential of electrolytic dissolution.
M$_2$C type **Mo$_2$C**	10% AA electrolytic solution with constant potential of electrolytic dissolution	For carbon steels and low-alloyed steels. M$_3$C, M$_7$C$_3$, M$_{23}$C$_6$ and M$_6$C type carbides are also extracted simultaneously.

MC type NbC	Phosphoric acid (2+1) dissolution method	For carbon steels and low-alloyed steels. M_2C type carbides are also extracted simultaneously.
	·15 (w/v) % sodium citrate-1.2 (w/v) % potassium bromide-30 (w/v) % citric acid aqueous solution (pH 3.0) with constant potential of electrolytic dissolution ·7 (v/v) % hydrochloric acid-3 (w/v) % iron chloride (Ⅲ)-ethylene glycol solution with constant potential of electrolytic dissolution · 10% AA electrolytic solution with constant potential of electrolytic dissolution	For carbon steels and low-alloyed steels. M_3C and M_2C type carbides are also extracted simultaneously.
MC type ZrC	·7 (v/v) % hydrochloric acid-3 (w/v) % iron chloride (Ⅲ)-ethylene glycol solution with constant potential of electrolytic dissolution · 10% AA electrolytic solution with constant potential of electrolytic dissolution	For carbon steels and low-alloyed steels.
M_6C type **(Fe, W)$_6$C**	15 (w/v) % sodium citrate-1.2 (w/v) % potassium bromide-30 (w/v) % citric acid aqueous solution (pH 3.0) with constant potential of electrolytic dissolution · 10% AA electrolytic solution with constant potential of electrolytic dissolution	For carbon steels and low-alloyed steels. M_3C and relatively stable carbides are also extracted simultaneously.

Chapter 1: Introduction

Forms of precipitates (Nitrides)	Extraction methods	Comments
AlN	・10% AA electrolytic solution with constant potential of electrolytic dissolution ・I$_2$-methanol method (333 K)	For carbon steels (included high-tensile steel), low-alloyed steels and stainless steels.
BN	・10% AA electrolytic solution with constant potential of electrolytic dissolution ・I$_2$-methanol method (R.T.)	For carbon steels.
Si$_3$N$_4$	・10% AA electrolytic solution with constant potential of electrolytic dissolution ・I$_2$-methanol method (333 K)	For carbon steels. The chemical stability of Si$_3$N$_4$ is dependent on the precipitation forms. It is desirable to apply alkaline melting or bomb methods for the dissolution of residues.
TiN	・10% AA electrolytic solution with constant potential of electrolytic dissolution ・I$_2$-methanol method (333 K) ・Phosphoric acid (2+1) dissolution method (R.T.)	For carbon steels (included high-tensile steel) and stainless steels. In the case of 10% AA electrolytic solution with constant potential of electrolytic dissolution, TiC is also extracted simultaneously.
ZrN	・10% AA electrolytic solution with constant potential of electrolytic dissolution ・I$_2$-methanol method (333 K)	For carbon steel. In the case of 10% AA electrolytic solution with constant potential of electrolytic dissolution, ZrC is also extracted simultaneously.
VN	10% AA electrolytic solution with constant potential of electrolytic dissolution	For carbon steels (included high-tensile steel). VC is also extracted simultaneously.

NbN	・10% AA electrolytic solution with constant potential of electrolytic dissolution ・I_2-methanol method (333 K) ・Phosphoric acid (2+1) dissolution method (R.T.)	For carbon steels (included high-tensile steel) and stainless steels. Outside the case of I_2-methanol method, NbC is also extracted simultaneously.
CrN	・10% AA electrolytic solution with constant potential of electrolytic dissolution ・I_2-methanol method (333 K) ・Hydrochloric acid (1+1) dissolution method (in the boiling bath)	For Cr-adding steels. Outside the case of hydrochloric acid (1+1) dissolution method, Cr carbides are almost quantitatively extracted.
β-Cr₂N	・10% AA electrolytic solution with constant potential of electrolytic dissolution ・I_2-methanol method (333 K)	For Cr-adding steels, stainless steels and anti-heat steels. M_7C_3 and $M_{23}C_6$ are also extracted simultaneously.

Forms of precipitates (Sulfides)	Extraction methods	The quantitative analysis method
MnS **TiS** **Zr₃S₄**	・10% AA electrolytic solution with constant potential of electrolytic dissolution ・4% MS electrolytic solution with constant potential of electrolytic dissolution	・Combustion and infrared absorption spectroscopy method ・Combustion and neutralization titration method ・Combustion and potassium iodate titration method
FeS **CaS** **RE₂S₃**	・4% MS electrolytic solution with constant potential of electrolytic dissolution	・Hydrogen sulfide vapor separation and methylene blue absorption spectrophotometry method (for MnS, CaS and RE_2S_3)

Chapter 1: Introduction

The extracted precipitates are collected via the suction filtration and dissolved by acid or melted by alkaline. After that, the amounts of precipitates are quantified by inductively coupled plasma-atomic emission spectroscopy (ICP-AES), atomic absorption spectroscopy (AAS) and absorption spectrophotometry methods. If necessary, the crystal phase of the precipitates are identified by X-ray diffraction (XRD) and/or Fourier transform infrared spectroscopy (FT-IR). The process flow of chemical analysis methods for the precipitates showed in Fig.1-14. As explained above, the amounts of the precipitates are able to be investigated. However, as a matter of course, the size distribution of precipitates is ignored in these analytical methods because of dissolution process by acids or alkaline. Thus, the precipitates were conventionally evaluated by the size evaluation from TEM observation and the quantitative analysis of the amounts by the various chemical analyses.
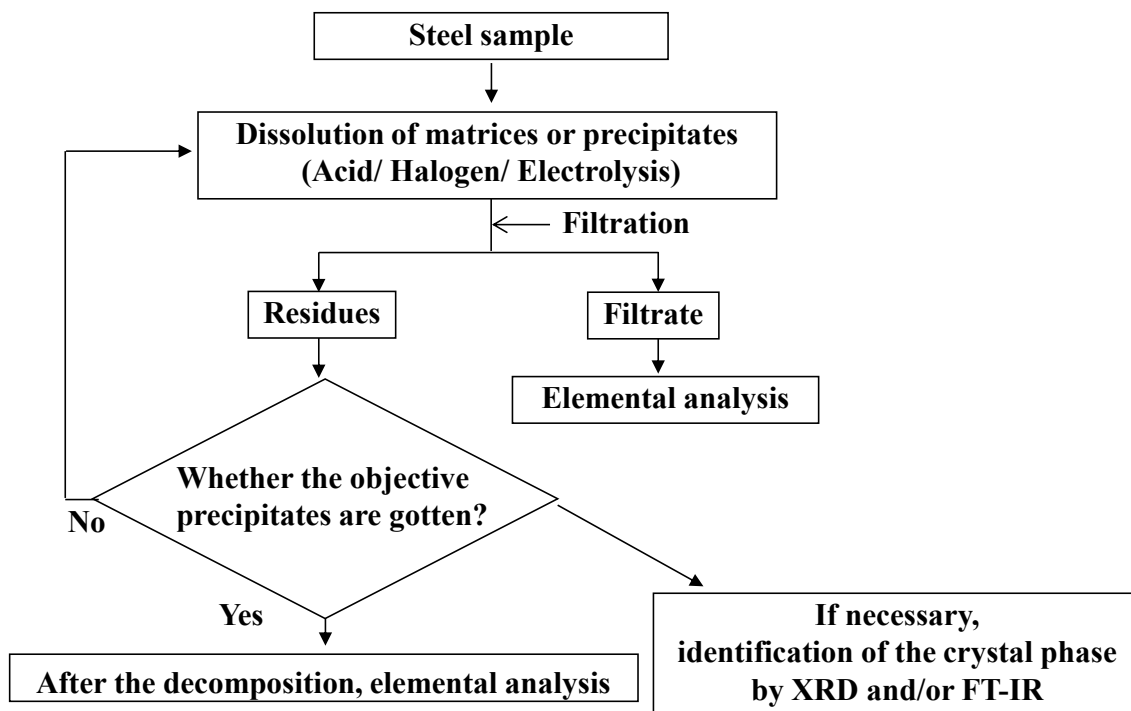
Fig. 1-14 The process flow of chemical analysis for the precipitates in steels [34].

Chapter 1: Introduction

1.2.3   Summary of conventional evaluation method and the problems

As mentioned above, there are the problems about the analysis method for the precipitates in steels.

(1) The precipitates distribution is usually non-uniform in steels. TEM or SEM observations enable the direct counting of number and measurement of size for the precipitates, however, the non-uniform distributions often confuses our understandings.

(2) Many of the objective precipitates are extracted well by various chemical extraction methods. The obtained amounts of the precipitates are more representative than the values estimated from the observation methods due to the decomposition of many samples. However, only the amounts of precipitates are analyzed because of the dissolution of the extracted residues.

Therefore, it is much difficult to analyze the more representative size distributions (size and number density) for the precipitates in steels using the conventional methods explained above.

1.3   Analysis of nanoparticles using Asymmetric Flow Field-Flow Fractionation (AF4)

From these problems, it is considered to develop the analytical methods for the size distributions of the precipitates in steels involving the representative information. The best way to measure the size distributions of the precipitates is how to measure *in-situ* in the extracted electrolytic solutions. In the size distribution measurement for the dispersed particles in solutions, the light scattering method, laser diffraction (LD) method are generally used. But, it is well-known that the measured average diameter and size distribution are easily affected by the coarse particles in a same system. In other words, if the samples have the wide size distribution, incorrect information might be obtained. When the coarse and fine particles are co-existent, the existence of coarse particles are excessively evaluated because the intensity of scattering lights depends on the particle diameter [35].

To solve the above problems, the separation techniques are to be applied prior to the size measurement. In recent days, asymmetric flow field-flow fractionation (AF4) method is focused as the separation techniques for various nanomaterials such as proteins [36], polysaccharide [37], polymers [38], and metallic nanoparticles [39-41]. This technique is using the chromatographic separation, but has no fixed column of liquid chromatography (LC). In this section, the basic principle and applications for AF4 is described as follows.

Chapter 1: Introduction

1.3.1 The basic principle of AF4 method

    The field-flow fractionation method (FFF) was developed by Prof. J. Calvin Giddings in 1960s [42]. In this analytical method, samples are separated with depending on the diffusion coefficient of particles by applying the vertical and horizontal flows for the separation field. The advantages of FFF are a wide size range to be applied. Additionally, the low absorption amounts to the separation column with liquid phase are also achieved. In the past, this analytical instrument was more complicated and not more versatile than other separation techniques such as size exclusion chromatography (SEC), capillary gel electrophoresis (CE), and LC. Thus, the popularization of FFF as a separation and analytical method was delayed. However, nowadays, the versatile instrument is marketed from Wyatt Technology Corporation and Postnova Analytics, the reliable data about the size distribution of nanoparticles is getting to be obtained by relatively easy operating procedures. In the FFF separation field, flow field, magnetic field, centrifugal field, and thermal slope field are used. Herein, the asymmetric flow FFF (AF4) used as most versatile method is explained in details.

    At first, the schematic of separation field in AF4 instruments are shown in Fig. 1-15. The separation unit (which is called as AF4 separation channel) makes a thin layer to separate nanoparticles by inserting a spacer with a certain thickness between upper and lower plates. Because only the lower plate adopts a porous frit structure, only the cross flow is ejected outside without losing samples by inserting the ultrafiltration membrane under the spacer. Furthermore, the Reynolds number is approximately several hundred when the mobile phase is flowed to the horizontal direction of this thin layer.
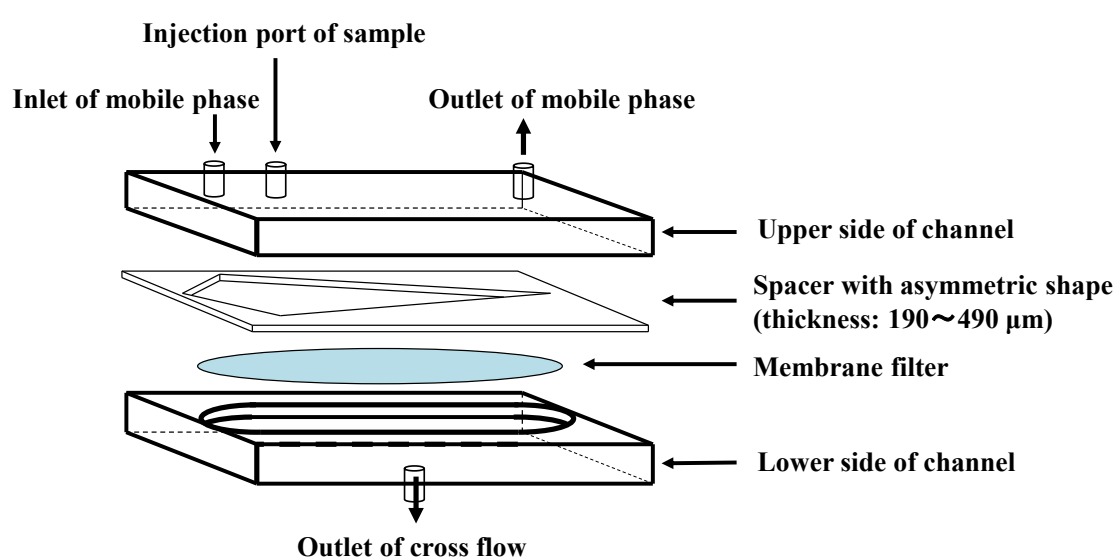
Fig. 1-15 Diagram of the AF4 separation field units [43].

<u>Chapter 1: Introduction</u>

Next, the mechanism of nanoparticle separation is shown in Fig. 1-16. Firstly, sample is injected from injection port as shown in Fig. 1-16 (a). After that, the focusing step is conducted in the AF4 separation channel (Fig. 1-16 (b)). In this time, the mobile phase is flowed from the both sides in the AF4 separation channel (which is called as focus flow), sample is focused at the constant position. Moreover, the cross flow is carried by pulling from the lower side of channel using HPLC pump. This vertical flow promotes to carry nanoparticles to lower side of the AF4 separation channel and all the nanoparticles settle down on the ultrafiltration membrane with passing a certain time. Also, it is well-known that the diffusion coefficients of nanoparticles are dependent on their size according to the following Stokes-Einstein's equation (Eq. 1-5).

$$R_h = \frac{kT}{6\pi\eta D} \qquad \text{(Eq. 1-5)}$$

where R_h is the hydrodynamic radius, η is the viscosity of solvent, k is Boltzmann constant, and T is the absolute temperature.

Once the concentration slope of nanoparticles is occurred by their sedimentation in the AF4 separation channel, the nanoparticles are going to diffuse to the direction of low concentration against the force from the vertical direction. In this time, the smaller size of nanoparticles gets, the stronger diffusion becomes, and it is resulting in moving far from the ultrafiltration membrane. On the other hand, the larger size of nanoparticles gets, the weaker diffusion becomes, and it is resulting in staying near the ultrafiltration membrane as shown Fig.1-16 (c). As mentioned above, samples are separated to the vertical direction in proportion to the diffusion coefficient which is dependent on the particle size. This step is called as relaxation step. Finally, the direction of channel flow is changed to only the outlet of AF4 separation channel as shown Fig.1-16 (d). Because the flow is laminar, the smaller particles become, the faster particles move. Thus, it can be eluted sequentially from the smaller particles. This step is called as elution step.

AF4 method is the separation technique by only the difference among the diffusion coefficients of nanoparticles in a liquid phase. Here, the elution time of each nanoparticle (which is called a retention time) is defined as Eq.1-6 [45]. Additionally, Eq. 1-7 is obtained by substituting Eq. 1-5 to Eq. 1-6.

Chapter 1: Introduction

$$t_R = \frac{w^2}{6D} \ln\left(1 + \frac{V_c}{V_0}\right) \qquad \text{(Eq. 1-6)}$$

where t_R is retention time, w is the thickness of spacer, D is the diffusion coefficient, V_c is the cross flow rate (vertical), V_0 is channel flow rate (horizontal)

$$t_R = \frac{w^2 R_h \pi \eta}{kT} \ln\left(1 + \frac{V_c}{V_0}\right) \qquad \text{(Eq. 1-7)}$$

It is obvious that the smaller the hydrodynamic radius becomes, the faster the retention time is in the AF4 method. As shown in these equations, there are many operating parameters which are composed of the thickness of spacer w, the cross flow rate V_c, and the channel flow rate V_0, the viscosity of solvent η and the absolute temperature T. Thus, it is very versatile methods for particles with the wide range size because the proper operating conditions are readily changeable to the physical and chemical properties of samples.
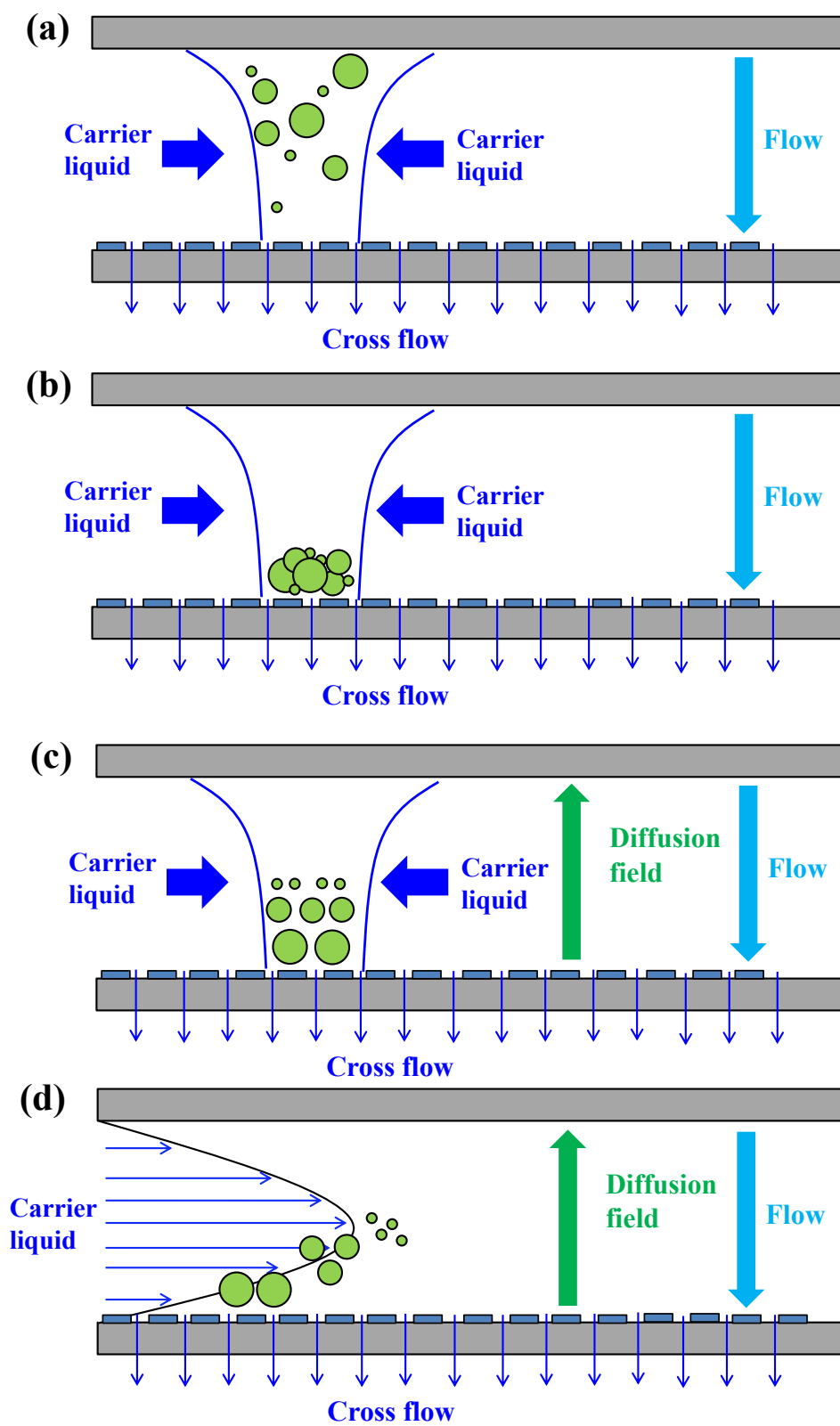
Fig. 1-16 The mechanism of nanoparticle separation in AF4 (a→d).

a. injection step, b. focusing step, c. relaxation step, d. elution step [44].

Chapter 1: Introduction

1.3.2   How to detect the particle in AF4 measurement

The various detection methods are able to be combined with AF4. There are light scattering method, UV absorption method, reflective index method and inductively coupled plasma-mass spectrometry (ICP-MS). In this sub-section, the detection method is explained as follows.

(1) Light scattering (LS) method

The light scattering (LS) method is the most general to measure polymer, proteins and nanomaterials. In this method, the lights irradiated from He-Ne laser (λ = 632.8 nm) hits the samples in a liquid phase. The lights are scattered to various directions and these scattered lights are analyzed. The size information is obtained from the results of analysis for the scattered lights. It must be carefully considered that the coarse samples are apt to be evaluated excessively because the intensity of the scattering lights is proportional to the squares of volume of samples. Especially, it is well-known that if the aggregates are contained much or there are equivalent of coarse particles and fine particles in a same system, the fine primary particles are often not detected. However, above problems are improved because the AF4 method can separate these mixed particles prior to the detection.

Additionally, in the case of high concentration of samples, the scattering light from a particle may hit to another particle (which is called a multiple scattering), resulting in the measurement error. Compared to only the LS measurement, AF4-LS method can improve this phenomenon by diluting the samples in the AF4 separation channel. Anyway, the sample concentration is recommended to investigate in advance.

The LS method is classified to two types of methods such as dynamic light scattering (DLS) and static light scattering (SLS). The former is how to measure the intensity change of scattering lights during a short time. The change is proportional to the diffusion coefficient of particles caused by the Brownian motion in a liquid phase. Using the estimated diffusion coefficient from the scattering light intensity and autocorrelation function G (τ), the hydrodynamic radius can be calculated from Stokes-Einstein's equation (Eq.1-5) [46]. However, it is not suitable to combine AF4 from following reasons. The DLS method measures the change of scattering light intensity and need certain duration time to measure. Thus, DLS online measurement on AF4 method brings the depression of size resolution and signal-noise (S/N) ratio.

On the other hand, the latter one is how to measure and analyze the average intensities of the scattering lights. In the case of nanometer-order samples, their sizes are much smaller than the wavelength of lights and Rayleigh scattering model can be applied. The second virial coefficient is calculated according to the Zimm's equation (Eq. 1-8) [47]. Here, the second virial coefficient is the parameter which indicates an excluded volume effect of polymer and their dispersibility.

Chapter 1: Introduction

$$\frac{Kc}{R(\theta)} = \frac{1}{M_w P(\theta)} + 2A_2 c \qquad \text{(Eq. 1-8)}$$

where c is sample concentration, M_w is the weight average molecular weight, A_2 is the second virial coefficient, $R(\theta)$ is the excessive Rayleigh ratio at an angle θ, $P(\theta)$ is the intramolecular interference factor, K is the optical constant.

To mention the molecular weight, intramolecular interferences of scattering lights could not occur and $P(\theta)$ becomes 1. Therefore, Eq. 1-8 is transformed to Eq.1-9.

$$\frac{Kc}{R(0)} = \frac{1}{M_w} + 2A_2 c \qquad \text{(Eq. 1-9)}$$

where $R(0)$ is the excessive Rayleigh ratio at $\theta = 0$.

From the Eq. 1-9, the weight average molecular weight of samples in a solution by using $R(0)$, c, K and A_2. Here, the optical constant K is shown in Eq. 1-10.

$$K = \frac{4\pi^2 \left(\mathrm{d}n/\mathrm{d}c\right)^2 n_0^2}{N_a \lambda^4} \qquad \text{(Eq. 1-10)}$$

where $\mathrm{d}n/\mathrm{d}c$ is the increment of refractive index by sample concentration, n_0 is the refractive index of solvent, N_a is the Avogadro number, λ is the wavelength of light source.

If applied this method, not only molecular weight and the second virial coefficient, but also the turning radius R_g of solute molecules and particles in a liquid solution are able to be evaluated. The scattering lights indicate different intensities between the front and back of particles for a proceeding direction of incident light. Here, the dependence on the angle for light scattering is dependent on their turning radius R_g. This is because the influence of Mie scattering which has angle dependence of scattering lights becomes larger than Rayleigh scattering which shows an isotropic scattering with increasing the size of particle. Thus, R_g is estimated using the intramolecular interference factor $P(\theta)$ (Eq. 1-11).

$$\lim_{\theta \to 0} \frac{1}{P(\theta)} = 1 + \frac{16\pi^2}{3\lambda^2} R_g^2 \sin^2(\theta/2) = 1 + \frac{\mu^2}{3} R_g^2 \qquad \text{(Eq. 1-11)}$$

where R_g is the turning radius, μ is the absolute value of scattering vector. Here, μ shows as following equation (Eq. 1-12).

$$\mu = \frac{4\pi n_0}{\lambda} \sin(\theta/2) \qquad \text{(Eq. 1-12)}$$

Additionally, if the interference of light scattering between different particles can be ignored, that is $c = 0$, Eq. 1-8 is able to be shown as Eq. 1-13 at a fully low angle.

$$\left(\frac{Kc}{R(\theta)}\right)_{c=0} = \frac{1}{M_w} + \frac{16\pi^2}{3\lambda^2} \frac{1}{M_w} R_g^2 \sin^2(\theta/2) \qquad \text{(Eq.1-13)}$$

The R_g is able to be estimated by calculating the dependence of the scattering light from samples and measuring the slope of this function. As mentioned above, it is required the Zimm's plot for the estimation of excessive Rayleigh ratio at $\theta = 0$ and $c = 0$ by measuring the dependence of concentration and angle of scattering lights in the SLS method. To make the Zimm's plot, the scattering lights from some samples of well-known concentration are measured at multi-angles and the acquired data should be plotted (Fig. 1-17). Each excessive Rayleigh ratio is extrapolated at $\theta = 0$ and $c = 0$, respectively from following functions; the slope of sample concentrations and angles. The two extrapolation lines are corresponding to Eq. 1-9 and Eq. 1-13. Thus, the intercept shows the molecular weight and the slope shows A_2 and R_g.
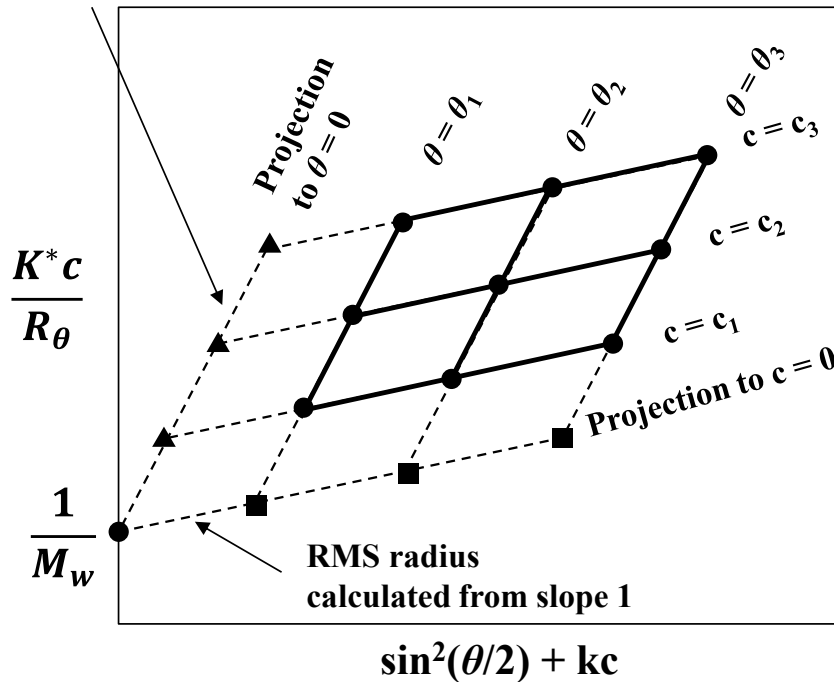

Fig. 1-17 Zimm's plot [48].

Chapter 1: Introduction

The angle dependence of scattering lights from particles is able to be measured by multi angle light scattering detector (MALS). This detector can measure simultaneously at 18 angles and it is useful for flow analysis hyphenated to chromatographic instruments such as AF4 and liquid chromatography (LC). Because the sample concentration is fully diluted in the separation channel In case of the flow analysis, the detected sample concentration is able to be approximated $c = 0$. Thus, the molecular weight and turning radius is estimated from the intercept and slope of the Debye plot which is made by the relationship between $\sin^2(\theta/2)$ and Kc/R (θ) in each retention time. Additionally, when the estimated molecular weight and turning radius is superimposed on the chromatogram, the molecular weight and turning radius distribution is able to be made. SLS method is suitable to the flow analysis such as AF4 which needs chromatographic hyphenation. However, the intensity of Rayleigh scattering light is proportion to the 6th power of the particle diameter. In many cases, the particle diameter under the 40 nm is not detectable because the particle diameter becomes under one tenth of the laser wavelength.

Also, DLS method can detect particles under 10 nm, but it is not suitable to the flow analysis. From the view of sensitivity and analytical precision, a batch measurement is generally conducted now. Therefore, the SLS method is most suitable to the particle detection system of AF4 among laser scattering methods, however, there is a problem for fine particles measurement.

(2) UV-vis absorption method

The ultraviolet (UV) and visible absorption (UV-vis) method is based on the Lambert–Beer law. The lights are absorbed to the substances in case of passing through substances. This method uses UV light (wavelength: $200 \sim 360$ nm) and visible light (wavelength: $360 \sim 780$ nm). This method is possible to measure at a short duration time. The continuous measurement in a time resolved-analysis often is able to use this method to investigate the kinetics of various reactions. Also, nanoparticles in a liquid solution often induce the characteristic light absorption phenomenon which is called as local surface plasmon resonance (LSPR) [49]. When the diameter of metallic nanoparticles becomes smaller than the wavelength of incident light, plasmon is localized around nanoparticles. If the absorption wavelength is within the visible regions, particle-specific color is observed. Thus, this method is suitable to detect ultra-fine particles and capture time changes of particle concentration. In advance, it is considered that a higher time-resolved flow analysis could be possible by selecting wavelength for target particles.

However, there are two disadvantages to apply UV-vis to AF4 analysis. Firstly, the elemental information is not analyzed in this method. It is necessary to identify the elemental composition

<u>Chapter 1: Introduction</u>

of particles by using other characterization methods in advance. Next, the diameter of particles is not determined directly unlike LS methods. If particles are larger than 40 nm, the diameter of particles is possible to be determined simultaneously by AF4-MALS measurements. Otherwise, other information is required such as TEM, SEM, DLS (batch analysis). Therefore, AF4 instruments are generally equipped with MALS and UV-vis system.

(3) Hyphenation to ICP-MS

Recently, AF4 is often connected to ICP-MS to measure the elemental composition of samples. In 1999, M. Hassellöv reported firstly that the on-line connection between AF4 and ICP-MS was conducted for the analysis of colloid particles in natural water [50]. At that time, the mixing module was installed between the outlet of AF4 and inlet of ICP-MS in order to dissolve separated samples by acid and add internal standards. It was obvious that not detected colloids by UV detection were detected successfully by hyphenated ICP-MS. After this, many studies on AF4-ICP-MS analysis were conducted in many fields such as metallic nanoparticles, mineral samples and environmental samples [51-55]. Also, it is considered that the above mixing module is not suitable to a highly sensitive detection of nanoparticles due to the dilution by acidic solutions. Thus, the recent AF4-ICP-MS system is constructed without mixing module.

However, there are some problems in direct connection between AF4 and ICP-MS. Firstly, A. R. Poda reported that the hydrodynamic diameter of silver nanoparticles evaluated by AF4-ICP-MS is relatively coincident to DLS evaluation results and not coincident to that of TEM [54]. That is, with decrease in size of particles, AF4-ICP-MS is apt to overestimate their size. For accurate size measurement, it is required to investigate this point more in details.

Secondly, it was also reported that the variability of signal intensity became bigger with increase in size of silver particles. In this case, the sample transport efficiency to ICP plasma and ionization efficiency in ICP plasma must be considered carefully. Unlike the general ICP-MS analysis, undissolved samples are transported and ionized in direct connection method in AF4-ICP-MS. As a matter of course, the particle size is influenced to their efficiencies. H. Prestel reported that monodisperse silica colloid particles under 500 nm are completely ionized [56]. Also, D.M.Murphy reported that the coarse particles over than 2 μm had the size dependence for the degrees of ionization [57]. On the other hand, sample transport efficiency is not understood well. For the accurate quantitative analysis of separated particles in AF4, this issue needs to be investigated more.

Chapter 1: Introduction

1.4 Aim of this research

The primary aim of the present research was to develop the analytical method of various nanoparticles (precipitates) whose sizes are ranged from several nanometers to several hundred nanometers in steels with regard to their size, number concentration and elemental composition. The basic strategy in this research was summarized as follows.

1. In order to obtain the representative information of these precipitates in steels, the macroscopic analysis method (e.g. chemical analysis), which is needed a large amount of sample, was adopted.

2. The SPEED method was used for the selective extraction of precipitates in steels. The extracted precipitates were dispersed in the electrolytic solution and the dispersed solution was measured directly.

3. The separation technique by their sizes of precipitates, and elemental analysis were necessary for the measurement of mixture of various kinds and/or sizes of the precipitates.

4. The analytical method by combining selective extraction technique (SPEED), size separation technique (AF4) and highly sensitive elemental analysis method (ICP-MS) of precipitates mentioned above were investigated for the evaluation of steels.

This thesis was comprised 6 chapters as shown Fig. 1-18. The findings were summarized as follows.

Chapter 1 described the background of this study and its objectives. Firstly, the outline of steel manufacturing process and the way of the steel products design using nanoparticles were introduced to be understood the necessity of nanoparticles measurement in steels. Secondly, the conventional analytical methods for nanoparticles in steels and their problems were explained well. Thirdly, the AF4 method as a new analytical technique for measurement of nanoparticles in steels was reviewed about the principles of separation, measurement method and their problems for the evaluation of steel products. Finally, our objective was summarized in this section.

In Chapter 2, the accurate analysis method for sulfides in steels was investigated. In SPEED method, when the copper ions and manganese sulfides co-existed, these reacted chemically and copper sulfides (Cu_xS) were generated in an electrolytic solution. The Cu_xS was not originally existed in steels and the incorrect analytical results were obtained. In order to solve this problem, the addition of triethylenetetramine (TET) to the electrolytic solution was effective as a copper ion masking agent by chelating copper ions more stably. The details and working mechanisms of chelating agent were discussed in Chapter 2.

In Chapter 3, the accuracy of nanoparticles measurement using AF4-ICP-MS was investigated. The gold nanoparticles were measured by three analytical methods, AF4-ICP-MS,

Chapter 1: Introduction

TEM, and SAXS. According to these evaluation results, the size distribution measured using AF4 were broadened almost twice than others. The correction method for the width of size distribution were developed and applied to niobium carbide nanoparticles in steels.

In Chapter 4, the improvement of sample transport efficiency in ICP-MS was investigated. Focused on the aerosol size of samples generated by ICP-MS nebulizer, mistral desolvation (MD) system was applied to ICP-MS analysis. MD system was equipped with heating and cooling system of aerosols. It was clarified that the aerosol size became in decrease by using MD. Additionally, in case of the application to nanoparticles dispersed solution, the sample transport efficiency was improved dramatically at the size over 100 nm.

In Chapter 5, the detection sensitivity for titanium carbide and vanadium carbide in steels using AF4-ICP-MS was investigated. The sulfur involved in eluent of AF4 caused the mass spectral interferences with titanium and vanadium. Thus, other surfactants were explored. Various surfactants were evaluated using DLS, zeta potential measurements, and AF4-ICP-MS. It was clarified that the sodium cholate met the separation ability in AF4 and avoided the spectral interferences. The details were discussed in Chapter 5.

Chapter 6 summarized the main results and findings in this study.

Chapter 1. Introduction

↓

Sample preparation process for the analysis of steels

↓

Chapter 2.
Development of analysis method for sulfide in steel with chelating agent of copper

↓

Separation & analysis method for nanoparticles in steels

Chapter 3.
Determination of size distribution of nanoparticles using asymmetric flow field-flow fractionation (AF4)

Size measurement

Sensitivity improvement

Chapter 4.
Improvement of sample introduction efficiency for ICP-MS using the mistral desolvating sample introduction method

Application to TiC, VC nanoprecipitates in steels

↓

Chapter 5.
Development of sulfur-free surfactant for titanium and vanadium nanoparticle characterization in steel using AF4-ICP-MS

↓

Chapter 6. General conclusions

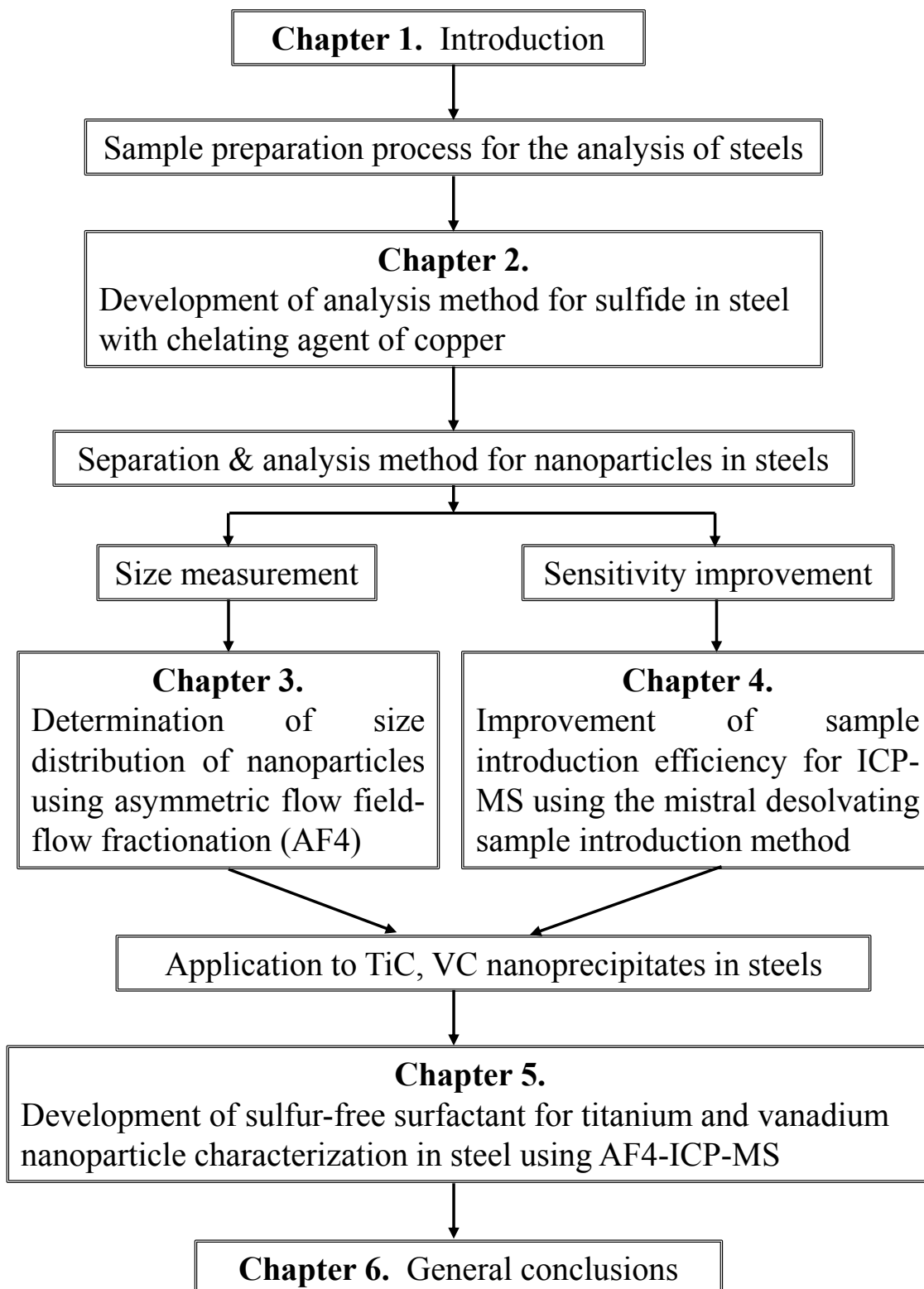Fig. 1-18 Construction of this study.

Chapter 1: Introduction

1.5 References

1. T. Maki: "*Recent Progress in Microstructure Control of Steels*", Materia Japan, **36**(1997), 937.

2. T. Maki: "*Phase Transformations in Steel －Martensite Transformation Ⅰ: Characteristic of Martensite Transformation in Ferrous Alloys*", Materia Japan, **54**(2015), 557.

3. Nippon steel HP, https://www.nipponsteel.com/product/sheet/process/

4. Y. Okuno: *Nippon Steel Monthly*, **135**(2004), 11.

5. T. Matsumiya: *Nippon Steel Monthly*, **138**(2004), 11.

6. T. Matsumiya: *Nippon Steel Monthly*, **140**(2004), 5.

7. R. W. K. Honeycombe: *Met. Sci.*, **14**(1980), 201.

8. W. B. Morrison: *J.ISI*, **201**(1963), 317.

9. Y. Funakawa: *J. Japan Inst. Met. Mater.*, **81**(2017), 447.

10. N. Kamikawa, Y. Abe, G. Miyamoto, Y. Funakawa, and T. Furuhara: *ISIJ Int.*, **54**(2014), 212.

11. M. F. Ashby: *Philos Mag.*, **14**(1966), 1157.

12. M. F. Ashby: "*Physics of Strength and Plasticity*", MIT Press, Massachusetts, **113**, (1969).

13. T. Gradman: "*The Physical Metallurgy of Microalloy Steels*", Maney Publishing, London, **47**, (2002).

14. A. Kojima, A. Kiyose, R. Uemori, M. Minagawa, M. Hoshino, T. Nakashima, K. Ishida, and H. Yasui: *Nippon Steel Technical Report*, **90**(2004), 2.

15. C. Zener, quoted by C. Smith: *Trans. AIME*, **175**(1948), 15.

16. T. Nishizawa, I. Ohnuma, and K. Ishida: *Mat. Trans. JIM.*, **38**(1997), 950.

17. M. Sugiyama: *Electron-microscopy*, **37**(2002), 167.

18. F.G. Wei and K. Tsuzaki: *Metall. Mater. Trans.A*, **37A**(2006), 331.

19. X.-L. Li, X.-T. Deng, C.-S. Lei, and Z.-D.Wang: *Scr. Mater.* **163**(2019), 101.

20. K. Narita: *Tetsu-to-Hagané*, **60**(1974), 1820.

21. K.Kawamura, S.Watanabe, and S.Suzuki: *J. Jpn. Inst. Met.*, **32**(1968), 375.

22. K.Kawamura, S.Watanabe, and S.Suzuki: *J. Jpn. Inst. Met.*, **32**(1968), 180.

23. S.Wakamatsu: *Tetsu-to-Hagané*, **55**(1969), 503.

24. K.Kawamura, S.Watanabe, and S.Suzuki: *Tetsu-to-Hagané*, **58**(1972), 2067.

25. H. F. Beeghly: *Anal. Chem.*, **21**(1949), 1513.

26. R.Wasmuht and P.Oberhoffer: *Arch. Eisenhüttenw.*, **2**(1929), 829.

27. R. Treje and C.Benedicks: *J. Iron Steel Inst.*, **128**(1933), 205.

28. P. Klinger and W.Koch: *Arch. Eisenhüttenw.*, **11**(1938), 569.

29. F. Kurosawa: *Zairyo-to-Kankyo*, **48**(1999), 405.

Chapter 1: Introduction

30. K. Takimoto, Y. Taguchi, and R. Matsumoto: *J. Jpn. Inst. Met.*, **40**(1976), 834.

31. K.Narita: *Tetsu-to-Hagané*, **73**(1987), 67.

32. S. Suzuki, S. Watanabe, H. Yasuda, and H. Sato: *Tetsu-to-Hagané*, **64**(1978), S362.

33. F. Kurosawa: *Surf. Interface Anal.*, **12**(1988), 203.

34. T. Akiyoshi, Y. Ishibashi, O. Inamoto, H. Uchihara, H. Kurayasu, S. Suzuki, T. Takayama, M. Narita, K. Fujimoto, K. Mizukami, Y. Mitsuo, K. Miyazawa, and T. Mochizuki: *Shiryou Bunseki Kouza: Tekko Bunseki [Sample Analysis Course: Steel analysis]*, (Maruzen Publishing, 2011), 97.

35. E. Tomaszewska, K. Soliwoda, K. Kadziola, B. Tkacz-Szczesna, G. Celichowski, M. Cichomski, W. Szmaja, and J. Grobelny: *J. Nanomaterials*, **60**(2013), 1.

36. M. Marioli and W. Th. Kok: *Anal. Bioanal. Chem.*, **411**(2019), 2327.

37. C. Fuentesa, H. Saari, J. Choi, S. Lee, M. Sjöö, M. Wahlgren, and L. Nilsson: *Carbohydrate Polymers*, **206**(2019), 21.

38. C. Fuentes, J. Choi, C. Zielke, J. M. Peñarrieta, S. Lee, and L. Nilsson: *Analyst*, **144**(2019), 4559.

39. A.R. Poda, A.J. Bednar, A.J. Kennedy, A. Harmon, M. Hull, D.M. Mitrano, J.F. Ranville, and J. Steevens: *J. Chromatogr. A*, **1218**(2011), 4219.

40. B. Schmidt, K. Loeschner, N. Hadrup, A. Mortensen, J. J. Sloth, C. B. Koch, and E. H. Larsen: *Anal. Chem.*, **83**(2011), 2461.

41. N. Bendixen, S. Losert, C. Adlhart, M. Lattuada, and A. Ulrich: *J. Chromatogr. A*, **1334**(2014), 92.

42. J. C. Giddings: *Sep. Sci.*, **1**(1966), 123.

43. K. Watanabe: *Bunseki*, **5**(2014), 208.

44. H. Kato: *AIST Technical Note*, **6**(2007), 185.

45. K.-G. Wahlund and J.C. Giddings: *Anal. Chem.*, **59**(1987), 1332.

46. K. Shiba: *Polyfile*, **47**(2010), 35.

47. B.H.Zimm: *J.Chem.Phys.*, **16**(1948), 1093.

48. M. Odaka: *Seibutu-kougaku Kaishi*, **89**(2011), 398.

49. A. J. Haes, S. Zou, G. C. Schatz, and R. P. V. Duyne: *J. Phys. Chem. B*, **108**(2004), 109.

50. M. Hasellöv, B. Lyvén, C. Haraldsson, and W. Sirinawin: *Anal. Chem.*, **71**(1999), 3497.

51. E. Bolea, F. Laborda, and J.R. Castillo: *Anal. Chim. Acta*, **661**(2010), 206.

52. M. Bouby, H. Geckeis, and F. W.Geyer: *Anal. Bioanal. Chem.*, **392**(2008), 1447.

53. E. Bolea, M.P. Gorriz, M. Bouby, F. Laborda, J.R. Castillo, and H. Geckeis: *J. Chromatogr. A*, **1129**(2006), 236.

54. A.R. Poda, A.J. Bednar, A.J. Kennedy, A. Harmon, M. Hull, D.M. Mitrano, J.F. Ranville, and J. Steevens: *J. Chromatogr. A*, **1218**(2011), 4219.

55. B. Schmidt, K. Loeschner, N. Hadrup, A. Mortensen, J. J. Sloth, C. B. Koch, and E. H. Larsen: *Anal. Chem.*, **83**(2011), 2461.

56. H.Prestel, L.Schott, R. Niessner, and U.Panne: *Water Res.*, **39**(2005), 3541.

57. D.M.Murphy, J.R.Garbarino, and H.E.Taylor: *J. Chromatogr. A*, **517**(1990), 435.

Chapter 2

Development of analysis method for sulfide in steel with chelating agent of copper

Chapter 2: Development of analysis method for sulfide in steel with chelating agent of copper

Chapter 2. Development of analysis method for sulfide in steel with chelating agent of copper

2.1 Introduction

This Chapter 2 was focused on the sulfide analysis in steels. The sulfides are known as chemically unstable particles in solutions and there are problems to extract the sulfides stably from steels. It was recommended to use 4 (v/v) % methyl salicylate-1 (w/v) % salicylic acid-1 (w/v) % TMAC-methanol (4% MS electrolyte) for sulfides in the past report [1].

However, of the particles, the unclear point had been reported about the observation and analysis of copper sulfides (Cu_xS) [2-9]. Several authors reported that when steels were rapidly cooled from a high temperature of 1473 to 1573 K, and observed after the SPEED etching, copper sulfides were found abundantly precipitated [10-12]. This temperature range was higher than the precipitation temperature (about 973 K) predicted by thermochemical calculation programs such as FactSage [13]. In other words, the calculation results did not agree with the experimental results. J. Tan and P.C. Pistorius [2] reported that these copper sulfides were formed because MnS stable in the steel matrix becomes unstable and easily decomposable in an aqueous solution. Additionally, because Cu^{2+} ion easily forms sulfides in an aqueous solution in the presence of S, it reacts with MnS in a methanol (non-aqueous solvent) electrolyte, which has the characteristics similar to an aqueous solution, resulting in forming artificial sulfides.

Here, in this Chapter 2, it was investigated that the mechanism that sulfides (named as artificial sulfides), which is not present in the steel matrix, are newly formed in the process of SPEED method. Moreover, an electrolyte and an electrolysis method capable of preventing the formation of artificial sulfides were developed. The results are reported below.

2.2 Experimental

Table 2-1 shows the chemical composition of the hot-rolled sheet steel used as sample material in the experiment. Hot-rolled steel sheet samples were mirror polished and observed by SEM-EDX.

Table. 2-1　Chemical composition of steel sample

Element	C	Si	Mn	S	Cu
weight %	0.07	3.3	0.1	0.025	0.07

Chapter 2: Development of analysis method for sulfide in steel with chelating agent of copper

    A JEOL JSM-7001F Schottky field emission scanning electron microscope (FE-SEM) was operated with a working distance of 10 mm and an acceleration voltage of 15 kV. Auger electron spectroscopy was performed with a PHI 700 field emission Auger electron spectroscope (FE-AES) at an electron beam voltage and current of 10 kV and 10 nA, respectively, and an argon ion beam voltage of 2 kV. The Fujiwara Scientific Speed Analyzer FV-138 was used as an electrolytic etcher. The estimation of the sputtering rate in the depth direction was performed by using Si/SiO_2 as standard materials. The sputtering depth converted into that of a thin SiO_2 film was adopted. The atomic weight ratio was calculated by eliminating the effect of oxygen on the oxidation of the sample surface. A quantitative analysis was conducted with a Shimadzu ICPS-8100 ICP emission spectrometer at measurement wavelengths of 257.610 nm for Mn and 327.396 nm for Cu. Table 2-2 summarized sample preparation methods, electrolytes and electrolysis conditions. The amounts of steel sheet electrolyzed were set to 30 C for SEM observation of the surface to be mirror polished and 3456 C, equal to be approximately 1 g of steel sheet, for quantitative analysis. The electrolyte was filtered after the SPEED method with a 0.2 μmφ pore size polycarbonate filter under the No. 9 electrolysis conditions (conventional) in Table 2-2. In case of the developed method, a polytetrafluoroethylene (PTFE) filter was adopted an operated under the No. 10 electrolysis conditions in Table 2-2.

Chapter 2: Development of analysis method for sulfide in steel with chelating agent of copper

Table. 2-2　Summary of electrolysis conditions

No.	Name	Surface finishing	Electtrolyte	Cu chelating agent	Added ion	Coulomb (C)	Filter
1	Mirror	mirror-polished	-	-	-	-	-
2	4%MS	mirror-polished	4%MS	-	-	30	-
3	10%AA	mirror-polished	10%AA	-	-	30	-
4	4%MS+Ag	mirror-polished	4%MS	-	Ag 20 μg mL^{-1}	30	-
5	4%MS+Cu	mirror-polished	4%MS	-	Cu 20 μg mL^{-1}	30	-
6	4%MS+5%TET	mirror-polished	4%MS	5 (v/v)% TET	-	30	-
7	4%MS+5%PEH	mirror-polished	4%MS	5 (v/v)% PEH	-	30	-
8	4%MS+5%EDTA	mirror-polished	4%MS	5 (v/v)% EDTA	-	30	-
9	4%MS (3456C)	polished	4%MS	-	-	3456	Polycarbonate 0.2 μm cut-off
10	4%MS+5%TET (3456C)	polished	4%MS	5 (v/v)% TET	-	3456	PTFE 0.2 μm cut-off

TMAC: tetra methyl ammonium chloride

4%MS: 4 (v/v) % methyl salicylate +1 (w/v) % salicylic acid + 1 (w/v) % TMAC + methanol

10%AA: 10 (v/v) % acetylacetone + 1 (w/v) % TMAC + methanol

TET: triethylene tetramine

PEH: pentaethylene hexamine

EDTA: ethylene diamine tetra acetic acid

2.3　Results and Discussion

2.3.1 Comparison between precipitation of sulfides after polishing and after electrolytic etching

Fig. 2-1 showed SEM-EDX maps of a hot-rolled steel sheet sample mirror polished under the No. 1 electrolysis conditions in Table 2-2.
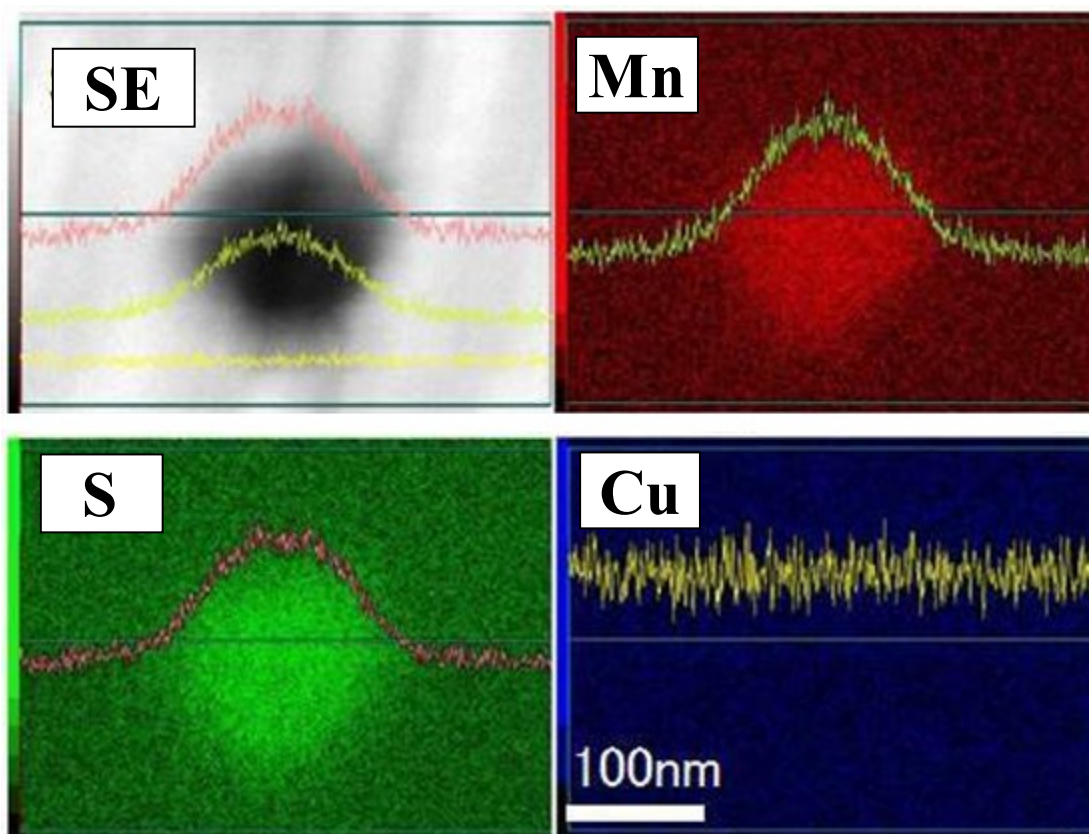
Fig. 2-1   SEM-EDX mapping of MnS particle after mirror-polishing.

When EDX element maps and intensity ratios of Mn, S and Cu are overlapped on a MnS particle about 150 nm in diameter, the Mn and S element maps are round, and the intensity ratios show a Gaussian distribution. This suggested that a strain-induced precipitation occurred when the steel sheet was hot rolled. Contrastingly, the EDX signal intensity of Cu is constant in the L direction. No change was confirmed in the signal intensity between the steel matrix and the particle. When the sample was polished and observed by SEM-EDX, the presence of Cu was not recognized around the MnS precipitated in the hot rolling process.

Next, Fig. 2-2 showed the secondary electron (SE) micrograph image and EDX element maps of a sample etched using 4%MS electrolyte under the condition of Table 2-2 No.2. A deposition of Cu was found in a top hat distribution around the MnS particle. Similar results were obtained when the electrolyte was changed to the No. 3 10%AA electrolyte in Table 2-2. Thus, it is estimated that the copper sulfide as shown in Fig. 2-2 is not originally present in the steel matrix. Additionally, the metallic copper dissolved as Cu^{2+} ion from the steel matrix into the electrolyte and Cu^{2+} ion made newly artificial sulfide in the MnS surface layer.
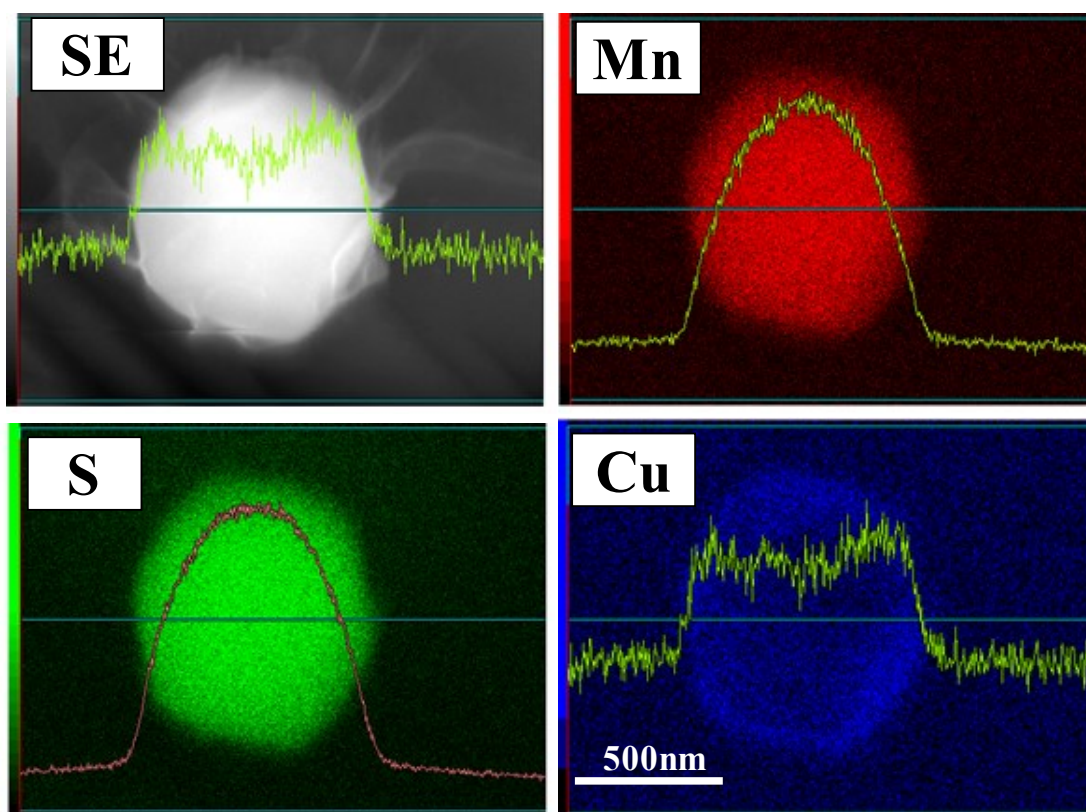
Fig. 2-2   SEM-EDX mapping of MnS particle after SPEED etching with 4%MS electrolyte.

2.3.2   Verification of artificial sulfide formation mechanism

Assuming that whether the sulfide formation reaction to occur would depend on the solubility product difference between sulfides, we calculated the solubility product constant [14] (K_{sp}) digit difference (δpK_{sp}) between the sulfides as shown by Eq. 2-1. The calculated values were shown in Table 2-3. It is estimated that the greater the δpK_{sp} value, the more easily the artificial sulfides are formed. Eq. 2-1 gives an example of how to calculate the δpK_{sp} value for MnS and CuS.

$$\delta pK_{sp}= pK_{sp}(CuS)-pK_{sp}(MnS) = 22.6 \qquad \text{(Eq. 2-1)}$$

where the K_{sp} values of the sulfides in an aqueous solution at 25°C were used as follows.

$$K_{sp}(MnS) = 3 \times 10^{-14}, K_{sp}(CuS) = 8 \times 10^{-37}$$

Chapter 2: Development of analysis method for sulfide in steel with chelating agent of copper

Table. 2-3   Solubility products of sulfides (K_{sp} value) in aqueous solution at 298 K and the difference in pK_{sp} ($-\log_{10} K_{sp}$) of the solubility product between sulfides

No.	Compound	Formula	K_{sp} (298 K)	pK_{sp}	HgS	Ag$_2$S	CuS	PbS	CdS	CoS	NiS	ZnS	Tl$_2$S	FeS
	pK_{sp} →				-53.7	-50.1	-36.1	-27.5	-27.0	-25.5	-24.9	-24.7	-21.2	-18.1
1	Mercury(Ⅱ) sulfide (red)	HgS	2×10^{-54}	-53.7	0.0									
2	Silver (Ⅰ) sulfide	Ag$_2$S	8×10^{-51}	-50.1	3.6	0.0								
3	Copper (Ⅱ) sulfide	CuS	8×10^{-37}	-36.1	17.6	14.0	0.0							
4	Lead (Ⅱ) sulfide	PbS	3×10^{-28}	-27.5	26.2	22.6	8.6	0.0						
5	Cadmium sulfide	CdS	1×10^{-27}	-27.0	26.7	23.1	9.1	0.5	0.0					
6	Cobalt (Ⅱ) sulfide (beta)	CoS	3×10^{-26}	-25.5	28.2	24.6	10.6	2.0	1.5	0.0				
7	Nickel (Ⅱ) sulfide (beta)	NiS	1.3×10^{-25}	-24.9	28.8	25.2	11.2	2.6	2.1	0.6	0.0			
8	Zinc sulfide (alpha)	ZnS	2×10^{-25}	-24.7	29.0	25.4	11.4	2.8	2.3	0.8	0.2	0.0		
9	Thallium (Ⅰ) sulfide	Tl$_2$S	6×10^{-22}	-21.2	32.5	28.9	14.9	6.3	5.8	4.3	3.7	3.5	0.0	
10	Iron (Ⅱ) sulfide	FeS	8×10^{-19}	-18.1	35.6	32.0	18.0	9.4	8.9	7.4	6.8	6.6	3.1	0.0
11	Manganese (Ⅲ) sulfide (green)	MnS	3×10^{-14}	-13.5	40.2	36.6	22.6	14.0	13.5	12.0	11.4	11.2	7.7	4.6

To confirm whether these estimations can also be applied to sulfides in a methanol solution, we verified the reactions between Ag^+ ion and MnS. The steel sample was electrolytically etched under the No. 4 conditions in Table 2-2 and observed by SEM. Fig. 2-3 showed a SE micrograph of the sample and EDX element maps of Mn, S and Ag.
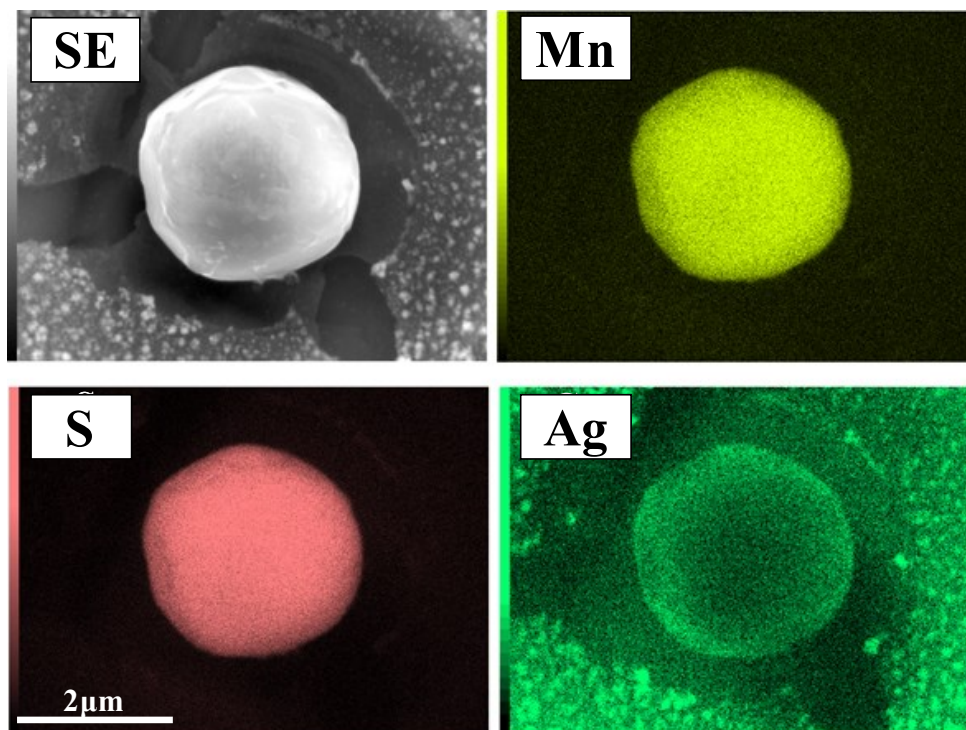
Fig. 2-3   SEM-EDX mapping of MnS particle after SPEED etching with 4%MS electrolyte and silver standerd solution (Ag 20 μg mL^{-1}).

It was confirmed that Ag was increased in concentration at the circumferential edge of the MnS particle and enriched on the MnS surface. At the center of the MnS particle, the Ag concentration is low, and the Mn and S concentrations are high. This suggested that the MnS surface alone was substituted by Ag. Therefore, it is inferred that if Ag^+ ion has a high δpK_{sp} value like Cu^{2+} ion, the sulfide formation reaction between it and MnS easily proceeds. It was confirmed that Pb, Co, Ni and Zn ions also similarly form artificial sulfides. In other words, if the solubility product constant digit difference (δpK_{sp}) between the sulfides is at least greater than 10, the sulfide formation reaction is thought to easily proceed within the time (about 2 to 3 hrs) taken to electrolyze about 1 g of the steel sample.

2.3.3   Verification of Ag infiltration by Auger Electron Spectroscopy

To verify whether artificial sulfides newly form in the surface layer of MnS or whether MnS dissolves, infiltrates and forms artificial sulfides, we performed element analysis of MnS surface by Auger electron spectroscopy. The surface layer of the MnS particle observed as shown in Fig. 2-3 was argon sputtered at depths of 1 nm interval. Fig. 2-4 plotted the Ar sputter depth (nm) along the horizontal axis and the atomic concentration (%) of S, Mn, Ag and Cu along the vertical axis.
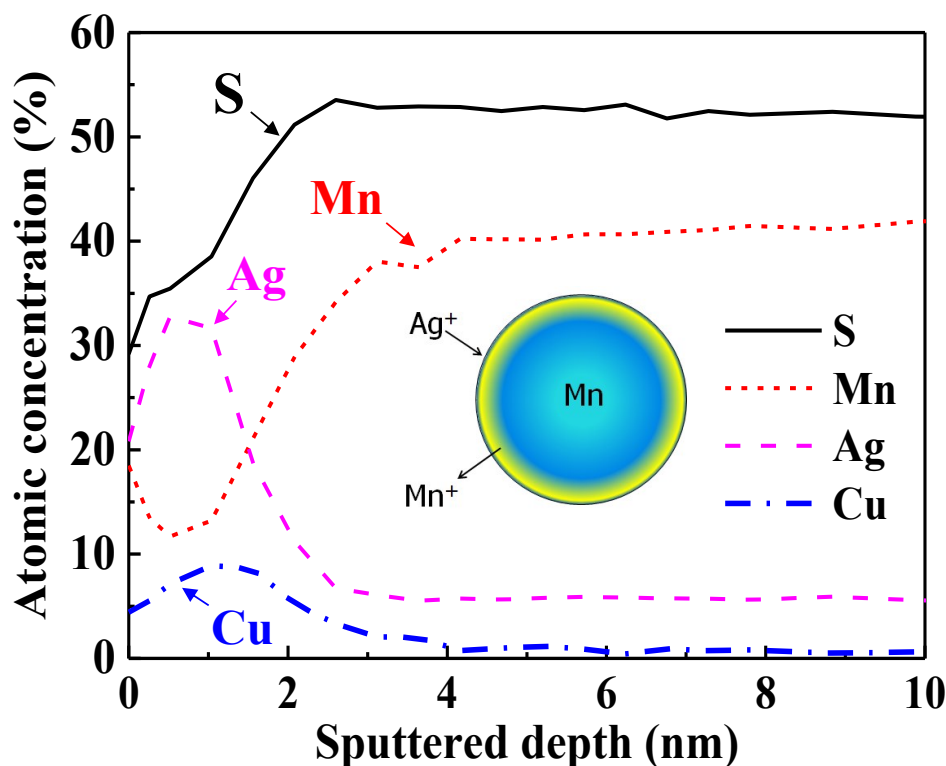
Fig. 2-4   Atomic concentration analysis of the surface of MnS particle by Auger electron spectroscopy.

Ag exhibited a maximum atomic concentration of 38% at about 1 nm depth in the MnS surface layer. Thereafter, its atomic concentration gradually decreased, and it infiltrated to a depth of about 100 nm. Contrastingly, the atomic concentration of Mn decreased in the surface layer of MnS. The atomic concentration of Cu increased nearly 10% in the surface layer of MnS, but the increase remained at about one third of that of the atomic concentration of Ag. Thus, the artificial sulfide formation reaction between metal ions and MnS is considered as the exchange reaction whereby MnS dissolves and Ag^+ and Cu^{2+} infiltrate to form sulfides.

2.3.4   Dependence of artificial sulfide formation on particle size

When a hot-rolled steel sheet sample was treated under the No. 2 electrolysis conditions in Table 2-2, a coarse MnS particle measuring a few micrometers and elongated horizontally (or in the L direction) was observed as shown at bottom left in Fig. 2-5(a) and fine particles 500 nm or smaller in size were observed as shown in a white-bordered area at top right in Fig. 2-5(a). Fig. 2-5(b) shows an element map where Mn and Cu are colored violet and blue, respectively. Consequently, most of the fine particles at top right were estimated to be Cu_xS. On the other hand, blue Cu_xS was formed in the surface layer of the coarse MnS particle (violet).
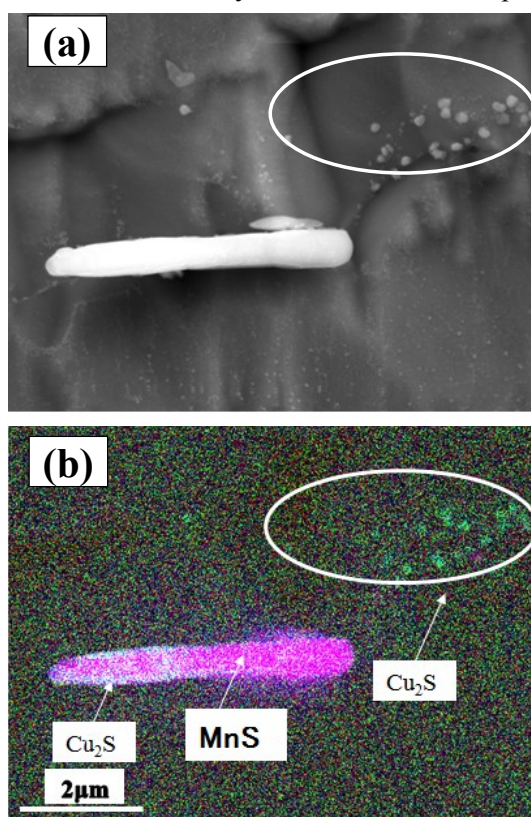
Fig. 2-5   SEM-EDX mapping of MnS particle after SPEED etching with 4%MS electrolyte, (a) Secondary electron image, (b) Elemental mapping by EDX. (Blue as Cu, Violet as Mn)

Chapter 2: Development of analysis method for sulfide in steel with chelating agent of copper

Next, the relationship between the MnS particle size and the immersion time in the artificial sulfide formation reaction was investigated. The samples were immersed in the No. 5 electrolyte in Table 2-2 for 10 to 1000 min, removed from the electrolyte, washed in methanol, air dried, and observed by FE-SEM. The observed particle size and the Mn/(Mn + Cu) mass content ratio calculated from the EDX elemental analysis values are shown along the horizontal and vertical axes, respectively, in Fig. 2-6.
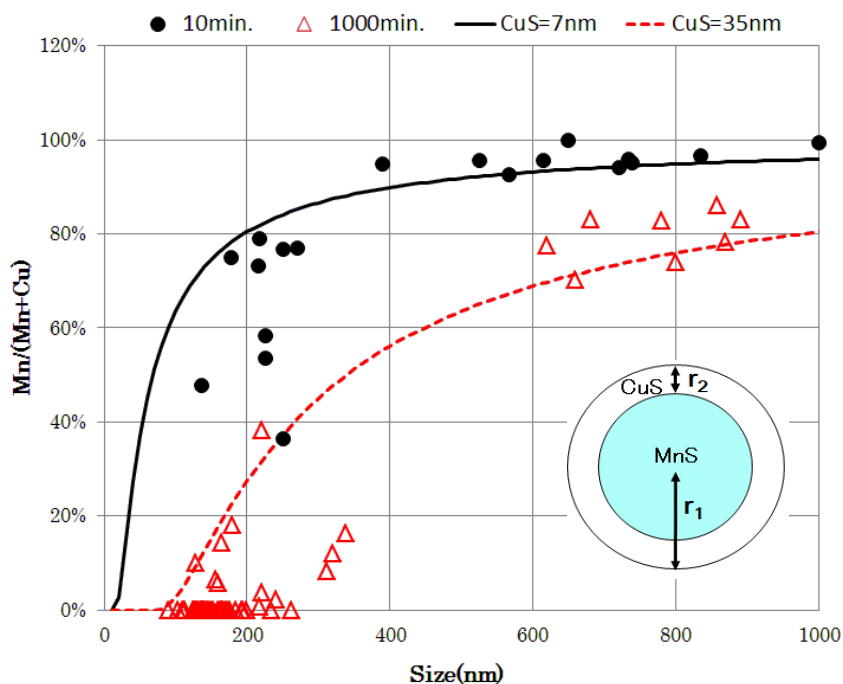
Fig. 2-6   Size dependence of Sulfide exchange reaction between MnS and Cu^{2+}.
(Dipping time: ● 10 minutes, △1000 minutes)

The values of the samples immersed for 10 and 1000 min are plotted by closed circles (●) and open triangles (△), respectively. The observed results showed that the longer the immersion time, the greater the infiltration depth and that the smaller the MnS particle size, MnS were converted easily to Cu_xS. We calculated the Mn/(Mn+Cu) mass content ratio and the Cu infiltration depth r_2 to fit the immersion time of 10 and 1000 min, respectively. In this case, it was presumed that the thickness r_2 of CuS alone have infiltrated into the surface layer of the MnS particle with the radius r_1 as the calculation model shown at bottom right of Fig. 2-6. The rate at which CuS diffused from the surface layer into the inside was assumed to be constant and the concentration gradient was not considered. From the calculated results, it was inferred that although there are some variations, at least about 7 nm (the solid line curve) and 35 nm (the broken line curve) of the about 200 nm MnS particle were converted to Cu_xS in the immersion time of 10 and 1000 min, respectively. Usually when the mirror-polished surface of the sample

is etched by the SPEED method and observed, Cu is detected in the MnS surface layer in many cases. As the MnS particle size decreases, the Cu content ratio increases. When the MnS particle size decreases below 50 nm, almost Cu and S alone are detected. Our present results are believed to support these results.

2.3.5   Study of prevention of artificial sulfide formation by Cu ion chelating agent

From the above results, we considered that the formation of artificial sulfides would be effectively prevented by trapping Cu^{2+} and other metal ions (excluding Fe) dissolved from the steel matrix with a chelating agent. Examples of chelating agents [15] that can selectively trap Cu^{2+} are shown in Table 2-4.

Table. 2-4   Stability constant between chelating agent and Cu ion

Chelating agent	Stability constant ($logK_{ML}$)
Pentaethylenehexamine (PEH)	26.2
Tetraethylenepentamine (TEP)	23.1
Triethylenetetramine (TET)	20.4
Ethylenediaminetetraacetic acid (EDTA)	18.3
Diethylenetriamine (DETA)	16.1
Ethylenediamine (EDA)	10.7
Iminodiacetic acid (IDA)	10.3
Ammonia (NH_3)	4.2

After studying various chelating agents soluble in organic solvents like methanol and exceptionally capable of trapping Cu^{2+}, we found that polyethyleneamine chelating agents such as, triethylenetetramine (TET), penicillamine, pentaethylenehexamine (PEH) and ethylenediaminetetraacetic acid (EDTA) are excellent at trapping not only Cu^{2+} but also Ag, Pb, Co, Ni and Zn ions. These chelating agents are highly selective to Cu^{2+} and form the structure in which unpaired electron pairs of nitrogen held by amines selectively surround Cu^{2+} ion. Thus, the electrolytes and electrolysis method described above were named hereinafter as the CUSH method (for Cu ion Selective Holding) in the sense that Cu^{2+} can be selectively trapped.

Fig. 2-7 shows the Mn, S and Cu element maps of the MnS particle in the steel sheet electrolytically etched using the CUSH method under the No. 6, No. 7 and No. 8 electrolysis conditions in Table 2-2. Element maps of the Mn and S were shown like particles shape. The clear EDX signals could not be obtained for Cu whichever chelating agent was used. The above

results indicated that these Cu ion chelating agents are highly effective in preventing the formation of artificial sulfides during SPEED etching.
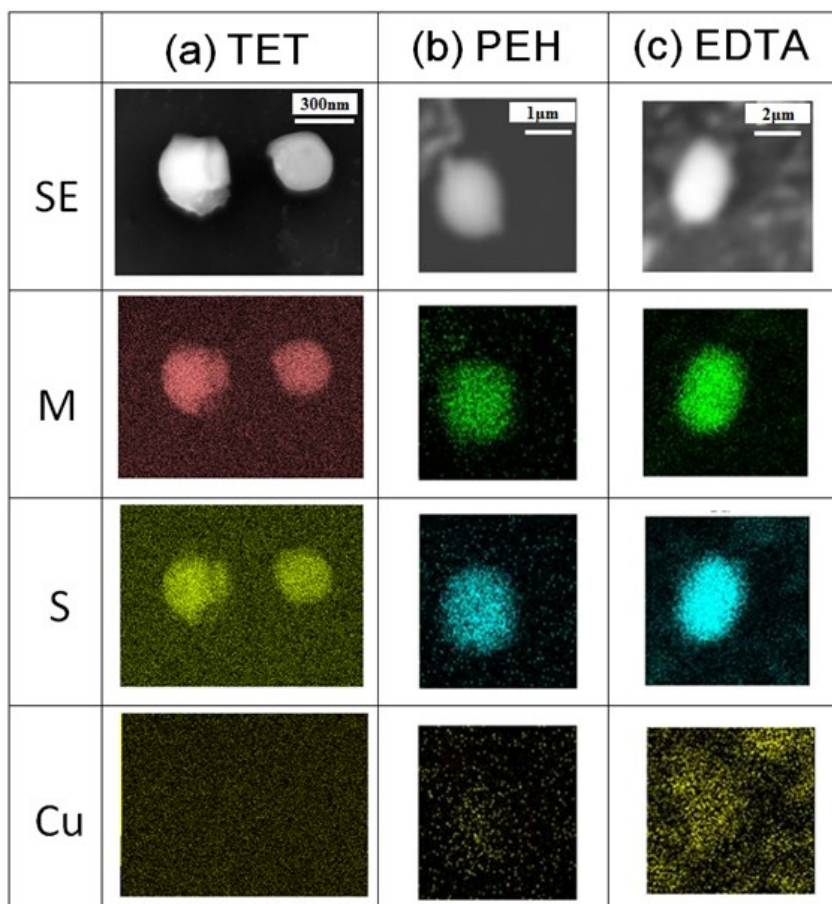
Fig. 2-7 SEM-EDX mapping of MnS particle after SPEED etching using 4%MS electrolyte with Cu chelating agent (a) TET, (b) PEH and (c) EDTA.

2.3.6 Comparison of content and morphology of Cu in electrolytic residues

SEM micrographs and EDX analysis values of electrolytic residues obtained under the No. 9 conventional electrolysis condition and the No. 10 developed electrolysis conditions in Table 2-2 were shown in Figs. 2-8(a) and (b), respectively. With the electrolytic residue obtained by the conventional method in Fig. 2-8(a), amorphous artificial sulfides were deposited in the MnS surface layer. With the electrolytic residue obtained by the CUSH method in Fig. 2-8(b), the surfaces of individual MnS particles are free from amorphous substances and smooth. According to the SEM-EDX element analysis results, the Cu content is high at about 37% in the residue (Fig. 2-8(a)) and is less than 5% in the residue (Fig. 2-8(b)) after the electrolysis by the CUSH method. These results confirmed that the formation of artificial sulfides was prevented during SPEED etching.

Chapter 2: Development of analysis method for sulfide in steel with chelating agent of copper
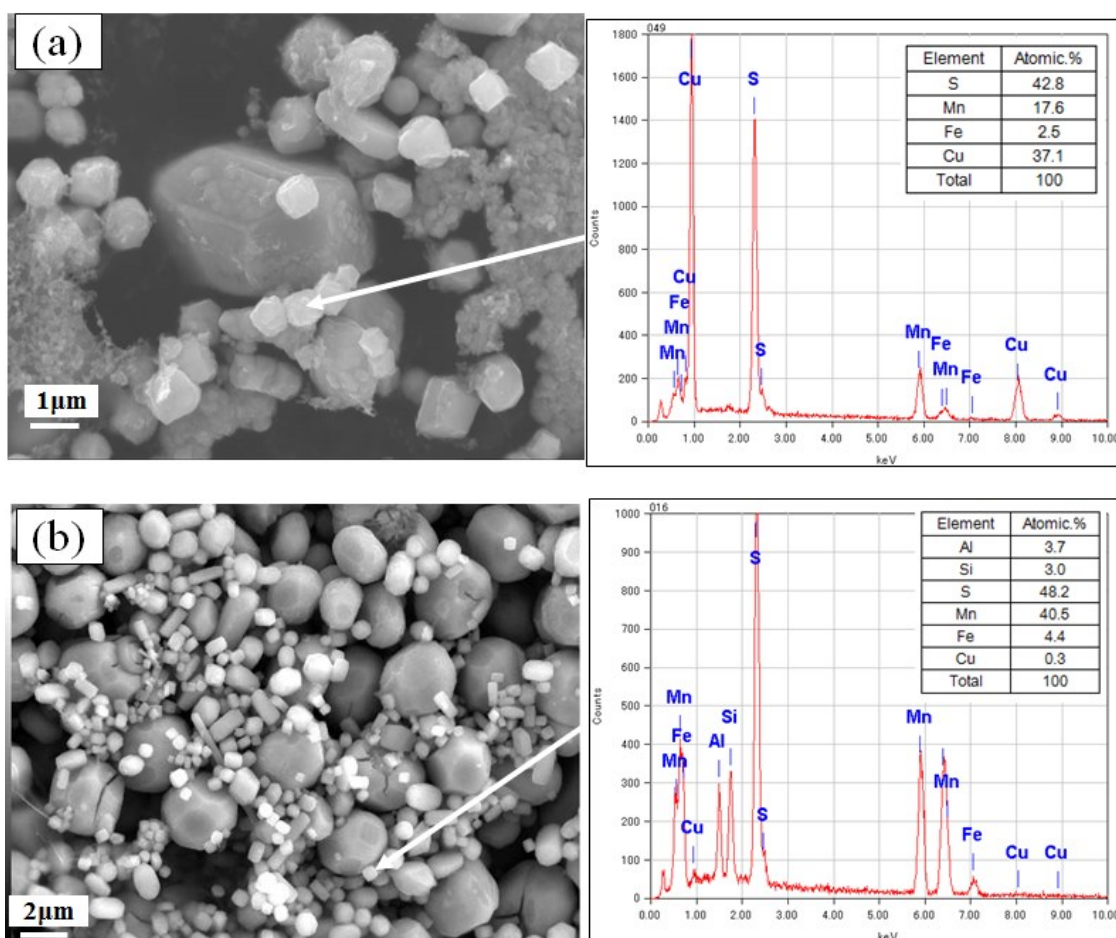
Fig. 2-8 Comparison of sulfides by SEM-EDX after SPEED etching with (a) 4% MS and (b) 4% MS+5% TET.

2.3.7 Study of optimum conditions of method for quantitatively analyzing electrolysis residue

With SPEED etching, the sample is electrolyzed only at a few tens of coulombs. We investigated the effect of the CUSH method when the residue after electrolysis of a sample weighing about 1 g was quantitatively analyzed. We found that the formation of artificial sulfides cannot be completely prevented when a large amount of steel sample is electrolyzed. We then studied the electrolysis conditions, electrolyte composition and steel composition and found the following tendencies occur when artificial sulfides form:

(1) Artificial sulfides increase with increasing electrolysis amount.
(2) Artificial sulfides increase with increasing carbon content of the steel sample.
(3) Artificial sulfides increase with decreasing Ar gas bubbling during electrolysis.

Chapter 2: Development of analysis method for sulfide in steel with chelating agent of copper

As our experimental results, when a Cu ion chelating agent was not contained in the electrolyte, the formation of artificial sulfides could not be prevented irrespective of the presence of Ar gas bubbling or stirring. When a Cu ion chelating agent was added to the electrolyte, the formation of artificial sulfides could be prevented only when the electrolyte was bubbled by Ar gas or stirred. Also, when Ar gas bubbling or stirring was weak, the formation of artificial sulfides varied, and the experimental reproducibility was low. To summarize the above results, the following estimation was considered about the formation of artificial sulfides in the CUSH electrolyte. The cementite increases in the sample surface with increasing electrolysis amount or carbon content. This makes it difficult for the Cu ion chelating agent to cover the MnS surface layer and causes Cu^{2+} dissolved from the steel matrix to react with MnS. Since this reaction proceeds very fast, it was estimated that the formation of artificial sulfides cannot be completely prevented, unless the Cu ion chelating agent is constantly supplied to the MnS surface layer by Ar gas bubbling.

Lastly, Fig. 2-9 showed the quantitative analysis values of the electrolysis residues obtained under optimized electrolysis conditions. Ar gas was supplied at 600 mL min^{-1} under the No. 10 electrolysis conditions in Table 2-2. The combined S content converted from the Mn and Cu contents of the residue obtained is shown in Figs. 2-9(a) and (b) when the steel sheet was electrolyzed with a conventional 4%MS electrolyte and shown in Figs. 2-9(c) and (d) when the steel sheet was electrolyzed with a developed CUSH electrolyte. With electrolysis using the conventional 4%MS electrolyte, about half of sulfides were formed as Cu_xS. With the developed CUSH electrolysis method, artificial Cu_xS was no longer detected. The repeatability of quantitative analysis of the combined S content in independent parallel tests was thus improved.

	(a) 4%MS (n=1)	(b) 4%MS (n=2)	(c) 4%MS+ 5%TET (n=1)	(d) 4%MS+ 5%TET (n=2)
□S as Cu$_2$S	77	80	0	0
■S as MnS	96	88	198	194
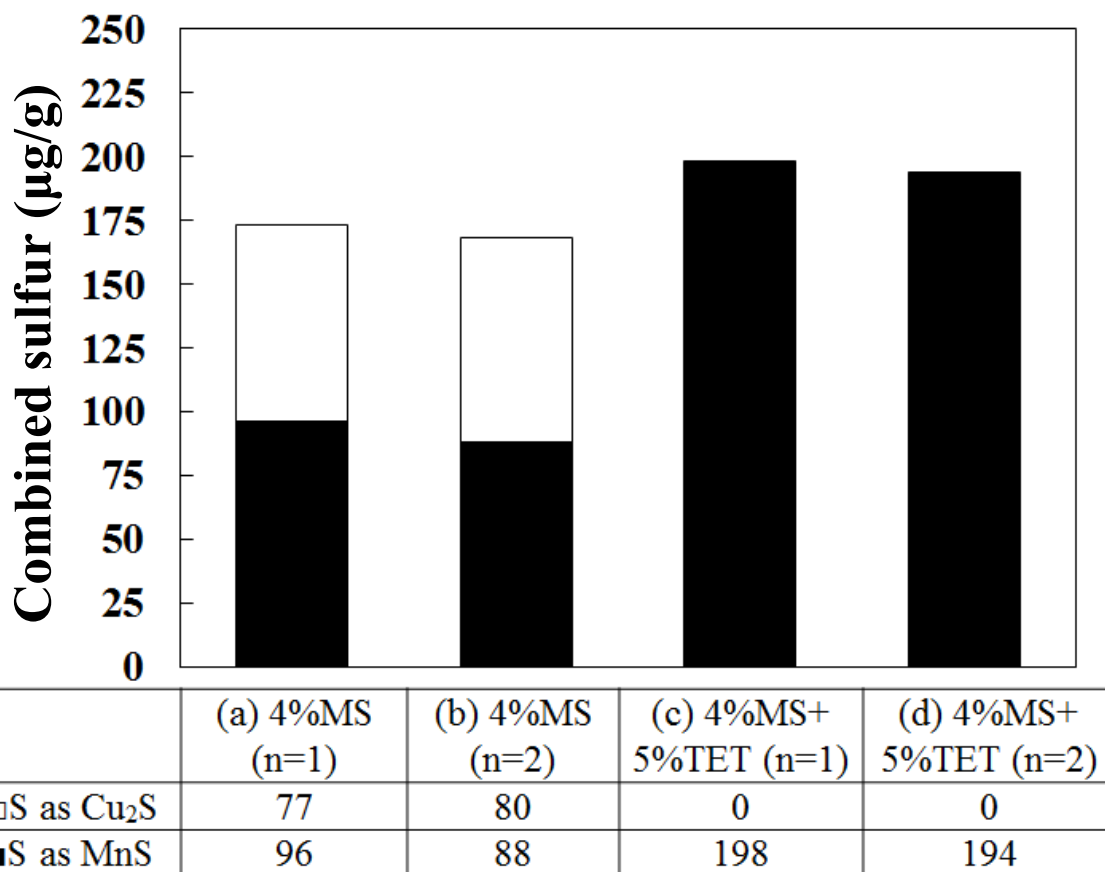
Fig. 2-9   With Ar gas bubbling, comparison of combined sulfur analysis using electrolyte as follows. (a) 4%MS (n=1), (b) 4%MS (n=2), (c) 4%MS+5%TET (n=1) and (d) 4%MS+5%TET (n=2). The white bar showed S as Cu$_2$S, the black bar showed S as MnS.

Chapter 2: Development of analysis method for sulfide in steel with chelating agent of copper

2.4 Conclusions

It was investigated that the mechanism whereby sulfides, considered originally not present in the steel matrix, are formed around the MnS when the steel sample is electrolytically etched by the SPEED method. It was also studied about electrolytes and electrolysis methods capable of preventing the formation of artificial sulfides. The following findings were observed:

(1) The greater the differences in the δpK_{sp} value of the sulfide solubility product, the more readily metal ions react with MnS.

(2) The addition of a Cu ion chelating agent is effective in preventing the artificial sulfide formation reaction.

(3) The combination use of bubbling is effective in increasing the effectiveness of Cu ion chelating agents.

Using the developed CUSH (Cu ion selective holding) electrolyte, we can observe fine particles *in-situ* in the steel matrix and can accurately and quantitatively analyze the particle size and composition of sulfides. With similar reactions expected, we consider that it is necessary to also study MnSe [16] whose crystal structure is the same as that of MnS and whose lattice constant is very close to that of MnS.

Chapter 2: Development of analysis method for sulfide in steel with chelating agent of copper

2.5   References

1. S. Hinotani, J. Endo, T. Takayama, N. Mizui, and Y. Inokuma: *ISIJ Int.*, **34**(1994), 17.

2. J.Tan and P.C.Pistorius: *Metall. Mater. Trans.B*, **44B**(2013), 483.

3. Z.Liu, Y.Kobayashi, K.Nagai, J.Yang, and M.Kuwabara: *ISIJ Int.*, **46**(2006), 744.

4. J.M.Dowling, J.M.Corbett, and H.W.Kerr: *Metall. Trans. A*, **17A**(1986), 1611.

5. Z.Zhang and R.A.Farrar: *Mater. Sci. Technol*, **12**(1996), 237.

6. I.Madariaga, J.L.Romero and I.Gutierrez: *Metall. Mater. Trans.A*, **29A**(1998), 1003.

7. G.Wranglen: *Corros. Sci.*, **14**(1974), 331.

8. J.G.Park, J.H.Park, Y.S.Lee, S.M.Jung, and D.J.Min: *ISIJ Int.*, **49**(2009), 171.

9. Y.Ishiguro, T.Murayama, K.Sato, and K.Kuroda: *Tetsu-to-Hagané*, **95**(2009), 8.

10. Y.Ishiguro, K.Sato, and T.Murayama: *Mater. Trans.*, **46**(2005), 769.

11. T.Sakai, T.Shimazu, K.Chikuma M.Tanino, and Matsuo: *Tetsu-to-Hagané*, **70**(1984), 2049.

12. K.Urata, Y.Kobayashi, R.Endo, M.Susa, and W.Y.Cha: *ISIJ Int.*, **55**(2015), 103.

13. C.D.J.Laughlin: "*Cu-S.Binary Alloy Phase Diagrams*", Second Edit., Ed.T.B.Massalski, ASM Int.Mat.Park, Ohio2 (1990), 1467.

14. Selected Solubility Products and Formation Constants at 25℃
    http://www.csudh.edu/oliver/chemdata/data-Ksp.htm

15. K. Ueno: "Chelate titration method", Minamiedo, Tokyo, (1956), 481.

16. T.Takamiya and O.Furukimi: *Tetsu-to-Hagané*, **100**(2014), 1413.

Chapter 2: Development of analysis method for sulfide in steel with chelating agent of copper

Chapter 3

Determination of size distribution of nanoparticles using asymmetric flow field-flow fractionation (AF4)

Chapter 3. Determination of size distribution of nanoparticles using asymmetric flow field-flow fractionation (AF4)

3.1 Introduction

Recently, nanoparticles, such as gold [1, 2], silver [3], platinum [4], carbon nanotubes, carbon black, and quantum dots [5], have been used in various industries, including cosmetics, electronics, and food. Nanoparticles are defined as materials with a diameter of 1–100 nm. As explained in the Chapter 1, steels contain various particles whose size ranges from nanometer to sub-micrometer for functionalizing various steel products [6]. The performance of particles in steels is dependent on their size and number density. In many cases, these particles have a wide size distribution; thus, determination of the average size and the size distribution of these particles has become considerably important. As mentioned in the Subsection 1.2.2, the electrolytic dissolution method is suggested as a method for extracting precipitates from steels. Additionally, in order to measure these extracted precipitates accurately, it is important to apply some kind of separation technique to analyze these particles in steels.

Several size-based separation techniques, such as asymmetric flow field-flow fractionation (AF4), size-exclusion chromatography, hydro dynamic chromatography, gel electrophoresis, capillary electrophoresis, and ultracentrifugation, have been reported in previous studies [7-11]. Many studies have suggested that AF4 has some advantages for analyzing metallic nanoparticles [12, 13]. AF4 has been employed for various samples, including certain matrices whose size ranges from nanometer to micrometer. If AF4 is combined with DLS and inductively coupled plasma-mass spectrometry (ICP-MS), the size distribution and elemental composition can be determined [14, 15]. Thus, AF4 analysis is expected to accurately measure particles that have a nonuniform and wide size distribution (e.g., precipitates and inclusions in steels). However, the application of AF4 analysis to complex materials such as steels has not been performed yet.

The major objective of this research is to develop the analytical method for the size distribution of precipitates in steels. Especially, Chapter 3, 4, and 5 focus on the improvement and modification of analytical method for the precipitates in steels using AF4-ICP-MS.

In this Chapter 3, prior to application to the evaluation of steels, the performance of size measurement by AF4 was investigated using gold nanoparticles (AuNPs). The average size and width of size distribution were verified by comparing the AF4 results with those of TEM and small-angle X-ray scattering (SAXS). Moreover, based on their results, a broadening coefficient for correcting the size distribution measured by AF4 was developed. Furthermore, the applicability of AF4 measurement with the broadening coefficient was investigated using

Chapter 3: Determination of size distribution of nanoparticles using asymmetric flow field-flow fractionation (AF4)

niobium carbide (NbC) in steels.

3.2 Experimental

3.2.1 Nanoparticles and reagents

All AuNPs and AgNPs were purchased from nanoComposix (San Diego, USA). All polystyrene size standard latex (PSL) particles STADEX were purchased from JSR life science (Tokyo, Japan). Tables 3-1 and 3-2 summarize the specifications of reference nanoparticles dispersed in water and those of the specimens.

Table 3-1. List of nanoparticles for reference.

Sample	Average diameter (nm)	Concentration (mg/L)	Dispersant	Shape
AuNP-2	2.1 ± 0.3	52.5	Glutathione	Sphere-like
AuNP-5	5.0 ± 0.6	1080	Citrate	Sphere-like
AuNP-7	7.5 ± 0.8	1070	Citrate	Sphere-like
AuNP-10	9.8 ± 0.8	1080	Citrate	Sphere-like
PSL-29	29 ± 1	5000	-	Sphere
PSL-48	48 ± 1	10000	-	Sphere
PSL-70	70 ± 1	10000	-	Sphere
PSL-100	100 ± 3	10000	-	Sphere

Table 3-2. (a) Sample specifications and (b) an average diameter of each specimen measured by different analyses.

(a)

Sample	Concentration (mg/L)	Dispersant	Shape
AuNP-5.5	1090	Lipoic acid	Sphere-like
AgNP-50s	20	Tannic acid	Sphere-like
AgNP-50p	20	PVA	Plate-like
NbC precipitates in steel (NCA5-3)	-	SDS	Plate-like
NbC precipitates in steel (NCA5-3)	-	SDS	Plate-like
NbC precipitates in steel (NCA5-1)	-	SDS	Plate-like

Chapter 3: Determination of size distribution of nanoparticles using asymmetric flow field-flow fractionation (AF4)

(b)

Sample	Average diameter (nm)			
	TEM	AF4 (raw data)	AF4 (corrected)	SAXS
AuNP-5.5	5.5 ± 0.5	5.6 ± 1.0	5.6 ± 0.5	5.0 ± 0.2
AgNP-50s	52.1 ± 7.1	54.1 ± 11.1	-	-
AgNP-50p	56.2 ± 14.6	59.6 ± 23.0	-	-
NbC precipitates in steel (NCA5-3)	2.4 ± 1.0 (FOV-1)	2.0 ± 0.4	2.0 ± 0.2	-
	2.1 ± 0.4 (FOV-2)			-
NbC precipitates in steel (NCA5-1)	-	2.1 ± 0.5	2.1 ± 0.2	-

AuNP-2, AuNP-5, AuNP-7, and AuNP-10 were used for calibrating the size measurement for AF4 analysis. AuNP-5.5 was prepared for comparisons between AF4 and SAXS measurements; it was placed onto a carbon-supporting grid and observed in a bright-field image using TEM. Two types of AgNPs (sphere-like and plate-like, called AgNP-50s and AgNP-50p, respectively) were used for the size distribution measurement using AF4 and TEM. Furthermore, to measure AgNPs, AuNPs and PSL particles were used for the size calibration using AF4.

All chemicals used for AF4 measurements were used as purchased without additional purification. Ultrapure water (>18 MΩ: Milli-Q water purification system type and Elix UV10, Millipore Corp., USA) was used for diluting samples and preparing AF4 carrier solutions. Sodium dodecyl sulfate (SDS, purity ≥ 99.0%) was obtained from FUJIFILM Wako Pure Chemical Corporation, Japan. Acetyl acetone (AA, special-grade, FUJIFILM Wako Pure Chemical Corporation), tetra methyl ammonium chloride (TMAC, purity ≥ 98.0%, Tokyo Chemical Industry Co., Ltd.), and methanol (special-grade, FUJIFILM Wako Pure Chemical Corporation) were used for extracting the precipitates from the steel sheets.

3.2.2   Sample preparation via selective potentio-static etching by the electrolytic dissolution method

NbC-precipitated ferritic steel, whose main chemical composition is 0.1% Nb and 0.01% C (mass %), was prepared from electrolytic iron by vacuum induction melting. Brock specimens ($30 \times 33 \times 45$ mm^3) for heat treatment were taken from an as-cast ingot. The heat treatment was conducted at 873 K for 1 h or 10 h after a solid solution treatment (1523 K, 24 h) and water quenching, which led to NbC precipitation. The holding time of the heat treatment was adjusted to change the size or number density of NbC. Additionally, the small specimens were cut into

dimensions of $25 \times 25 \times 2$ mm^3 for the following analysis.

For obtaining specimens of precipitates formed in the steel sheets, selective potentio-static etching by electrolytic dissolution (SPEED) was applied. A 10 (v/v) % AA, 1 (w/v) % TMAC, and 10 μg mL^{-1} SDS-MeOH solution was used. The electrolytic extraction was conducted in two steps with a constant current of 500 mA. The first step was the pretreatment of the electrolytic extraction for cleaning the surface. This step was operated for 15 min to dissolve the pollutants on the surface and the oxide layer on the sample. The second step was conducted for the dissolution of the sample from the surface layer. To separate the surface pollutants and the oxide layer, which were dissolved in the electrolytic solution used in the first step from the sample, the second step was conducted for 120 min after transferring the sample to another electrolytic solution having the same components. After 120 min of the electrolytic treatment, ~1.0 g of the steel anode sample dissolved in the solution and nanometer-sized carbides were dispersed in the electrolytic solution.

3.2.3   Instruments

3.2.3.1   AF4-ICP-MS

Fig. 3-1 displays the schematic of the Wyatt Eclipse AF4 system (Wyatt Technology Europe, Germany). This system is equipped with a high-performance liquid chromatography pump and an integrated degassing system with an auto sampler (Agilent Technologies 1260 Infinity series, Agilent Technologies, USA). Each nanoparticle was injected into this system, as shown in Fig. 3-1(a). Nanoparticles in the solution were diffused and moved with channel flow and eluted at a certain time according to their size in this system. The principle of nanoparticle size classification is shown in Figs. 3-1(b) and 3-1(c). The AF4 system employs two main steps for the separation of nanoparticles. First, the injected nanoparticles were focused at the focusing zone by the flow from both sides of the AF4 separation channel. Nanoparticles in solution were simultaneously separated by the difference of their own diffusion constant in the focus step. With a decrease in the particle size, nanoparticles floated to the upper side in the AF4 separation channel. Next, the flow was switched to only one direction in the elution step. Smaller nanoparticles were carried from the focusing zone of this channel by the faster flow rate near the center in a laminar flow. Contrastingly, larger nanoparticles moved slowly and were carried by the slower flow. A regenerated cellulose (RC) ultrafiltration membrane (Microdyn-Nadir, Germany) with a molecular weight cut-off of 5 kDa (RC 5 kDa) or 30 kDa (RC 30 kDa) was used as an accumulation wall for the AF4 separation channel. During this time, 10 μg mL^{-1} SDS solutions in ultrapure water were used as AF4 carrier solutions. The electric repulsive force to prevent nanoparticle adhesion on the membrane was generated by the surface charge on

Chapter 3: Determination of size distribution of nanoparticles using asymmetric flow field-flow fractionation (AF4)

particles and the membrane; this force was characterized by the zeta potential between the nanoparticles and the membrane. A separation device equipped with a 275-mm-long channel and a 490-µm-thick or 350-µm-thick asymmetric diamond-shaped channel spacer was applied.

To detect the separated nanoparticles, the AF4 separation channel was connected to a variable-wavelength ultraviolet (UV)–visible detector (Agilent Technologies 1260 Infinity series) through a polyether ether ketone (PEEK) tube. The detection wavelength of UV was set to 520 or 254 nm. The online elemental information of the nanoparticles separated by AF4 was obtained using ICP-quadrupole MS (Agilent8800, Agilent Technologies, USA). This instrument was directly connected to the PEEK tube at the outlet from the UV detector of the AF4 system.
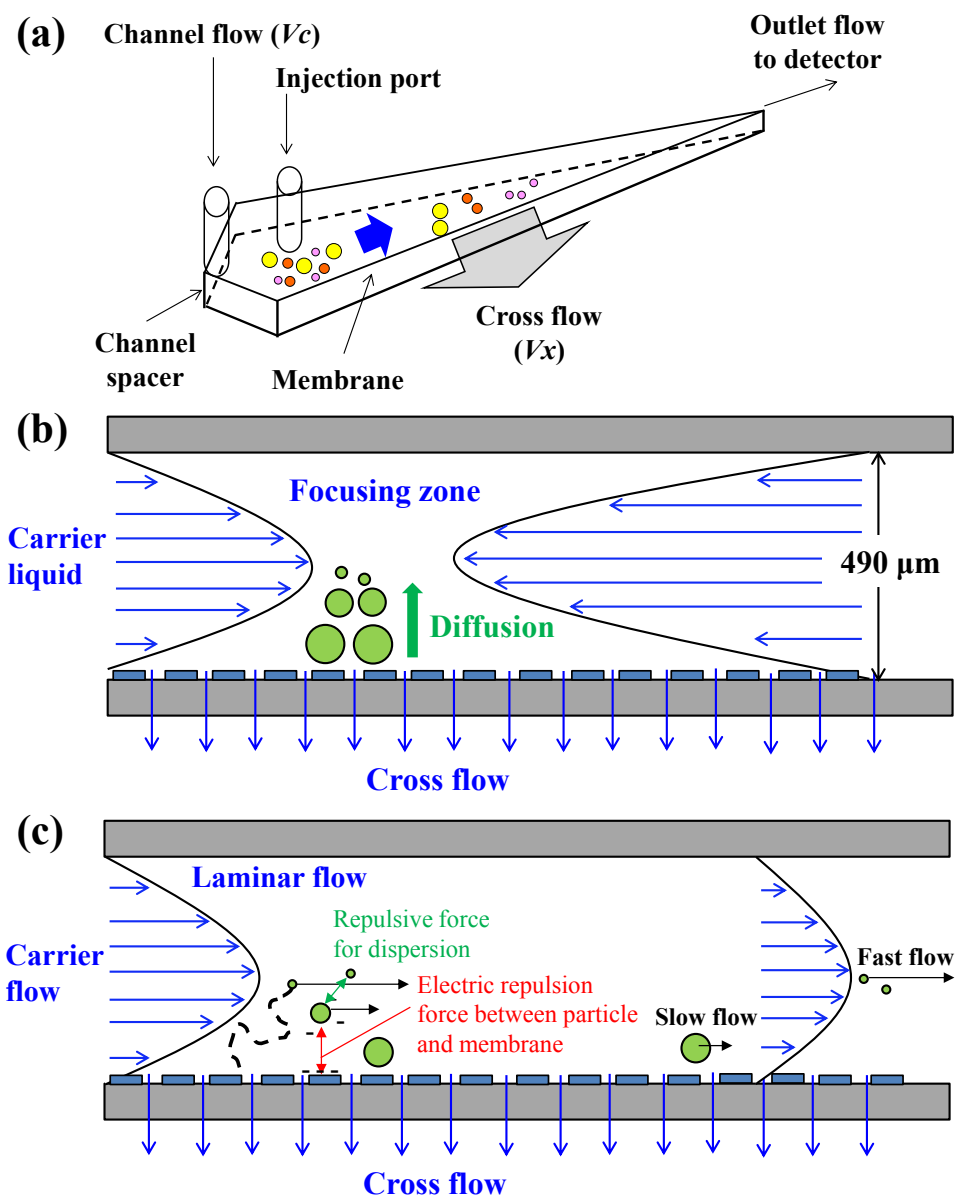
Fig. 3-1 Schematic of the AF4 instrument. (a) whole diagram and (b) cross-sectional diagram of the focus step and (c) the elution step.

Chapter 3: Determination of size distribution of nanoparticles using asymmetric flow field-flow fractionation (AF4)

The sample introduction system comprised a self-aspirating nebulizer (MicroMist nebulizer). Table 3-3 summarizes the operating conditions of ICP-MS. Prior to the AF4 measurement, the membrane was conditioned with an AF4 carrier solution of SDS for at least 30 min. Each AuNP and AgNP dispersed solution was diluted to 25 μg mL^{-1} using ultrapure water. The precipitates dispersed in the SPEED solution were then applied without dilution. Then, these samples were injected in the AF4 separation channel using the autosampler, and then analyzed. Table 3-4 summarizes the AF4 separation conditions.

Table 3-3. Operating conditions of the inductively coupled plasma mass spectrometry (ICP-MS) when connecting to AF4.

Agilent8800 ICP-MS	
RF power (W)	1550
Nebulizer flow (L/min)	1.05
Cooling gas (L/min)	15
Auxiliary gas (L/min)	0.90
Sampling depth (mm)	8.0
Element (m/z)	Au (197)
Duration time (s)	0.10
Spray chamber temperature (K)	275.15

Table 3-4. Separation condition in AF4.

		For AuNPs and NbC precipitates	For AgNPs
Channel parameters	**Membrane nature**	**Regenerated Cellulose (RC)**	**Regenerated Cellulose (RC)**
	Membrane cut-off	**30 kDa**	**5 kDa**
	Spacer	**490 um**	**350 um**
	Elution solvent	**0.035 mmol L^{-1} SDS**	**1.73 mmol L^{-1} SDS**
Fractionation time	**Elution time**	**1 minute**	**1 minute**
	Focusing time	**1 minute**	**1 minute**
	Focus +Injection time	**2 minutes**	**2 minutes**
	Focusing time	**1 minute**	**3 minutes**
	Elution time	**45 minutes**	**35 minutes**
Fractionation step, flow, and volume	**Injection volume**	**20-100 μL (optimal)**	**100 μL**
	Injection flow	**0.2 mL min^{-1}**	**0.2 mL min^{-1}**
	Channel flow(Vout)	**1.0 mL min^{-1}**	**1.0 mL min^{-1}**
	Cross flow(Vc)	**2.0→ 0.1 mL min^{-1} (linear gradient)**	**3.0→ 0 mL min^{-1} (linear gradient)**
	Focus flow	**3.0 mL min^{-1}**	**3.0 mL min^{-1}**
Detector	**UV absorbance**	**520 nm**	**254 nm**

Chapter 3: Determination of size distribution of nanoparticles using asymmetric flow field-flow fractionation (AF4)

3.2.3.2　TEM

For TEM observation, AuNPs dispersed in the solution were placed on the carbon-supporting grid and dried under reduced pressure. These samples were then observed using a field-emission transmission electron microscope (Tecnai F20, FEI Inc., USA) at an acceleration voltage of 80 kV. Bright-field images were obtained for the AuNPs, and processed using the Digital Micrograph software package (Gatan Inc., USA); the maximum diameter of each of the 500 particles was manually measured. Furthermore, the precipitates extracted in the above SPEED solution were prepared in the same manner as that for the TEM observation of AuNPs.

3.2.3.3　SAXS

SAXS measurements were performed at the beam line BL-10C, [16] located at the Photon Factory (PF), the High Energy Accelerator Research Organization (KEK) in Tsukuba, Japan. The energy of an incident X-ray was set to 12.4 keV. A two-dimensional (2D) hybrid pixel array detector, PLATUS3 2M (DECTRIS Ltd., Baden, Switzerland), was set at 1 m from the sample. In the SAXS measurement, to measure the AuNPs dispersed in the solution, a custom-made sample cell was used for solution experiments. All SAXS measurements were performed as follows. The X-ray scattering data from AuNPs were obtained by measuring 10 frames with an exposure time of 10 s, and combined to yield a dataset with low noise. The obtained 2D data were converted to one-dimensional data [data obtained via circular ring average using Fit2d (developed by ESRF)]. Silver behenate was used for calibrating the camera distance. Furthermore, the scattering vector is defined as

$$q = \frac{4\pi}{\lambda} \sin\frac{\theta}{2} \qquad \text{(Eq. 3-1)}$$

where λ is the wavelength (nm) and θ is the scattering angle. Note that the scattering intensities were corrected for background scattering.

3.3　Results and Discussion

3.3.1　TEM observation of nanoparticles

First, AuNP-5.5, AgNPs, and NbC precipitates were observed using TEM. AuNP-5.5 and AgNPs were dispersed not as aggregates but as single particles with a primary diameter. Fig. 3-2 shows one of the TEM images and the size distribution of AuNP-5.5 and AgNPs; however, as shown in Fig. 3-3, certain NbC precipitates were aggregated in several fields of view (FOVs).

Chapter 3: Determination of size distribution of nanoparticles using asymmetric flow field-flow fractionation (AF4)

The shape of AuNP-5.5 and AgNP-50s was almost spherical, but a part of the particles was not spherical; however, AgNP-50p and NbC precipitates had a plate-like shape. The diameter and thickness of AgNP-50p were approximately 56 and 14 nm, respectively. Furthermore, NbC precipitates had diameter and thickness of several nanometers. These nanoparticles were measured by AF4 and SAXS in subsequent experiments.
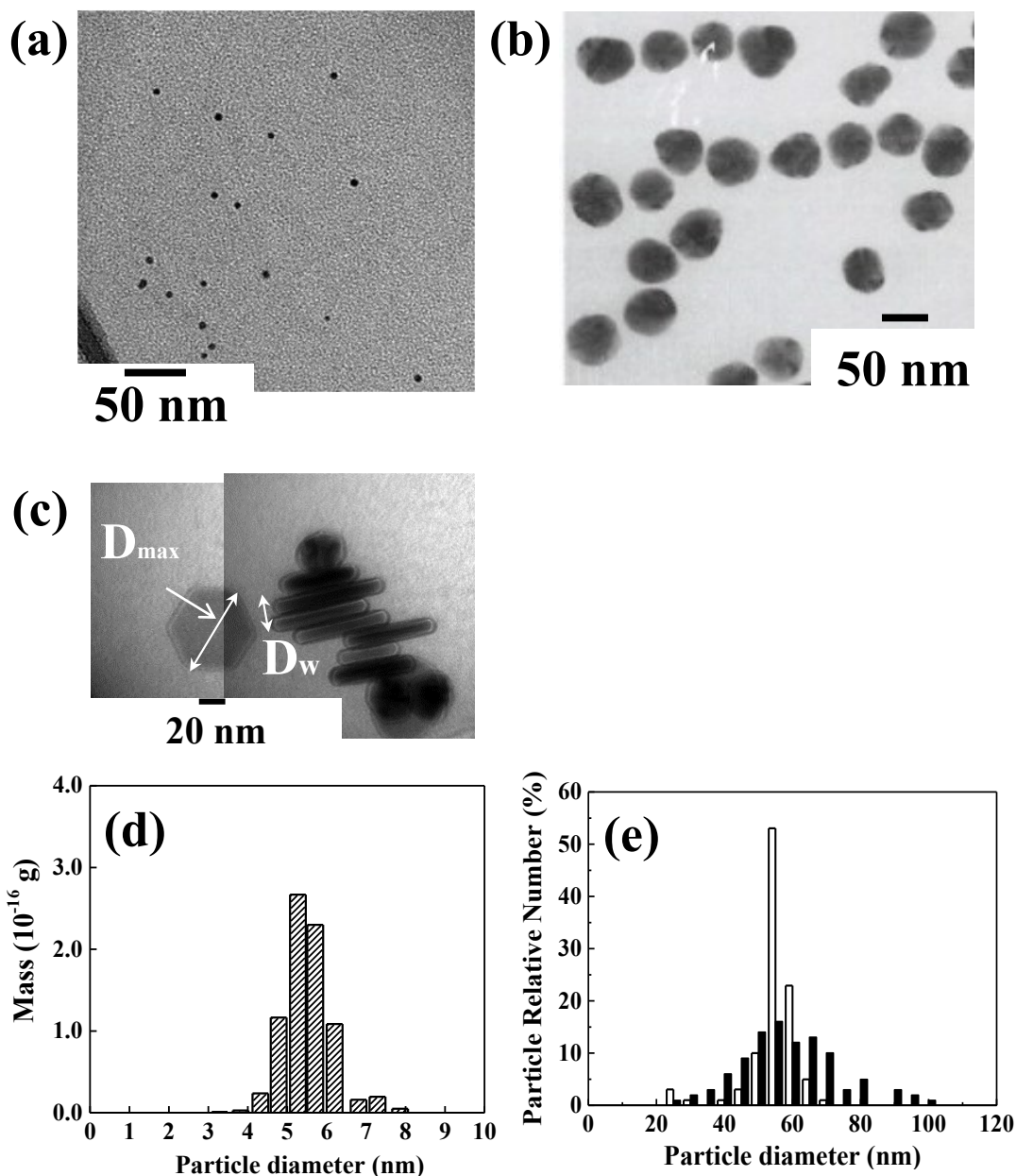
Fig. 3-2 TEM bright-field images of (a) AuNP-5.5, (b) AgNP-50s, and (c) AgNP-50p on a carbon-supporting grid. The size distribution of (d) AuNP-5.5 and (e) two types of AgNPs by TEM. The white bar shows AgNP-50s and the black bar shows AgNP-50p. The diameter of AgNP-50p was measured as a maximum of diameter (D_{max}). The thickness of AgNP-50s (D_w) was ignored here.
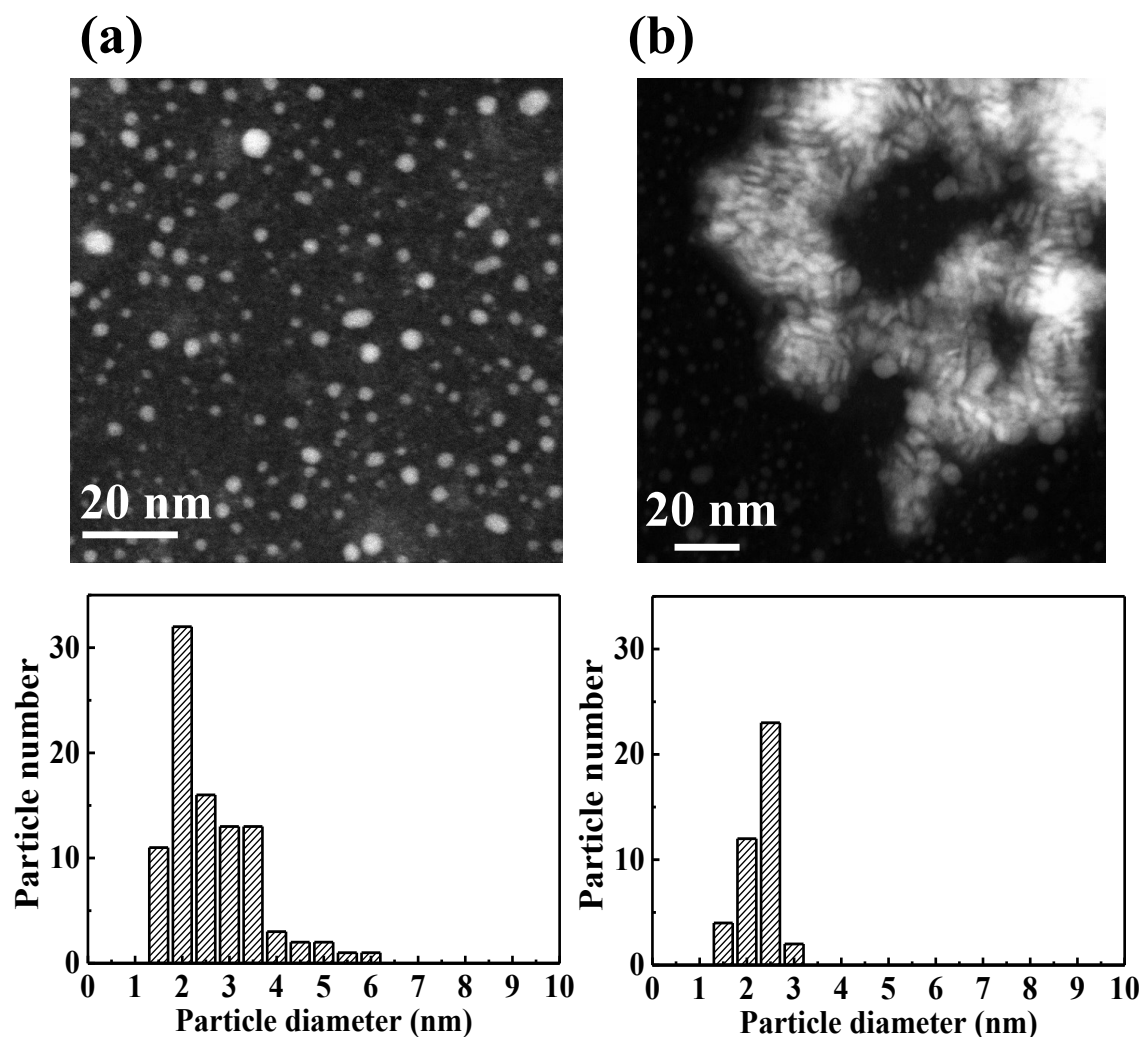
Fig. 3-3 HAADF-STEM image of electrolytically extracted NbC from the steel sheet, NCA5-3, at two FOVs and size distributions at each FOV: (a) FOV No.1 and (b) FOV No.2.

3.3.2 Comparison of AF4 results with TEM and SAXS results in AuNP analysis: average diameter and width of distribution

To confirm the performance of the size measurement method for AF4, AuNP-5.5 (primary diameter 5.5 ± 0.5 nm) was measured via AF4, TEM, and SAXS with synchrotron radiation. For AF4, the measurement was performed under optimized conditions, and the size distribution was estimated using the calibration curve obtained based on other AuNP sizes. The results were fitted via a Gaussian distribution, and the average size of AuNP-5.5 and the full width at half maxima (FWHM) of the size distribution were calculated. Furthermore, TEM observations were repeated twice to confirm the uncertainty of the size measurement using TEM. Moreover, for the SAXS measurement, the AuNP-5.5 dispersed solution was placed in a custom-made sample

cell. Fig. 3-4 shows the SAXS profile of the AuNP-5.5 dispersed solution. Two scattering peaks, indicated by arrows, were clearly observed. Generally, the scattering maxima from a form factor are clearly observed if the scatterers in a sample have a uniform size distribution. Thus, AuNPs were considered to have mostly uniform size. From the TEM observation, the shape of AuNP-5.5 was presumed to be spherical and the fitting was performed via a theoretical scattering curve. The form factor $P(q)$ of the spherical particle was expressed in Eq. 3-2. The size distribution of $P(q)$ was modeled using the Gaussian distribution. The solid lines in Fig. 3-4 show the calculated SAXS profiles. The calculated SAXS curves were in excellent agreement with the experimental curve.

$$P(q) = (3C \frac{\sin(qR) - qR\cos(qR)}{(qR)^3})^2 \qquad \text{(Eq. 3-2)}$$

where C is a constant and R is the radius of the sphere.
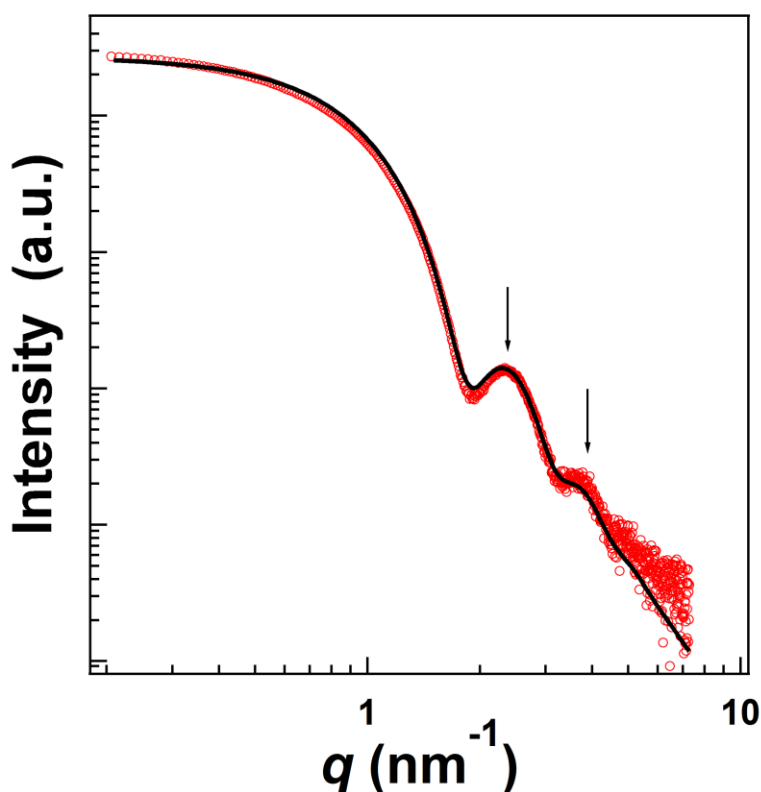
Fig. 3-4 SAXS profile of 5.5 ± 0.5 nm AuNPs. Solid line represents the model fits obtained using Eq. 3-2.

Fig. 3-5 (a) shows the results of AF4 analysis, SAXS fitting, and TEM observation. Table 3-2 summarizes each average size of AuNP-5.5 and the FWHM of the size distribution.
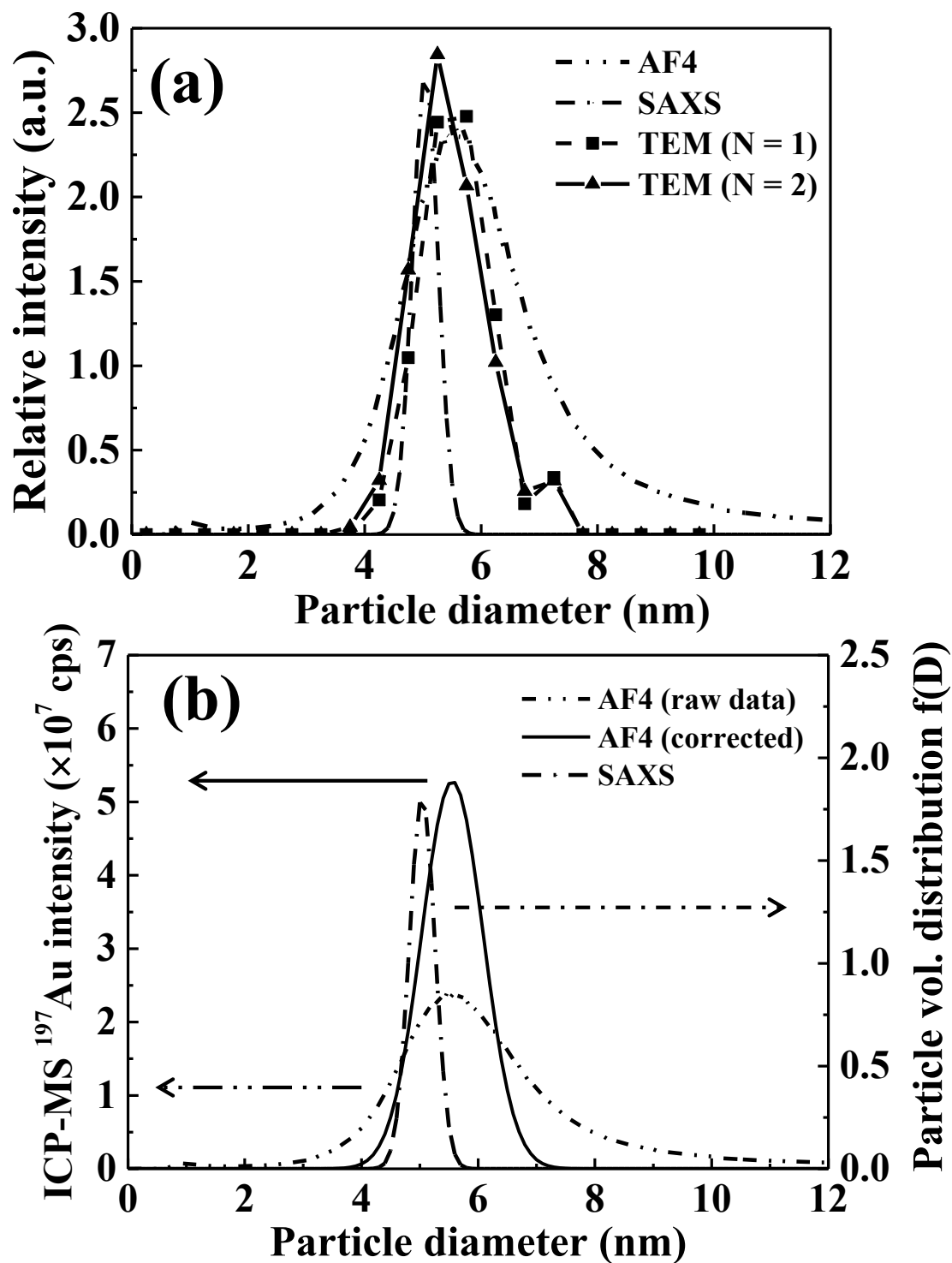
Fig. 3-5 (a) Size distributions of AuNP-5.5 measured using AF4, TEM, and SAXS. The AF4 was operated under optimized conditions. TEM observations were repeated twice. (b) Comparison of size distributions of AuNP-5.5 among AF4, AF4 with broadening coefficient, and SAXS.

Chapter 3: Determination of size distribution of nanoparticles using asymmetric flow field-flow fractionation (AF4)

As expected, the average size measured using AF4 was consistent with the TEM results, because AF4 measurement was conducted using the size calibration curve with TEM results. However, the two average diameters measured by AF4 and TEM were slightly larger than that of SAXS. This difference was caused by the presumption regarding the particle shape. For SAXS analysis, it was presumed that AuNPs had completely spherical shapes; however, the AuNPs were not completely spherical.

Furthermore, the FWHM of the size distribution measured by AF4 was not consistent with those measured by TEM and SAXS. The FWHM of the AF4 result was almost five times larger than that obtained using SAXS. Moreover, in the case of TEM, the FWHM of the AF4 result became approximately twice as large as that of TEM. These differences were attributed to the following two reasons. First, these methods for particle characterization adopted different principles for measurement. AF4 was used to measure particle mobility, TEM was used to measure electron diffraction, and SAXS was used to measure the difference in electron density in terms of crystallography. The AF4 result reflected the outer shape of the particles, the TEM result indicated the contrast of electron diffraction derived from elemental components and crystalline nature, and the SAXS result indicated the electron density difference between the particles and surrounding matrices. The difference in assumption regarding particle shape was reflected in these results.

Second, considerable attention should be paid to the measurement method in AF4 analysis, because the FWHM of size distribution measured by AF4 was the largest due to the diffusion of particles in the AF4 separation channel. Because the AF4 measurement was conducted under the condition that particles were flowing, it was unavoidable that any particle would diffuse in the AF4 separation channel. This phenomenon led to the broadening of the size distribution and a lack of size resolution; thus, the measurement method for particle size distribution using AF4 should be improved.

3.3.3   Correction method for size distribution in AF4 analysis

As discussed in Chapter 3.3.2, as FWHM largely depends on the principle, the measured values were attempted to be corrected for a realistic application. The correction method of the size distribution measurement for AF4 analysis was as follows. Each FWHM ratio of AF4 to TEM or SAXS for AuNP-5.5 was calculated from the results shown in Table 3-2; consequently, the FWHM ratio of AF4/SAXS and AF4/TEM was 4.64 and 1.94, respectively. The FWHM ratio of AF4/TEM should be adopted for the correction because the sizes estimated by TEM were used for the size calibration of AF4. The value was defined as a broadening coefficient of AF4 analysis. Additionally, same as mentioned above, the broadening coefficient for other

nanoparticles was calculated, as shown in Table 3-5.

Table 3-5. The broadening coefficients in AF4 analysis

Samples	Average size /nm (TEM)	Shape	Component of materials	Density /g·cm⁻³	Broadening coefficient	FWHM (AF4)	FWHM (TEM)
AuNP-2	2.1 ± 0.3	sphere-like	Gold	19.32	2.21	1.66	0.75
AuNP-5	5.0 ± 0.6	sphere-like	Gold	19.32	2.05	2.56	1.25
AuNP-5.5	5.5 ± 0.5	sphere-like	Gold	19.32	1.94	2.40	1.24
AuNP-7	7.5 ± 0.8	sphere-like	Gold	19.32	2.29	3.09	1.35
AuNP-10	9.8 ± 0.8	sphere-like	Gold	19.32	1.94	3.47	1.79
AgNP-50s	52.1 ± 7.1	sphere-like	Silver	10.49	3.01	26.09	8.66
AgNP-50p	56.2 ± 14.6	plate-like	Silver	10.49	1.64	54.05	32.90

Here, two types of AgNPs were measured by other AF4 operating conditions, because AgNPs had about 10-times larger diameter as compared to the above AuNPs. Prior to the AF4 measurement of AgNPs, the size calibration was conducted by several AuNPs and PSL particles, as shown in Fig. 3-6.
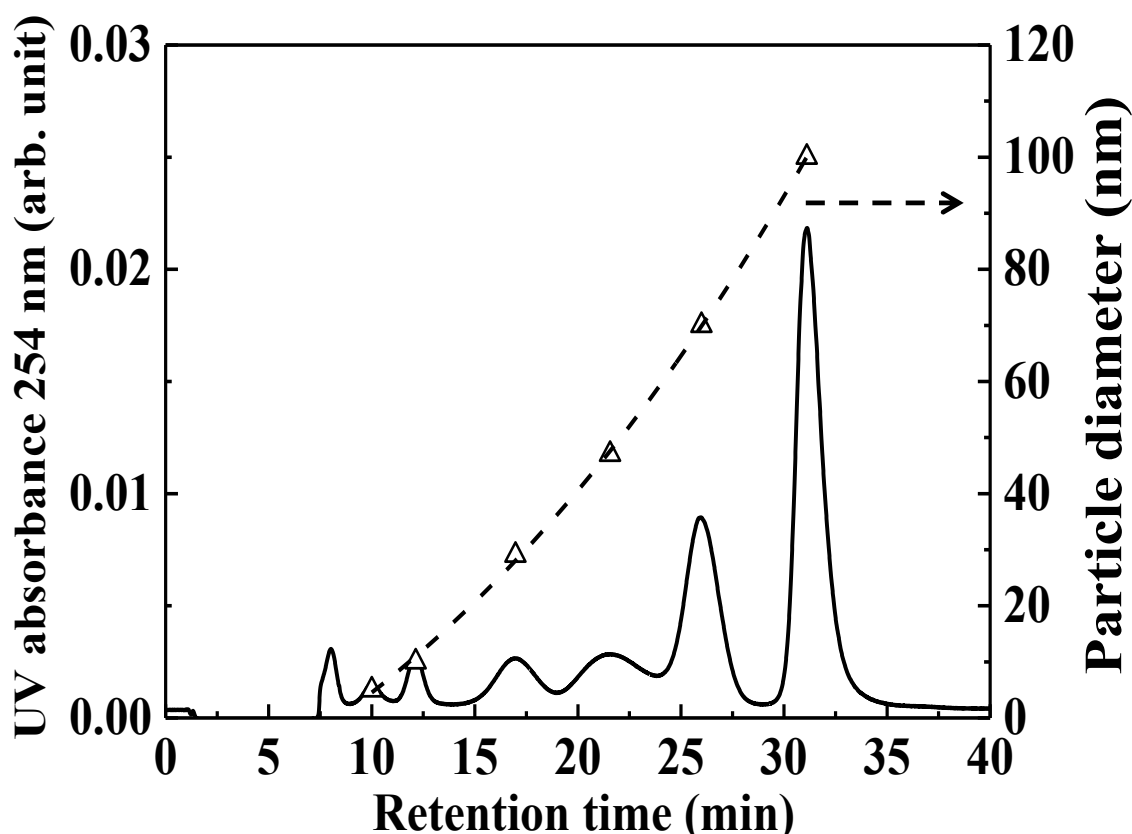
Fig. 3-6 Separation results of AuNPs and PSL mixtures by AF4. Bottom and right axes show the size calibration curve.

The size distribution of two AgNPs measured by AF4 and TEM is shown in Fig. 3-7. It was revealed that the broadening phenomenon of particles in the AF4 separation channel can influence any AF4 chromatogram regardless of their particle size.
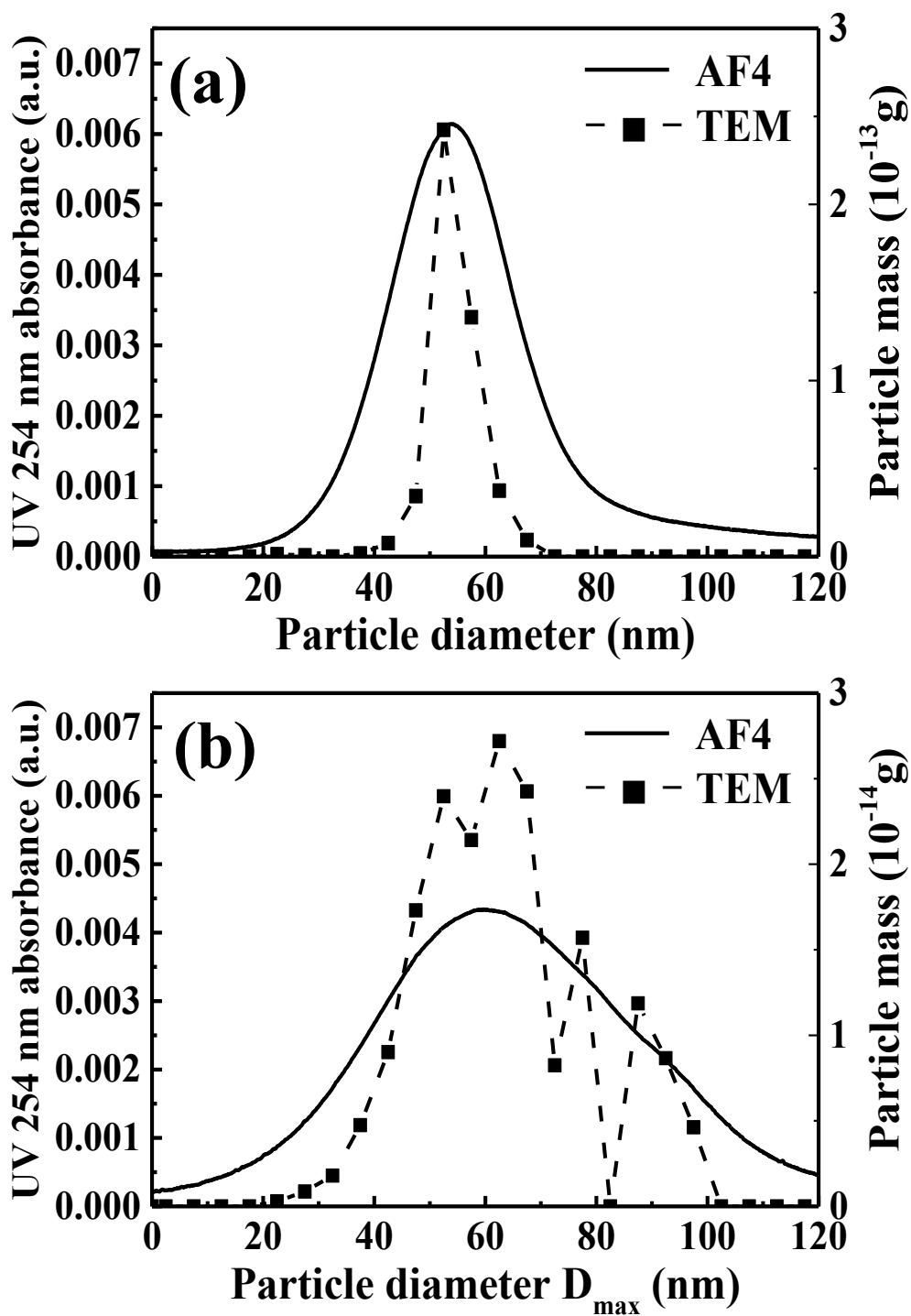
Fig. 3-7 Size distributions of AgNPs measured using TEM and AF4. (a) AgNP-50s and (b) AgNP-50p.

Chapter 3: Determination of size distribution of nanoparticles using asymmetric flow field-flow fractionation (AF4)

The findings for the broadening coefficient are summarized as follows:

(i) The broadening coefficients calculated from the measurement results of the above AuNPs, largely depend on the shape and type of particles. The broadening coefficient determined for sphere-like particles was in a range of 1.94-2.29.

(ii) The effects of particle shape were considered for two types of AgNPs, because the direct comparison among different types of particles was not straightforward. The broadening coefficient for plate-like particles apparently became smaller than that for sphere-like particles. This was attributed to the fact that the flow in AF4 became more dominant than the Brownian diffusion of plate-like particles themselves; consequently, the Brownian motion of plate-like particles was suppressed for the horizontal direction.

Subsequently, the above broadening coefficient was used for calculating the standard deviation of AuNP-5.5. The average size measured by AF4, the total area of peaks detected by AF4, and the estimated standard deviation were utilized for correcting the size distribution measured by AF4. The Gaussian distribution was assumed from the TEM and SAXS results. Fig. 3-5 (b) shows the AF4 measurement results of AuNP-5.5 corrected by the broadening coefficient. It was revealed that the AF4 result calibrated by TEM became closer to SAXS result.

3.3.4   Application of size distribution measurement method by AF4 with broadening coefficient to NbC precipitates in steels

To investigate the applicability of the correction method of FWHM in AF4 analysis, NbC precipitates extracted from the steel samples were measured by AF4. Consequently, the correction method of FWHM was found to be more effective with a lesser measurement error for nanometer-sized precipitates in steels.

NbC precipitates were measured by AF4 under the operating conditions same as those for AuNPs. Fig. 3-8 shows the size distribution of NbC precipitates measured by AF4. The heat treatment for steels was conducted to increase the size of NbC precipitates. Additionally, it was observed by TEM that these NbC precipitates were not uniformly dispersed in the steel sheets. The size distribution of NbC precipitates was not coincident among several FOVs; however, AF4 showed average information about the size distribution and this result was almost close to that of TEM. Furthermore, this result indicated that not size but only the number density of fine NbC increased by about 1.5 times with the holding time of heat treatment, against our predictions. In this study, a quantitative analysis was not conducted due to the necessity of more

improvement in the quantitativeness for AF4-ICP-MS. Because the peak areas of AF4-ICP-MS indicated the relative amounts of NbC, the difference in the number density of NbC was calculated through a comparison of peak areas between NCA5-1 and NCA5-3 steels: 1.0 and 1.5 respectively. In this manner, AF4-ICP-MS was found to be effective for semi-quantitatively measuring precipitates in steels.
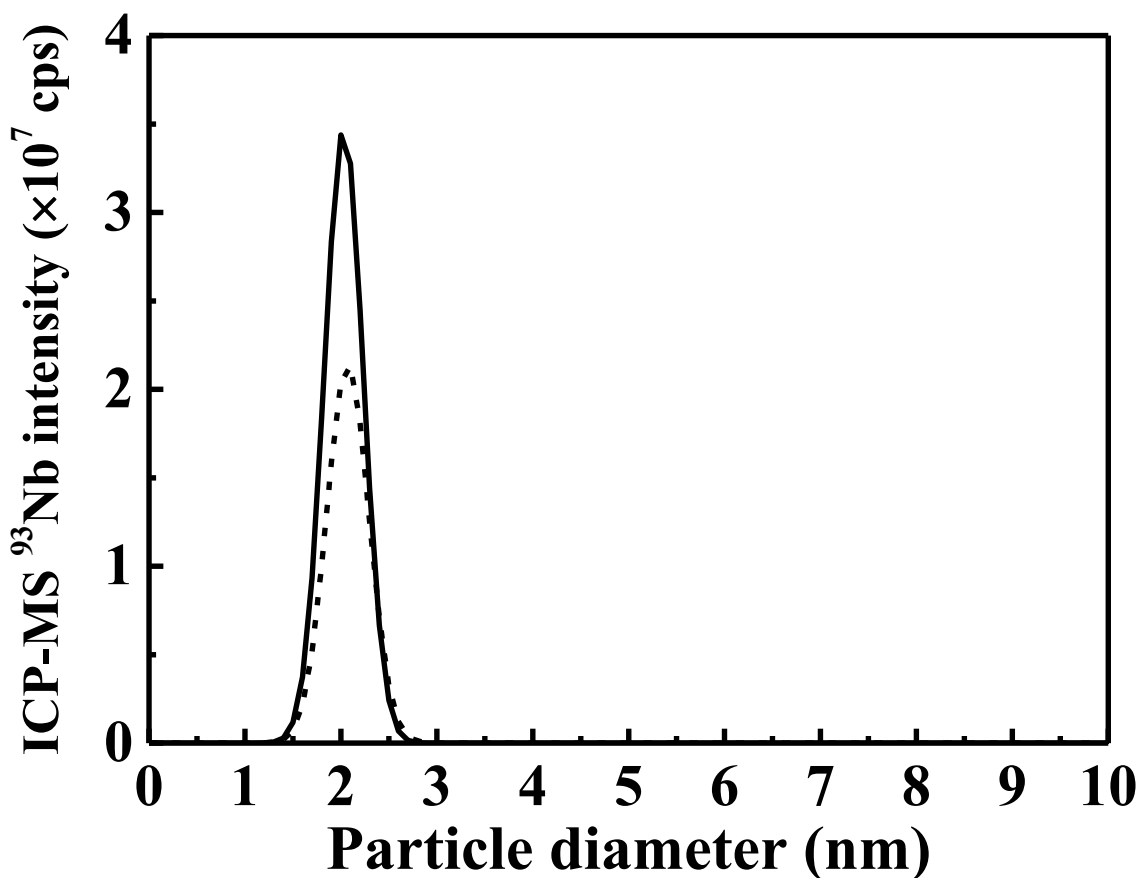
Fig. 3-8 Results of AF4-ICP-MS measurement for NbC in steels. The heat treatment was processed at 873 K to NCA5-1 (dotted line) for 1 h and to NCA5-3 (straight line) for 10 h.

In conclusion, the FWHM correction method in AF4 measurement was found to be useful for evaluating various nanoparticles. In the future, more detailed discussion would be conducted by considering the effect of particle shape on the FWHM of size distribution and improving the quantitative analysis method in AF4-ICP-MS.

Chapter 3: Determination of size distribution of nanoparticles using asymmetric flow field-flow fractionation (AF4)

3.4 Conclusions

The measurement method of the size distribution by AF4 with TEM was investigated using various nanoparticles. The findings in this study are summarized as follows.

(1) The average size measured by AF4 was almost same as those measured by TEM and SAXS. However, special attention should be paid to the presumption of particle shape, because the SAXS measurement was easily affected by the particle shape.

(2) For AF4 analysis, a peak-broadening phenomenon occurred because of the diffusion of particles in the AF4 separation channel.

(3) An FWHM correction method of size distribution in AF4 analysis was developed using a broadening coefficient, defined as the FWHM ratio of AF4/TEM.

(4) The broadening coefficient for sphere-like particles was determined as ca. 2.0; on the other hand, the broadening coefficient for plate-like particles (ca. 1.6) apparently became smaller than that for sphere-like particles due to the suppression of the Brownian motion.

When the broadening coefficient was applied, it was effective for the size evaluation of various nanoparticles. Therefore, the applicability of the FWHM correction method in the AF4 analysis was confirmed.

Chapter 3: Determination of size distribution of nanoparticles using asymmetric flow field-flow fractionation (AF4)

3.5 References

1. K. S. Siddiqi and A. Husen: *J. Trace Elem. Med. Biol.*, **40**(2017), 10.

2. D. Peng, B. Hu, M. Kang, M. Wang, L. He, Z. Zhang and S. Fang: *Appl. Surf. Sci.*, **390**(2016), 422.

3. H. Chen, F. Gao, R. He and D. Cui: *J. Colloid Interface Sci.*, **315**(2007), 158.

4. Y. Li and F. Zaera: *J. Catal.*, **326**(2015), 116.

5. T. Jamieson, R. Bakhshi, D. Petrova, R. Pocock, M. Imani and A. M. Seifalian: *Biomaterials*, **28**(2007), 4717.

6. T. Kataoka, Y. Arita, F. Takahashi, H. Fujimura, Y. Kurosaki, M. Sugiyama and I. Ohnuma: *ISIJ Int.*, **56**(2016), 2062.

7. G. T. Wei, F. K. Liu and C. R. Chris Wang: *Anal. Chem.*, **71**(1999), 2085.

8. K. M. Krueger, A. M. Al-Somali, J. C. Falkner and V. L. Colvin: *Anal. Chem.*, **77**(2005), 3511.

9. E. P. Gray, T. A. Bruton, C. P. Higgins, R. U. Halden, P. Westerhoff and J. F. Ranville: *J. Anal. At. Spectrom.*, **27**(2012), 1532.

10. F. K. Liu, F. H. Ko, P. W. Huang, C. H. Wu and T. C. Chu: *J. Chromatogr. A*, **1062**(2005), 139.

11. X. Xu, K. K. Caswell, E. Tucker, S. Kabisatpathy, K. L. Brodhacker and W. A. Scrivens: *J. Chromatogr. A*, **1167**(2007), 35.

12. J.C. Giddings, *Science*, **260**(1993), 1456.

13. J.C. Giddings, F.J. Yang and M.N. Myers: *Science*, **193**(1976), 1244.

14. B. Schmidt, K. Loeschner, N. Hadrup, A. Mortensen, J. J. Sloth, C. B. Koch and E. H. Larsen: *Anal. Chem.*, **83**(2011), 2461.

15. H. Hagendorfer, R. Kaegi, J. Traber, S. F.L. Mertens, R. Scherrers, C. Ludwig and A. Ulrich: *Anal. Chim. Acta*, **706**(2011), 367.

16. N. Igarashi, Y. Watanabe, Y. Shinohara, Y. Inoko, G. Matsuba, H. Okuda, T. Mori and K. Ito: *J. Phys. Conf. Ser.*, **272**(2011), 012026.

Chapter 3: Determination of size distribution of nanoparticles using asymmetric flow field-flow fractionation (AF4)

Chapter 4: Improvement of sample introduction efficiency for ICP-MS using the mistral desolvating sample introduction method

- 85 -

Chapter 4

Improvement of sample introduction efficiency for ICP-MS using the mistral desolvating sample introduction method

Chapter 4. Improvement of sample introduction efficiency for ICP-MS using the mistral desolvating sample introduction method

4.1 Introduction

In Chapter 3, the accuracy of size measurement for nanoparticles using AF4-ICP-MS was investigated. The average size evaluated by AF4-ICP-MS was consistent with TEM and SAXS. On the other hand, the FWHM of size distribution was broadened by the diffusion of particles in case of AF4-ICP-MS. The developed broadening coefficient for AF4 analysis enabled more accurate size measurements.

Next, the detection for nanoparticles must be considered in the case of the application of steel samples to AF4-ICP-MS analysis. It is known that the solid sample direct introduction to ICP must be paid attention carefully from the researches about laser ablation method and slurry sample introduction method. There are differences about sample introduction efficiency and ionization efficiency between solid sample and liquid sample. Especially, the problems about sample introduction efficiency have not ever been solved completely. The solid sample has the lower sample introduction efficiency than liquid sample. Additionally, sample introduction method itself is very low efficiency.

In this Chapter 4, the sample introduction method in ICP-MS analysis was investigated. In the sample introduction system and method in ICP-MS and ICP-AES, these have possibilities of improvement in sensitivity because, generally, only several percent of the total sample amount spraied with a nebulizer can be introduced into plasma [1], and the S/N ratio can be enhanced by selective removal of the matrix. For example, Inagaki et al. [2] reported that the sample introduction efficiency can be improved by inserting a capillary into a conventional concentric double tube nebulizer (triple tube structure) in which the difference between the pressure of the spraied gas in the nozzle and that of the outside atmosphere is utilized, resulting in the generation of further fine droplets (flow focus effect). Many papers have been written with regard to the sensitivity enhancement effect by various desolvation processes (heating-cooling method, gas-exchange method, etc.) of the sample that is transferred to droplets by a nebulizer such as an ultrasonic nebulizer [3, 4].

Among these methods, it is considered that mistral desolvation (MD) is valid to the high efficient transportation of nanoparticle samples. Here, MD method is explained as follows; the sample introduction method equipped with the heating-cooling process is applied to the primary droplets sprayed by a nebulizer, resulting in a solvent removal by selective evaporation and condensation so that the sensitivity can be improved by several times as compared with conventional methods [5]. It was reported that the mechanism of sensitivity enhancement in this

Chapter 4: Improvement of sample introduction efficiency for ICP-MS using the mistral desolvating sample introduction method

method was influenced by at least the following three hypotheses.

1) Suppression effect in generation of polyatomic ion species derived from a solvent [6]

In this mechanism, by selectively removing a solvent before introduction into the plasma, the generation of polyatomic ion species formed between the target element and the solvent is suppressed so that the amount of the target element ion is increased.

2) Effect on sensitivity due to the change in the plasma state [7]

Generally, when a solvent vapor is removed by a desolvation process, the amount of hydrogen atoms in plasma is decreased. Because of this, electron density, thermal conductivity inside the plasma, and energy transmission efficiency from the plasma to the sample decrease, so the ionization temperature becomes lower. It was reported that the optimal ionization position and ionization efficiency in the plasma were changed so that the relative sensitivity was affected. However, because the effect on the sensitivity is dependent on the instrument design, there is no unified view.

3) Improving effect of the sample introduction efficiency [8]

In the general sample introduction system of ICP, because coarse droplets generated in a nebulizer have an adverse effect on plasma stability, the system design is such that the coarse droplets can be removed in advance in a spray chamber so that only fine droplets can be introduced into the plasma. It is presumed that coarse droplets, which have been removed in a spray chamber in conventional introduction methods, are refined in the desolvation process so that they can be transported to the plasma, which leads to improvement in the sample introduction efficiency.

In this Chapter 4, it was verified the sensitivity enhancement mechanism of ICP-MS/AES by the MD method mentioned above to clarify its dominant factor and the basic information for development of a sample introduction system was obtained. Additionally, as a result of an investigation into the application of this method to steel analysis, it was revealed that high sensitivity could be achieved with smaller sample consumption than before and found the possibilities that the target steel samples for analysis may be expanded. Moreover, the application to nanoparticle measurement of MD-ICP-MS analysis was examined. It was especially valid for the sub-micron meter particles over 100 nm. These findings were reported as follows.

Chapter 4: Improvement of sample introduction efficiency for ICP-MS using the mistral desolvating sample introduction method

4.2 Experiments
4.2.1 Reagents

A multi-element standard solution (SPEX Centriprep, XSTC series) and single-element standard solution (SPEX Centriprep, Assurance series) were used for each experiment. The preparation of standard solution for each experiment was conducted adding high-purity nitric acid (Tama Chemicals, TAMAPURE-AA100) and ultrapure water (milli-Q, resistance: 18.2 MΩ, TOC: 8.0 ng mL^{-1}) such that the concentration of nitric acid became to 1 (v/v) %. In analyses of the Japanese Iron and Steel Certified Reference Materials for instrumental analysis, JSS 154-9 and JSS 158-1 were used. The solution for the calibration curve was prepared by dissolving JSS 001-6 (high-purity iron) matrix with hydrochloric acid (Kanto Chemical, reagent grade) followed by the addition of standard metal stock solutions (Kanto Chemical; Cu, Ni, V) to the each concentration, and the volume was fixed with ultrapure water. Three kinds of gold nanoparticles (AuNPs, 10, 50, 100 nm) were purchased from nanoComposix (San Diego, USA). Two kinds of AuNPs (200, 300 nm) were purchased from Sigma-Aldrich Japan (Tokyo, Japan). These AuNPs were dispersed in a citrate buffer.

4.2.2 Instruments

For measurement of trace elements in solution, an ICP-MS spectrometer (Agilent Technologies, Agilent 7500cs) and an ICP-AES spectrometer (Shimadzu, ICPE-9000) were used. For introduction of the sample solution, a mistral desolvating (MD) sample introduction instrument (Elemental Scientific Inc., apex Q) and a micro-flow nebulizer (Elemental Scientific Inc., PFA-400/100 nebulizer) were used (as shown in Fig. 4-1).
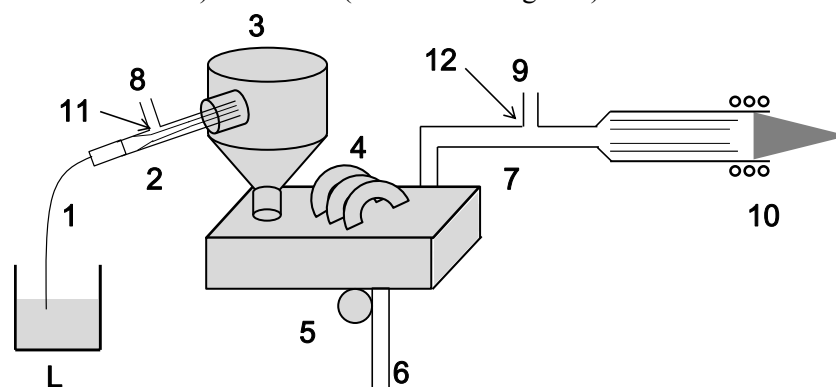
Fig. 4-1   Scheme of the MD instruments. L : liquid sample ; 1 : PFA tube ; 2 : micro-flow nebulizer ; 3 : chamber with heater (373 K／413 K) ; 4 : cooler (275 K) ; 5 : peristaltic pump ; 6 : drain ; 7 : PFA tube ; 8 : Ar carrier gas ; 9 : additional gas ; 10 : plasma torch ; 11 : carrier gas inlet ; 12 : additional gas inlet.

Chapter 4: Improvement of sample introduction efficiency for ICP-MS using the mistral desolvating sample introduction method

As the conventional sample introduction system, a cyclonic spray chamber (Glass Expansion, 50 mL) and a concentric nebulizer (Glass Expansion, Conikal U-Series nebulizer, 1.0 mL min^{-1}) were used. Measurement of the uptake flow rate of the sample was made with a sample flow meter (Glass Expansion, Truflo Sample Monitor). For measurement of the sample's aerosol size distribution, a cascade impactor (DEKATI, ELPI Classic) was used. Ar gas with a purity of 99.9995% was used.

4.2.3 Experimental method

As for the operating conditions of MD, heating temperature was set at two levels: 373 K and 413 K. To study only the desolvation effect, instrument designs (kind of nebulizer, structure of spray chamber, etc.) need to be identical. In this study, the non-heating condition was set at 298 K (room temperature) for comparison. The cooling temperature after heating was set at 275 K. Measurement of ICP-MS and ICP-AES were made with the measurement conditions summarized in Table 4-1.

Table 4-1. Operating conditions for ICP-MS and ICP-AES instruments.

ICP-MS	
Plasma RF power (W)	1140-1400
Ar plasma gas (L min^{-1})	15
Ar carrier gas (L min^{-1})	0.80-0.85
Ar make-up gas (L min^{-1})	0.46
Ar auxiliary gas (L min^{-1})	0.60
Sampling depth (mm)	5-20
Sample uptake rate	self-aspiration (ca. 0.40 mL min^{-1})
ICP-AES	
Plasma RF power (W)	1200
Ar Plasma gas (L min^{-1})	12
Ar carrier gas (L min^{-1})	0.70
Ar auxiliary gas (L min^{-1})	0.60
Exposure height (mm)	10
Sample uptake rate	self-aspiration (ca. 0.40 mL min^{-1})
Exposure time (sec)	15-30
MD	
Nitrogen flow	OFF
Nebulizer	PFA-400/100 (Elemental Sci. Inc.)
Spray Chamber heater (K)	413/373/298 (No-heated)
Spray Chamber cooler (K)	275

Chapter 4: Improvement of sample introduction efficiency for ICP-MS using the mistral desolvating sample introduction method

4.2.3.1 Examination of suppression effect in generation of polyatomic ion species derived from a solvent — Measurement of the oxide-ion generation ratio in ICP-MS

The cerium standard solution (SPEX Centriprep, Assurance PLCE2) with 10 ng mL^{-1} was prepared. By using this solution, the change amount of the generation ratio of an oxide ion of cerium, which is known as one of elements that can most readily produce oxide ion, was examined. The oxide ion generation ratio was calculated from the signal strength ratio of CeO^+ (m/z = 156) to Ce^+ (m/z = 140).

4.2.3.2 Examination of the effect to the sensitivity due to the change in the plasma state — Estimation of the plasma temperature by the Boltzmann plot method

The iron standard solution (SPEX Centriprep, Assurance PLFE2) with 1.0 μg mL^{-1} was prepared. To estimate the plasma temperature, by using this solution the atomic line of Fe (I) was measured by ICP-AES to obtain the Boltzmann plot from 13 different emission strengths (Table 4-2); and from this, the plasma temperatures at each MD heating temperatures were estimated. For making the Boltzmann plot, the Boltzmann equation shown below was used [9].

$$\log\left(\frac{I\lambda}{gA}\right) = -\frac{0.434E_n}{kT} + C \quad (C: \text{constant}) \qquad (\text{Eq. 4-1})$$

$$gA = \frac{8\pi^2 e^2}{mc} \cdot \frac{gf}{\lambda^2} \qquad (\text{Eq. 4-2})$$

where I is the emission strength, λ is the wavelength, g is the statistically weighted value of excited level, A is the transition probability, k is the Boltzmann constant, T is the absolute temperature, E_n is the excitation energy, f is the oscillator strength, e is the elementary charge, m is the mass of electron, and c is the velocity of light.

Chapter 4: Improvement of sample introduction efficiency for ICP-MS using the mistral desolvating sample introduction method

Table 4-2. Measured Fe (I) emission lines and energy transition.

Wave length λ (nm)	E_k (eV)	Lower level	Upper level	gA
370.925	4.257	3d7.(4F).4s	3d7.(4F).4p	1.09E+08
371.993	3.333	3d6.4s2	3d6.(5D).4s.4p.(3P*)	1.78E+08
372.256	3.417	3d6.4s2	3d6.(5D).4s.4p.(3P*)	2.48E+07
372.762	4.284	3d7.(4F).4s	3d7.(4F).4p	1.12E+08
373.332	3.431	3d6.4s2	3d6.(5D).4s.4p.(3P*)	1.94E+07
373.486	4.178	3d7.(4F).4s	3d7.(4F).4p	9.91E+08
373.713	3.369	3d6.4s2	3d6.(5D).4s.4p.(3P*)	1.27E+08
374.826	3.417	3d6.4s2	3d6.(5D).4s.4p.(3P*)	4.58E+07
374.949	4.221	3d7.(4F).4s	3d7.(4F).4p	6.87E+08
375.823	4.257	3d7.(4F).4s	3d7.(4F).4p	4.44E+08
376.379	4.284	3d7.(4F).4s	3d7.(4F).4p	2.72E+08
376.554	6.529	3d7.(2H).4s	3d7.(2H).4p	1.43E+09
381.584	4.734	3d7.(4F).4s	3d7.(4F).4p	7.84E+08

The emission strength *I* of the raw signal strength measured with the ICP-AES instrument was used. In this study, all experiments were conducted with the same instrument configuration and measurement conditions, so that relative plasma temperatures can be compared even without correction of the sensitivity coefficient of the instrument. Other parameters necessary for calculation are cited from the NIST Atomic Spectra Database Lines Form [10].

4.2.3.3   Examination of improving effect of the sample introduction efficiency — Estimation of the sample introduction efficiency by collecting sample transported from MD instrument using the cascade impactor

To examine the change of the sample introduction efficiency, the cerium standard solution with a concentration of 50 μg mL^{-1} was used for MD system, sample aerosols from an outlet of the MD instrument (heating conditions: 298 K and 413 K) were sieved and collected directly on the filter for a period of 30 minutes using the cascade impactor (Fig. 4-2). The cerium contained in the aerosols that were collected on the filter was recovered with the 1 (v/v) % HNO_3 solution and the volume was fixed. The collected amount of cerium was analyzed using ICP-MS, and the size distribution of the aerosols and the sample transportation efficiency were compared.
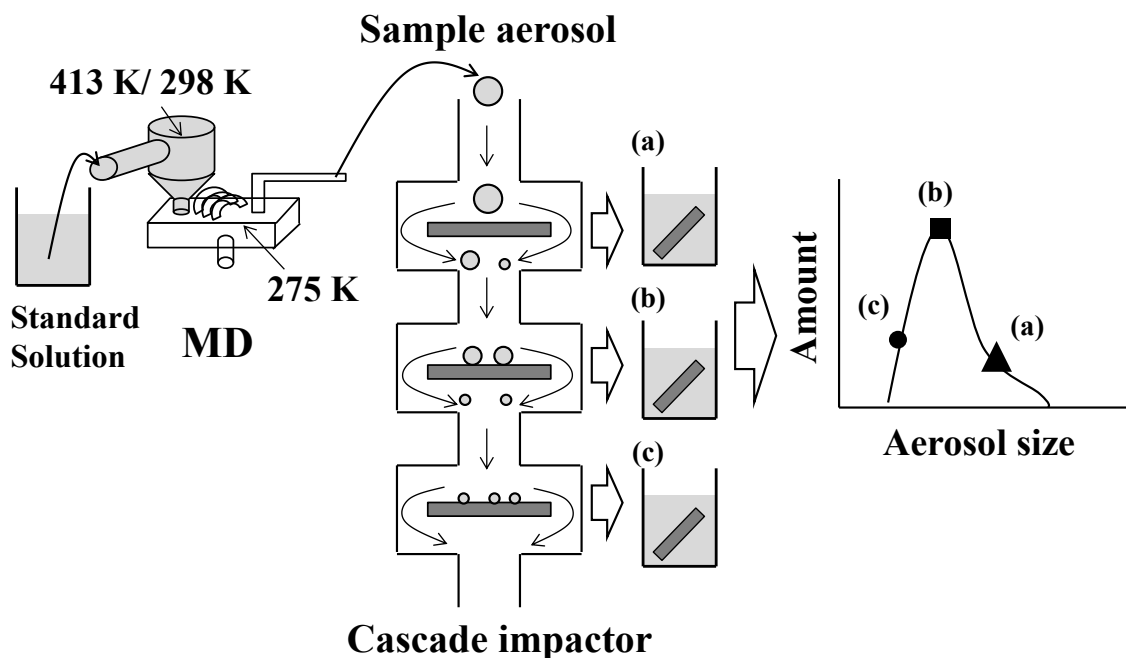
Fig. 4-2   Experimental procedure of the size distribution analysis of sample aerosols by using cascade impactor

4.2.3.4   Analysis of the Japanese Iron and Steel Certified Reference Materials for instrumental analysis

   For MD-ICP-AES analysis, the samples were prepared by the following flow. Firstly, after 0.5 g of samples (Japanese Iron and Steel Certified Reference Materials shown in Table 4-3) was weighed, the samples were decomposed with 20 mL of hydrochloric acid (HCl) in a 200 mL PFA beaker by heating at 473 K on a hot-plate. Then, this solution was fixed to 200 mL adding ultrapure water.

Chapter 4: Improvement of sample introduction efficiency for ICP-MS using the mistral desolvating sample introduction method

Table 4-3. Certified values of CRMs. (Asterisk mark is attached on reference value.)

Unit: mass%

JSS No.	JSS154-9	JSS158-1	JSS001-6
C	0.11	0.14	0.00024
Si	0.60	0.30	0.0001
Mn	1.15	0.47	0.000003*
Ni	0.52	0.048	0.00002*
Cu	0.20	0.16	0.000036
V	0.30	-	<0.00003*
P	0.0045	0.006	0.00005*
S	0.0045	0.007	0.00015
Cr	1.98	0.042	<0.00006*
Mo	0.37	-	<0.00002*
Al	0.009	-	<0.0001*
N	0.0117	-	0.00021
Co	-	0.30	0.000032
Ti	-	0.10	<0.00002*
As	-	0.092	<0.0003*
Sn	-	0.050	0.00003*
Nb	-	0.088	<0.00003*
B	-	-	0.00002*
Ca	-	-	<0.0002*
Mg	-	-	<0.00006*
Pb	-	-	0.000018
W	-	-	0.00001*
Zn	-	-	0.00019

Secondly, the standard solution was prepared as follows. Similarly to above, 0.5 g of high purity iron (JSS 001-6) was weighed. Then, this sample was decomposed with 20 mL of HCl in a 200 mL PFA beaker by heating at 473 K on a hot-plate. And after, the standard solution of Cu, Ni, and V was added to this decomposed solution, and then the volume was fixed to 200 mL so as to give the Cu, Ni, and V concentrations of 0−30 μg mL^{-1} adding ultrapure water. The sample preparation mentioned above was independently carried out twice and measured with MD-ICP-AES under the measurement conditions shown in Table 4-1. Each average values of Cu, Ni, and V was calculated.

4.2.3.5 Application to nanoparticle analysis of MD-ICP-MS

For nanoparticle analysis using MD-ICP-MS method, the samples were prepared by the following flow. Firstly, AuNPs was dissolved with aqua regia. After that, the dissolved AuNPs were diluted with ultrapure water up to one in 10,000. Here, the final concentration of aqua regia was adjusted to be 1 (v/v) %. These samples were named as the dissolved AuNPs. Next, undissolved AuNPs were diluted with ultrapure water to be same concentration above. These samples were named as the dispersed AuNPs. Additionally, the calibration curve was made by using the gold standard solution (SPEX Centriprep, Assurance PLAU3).

These samples were analyzed using MD-ICP-MS. The measurement was repeated three times for one sample.

4.3 Experimental results

4.3.1 Examination of suppression effect in generation of polyatomic ion species derived from a solvent — Measurement of the oxide-ion generation ratio in ICP-MS

As reported by N. Jakubowski et al., it was focused on the Ce ion, which is one of indicator of the oxide ion formation, and compared the oxide-ion generation ratio (CeO^+/Ce^+) at the MD heating temperature of 298 K and 413 K. As a result, the ratios were 0.75% at 298 K (without heating) and 0.51% at 413 K (with heating). A slight decrease in the Ce oxide-ion generation ratio by the MD heating was confirmed, but the decrease was very small, only about 0.24%.

4.3.2 Examination of the effect on the sensitivity due to the change in the plasma state - Estimation of the plasma temperatures by the Boltzmann plot method

The MD instrument was connected to the ICP-AES instrument, and the Boltzmann plot was obtained by measuring the emission lines of Fe (I) to estimate the plasma temperature. Because the plasma source of the ICP-AES instrument used in this experiment is different from that of the ICP-MS, the plasma temperatures must be different to be exact. However, in this experiment, it was expected that a relative comparison could be made by examining the effect of the heating temperature of the MD instrument using the same plasma source of ICP-AES instrument. The heating temperature of the MD instrument was changed in three temperature levels, and the difference in the plasma temperatures in each MD heating temperature was compared (Fig. 4-3).
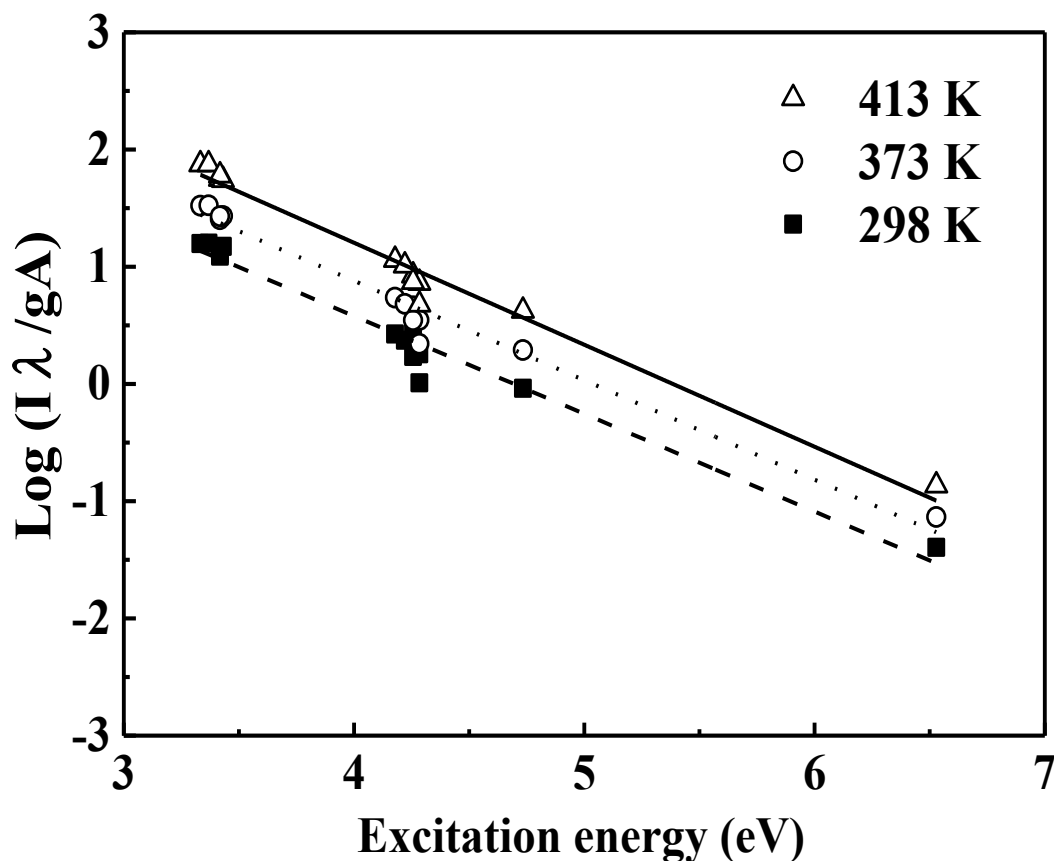
Fig. 4-3   Boltzmann plot upon heating temperature of MD process.
           ■, 298 K; ○, 373 K; △, 413 K.

    Because the sufficient linearity was obtained in all the obtained Boltzmann plots with the correlation coefficient R of about 0.97 to 0.98, the plasma temperatures T_p were calculated from the slopes of these straight lines (Fig. 4-4). As a result, it was found that the plasma temperature in each condition was about 6000 K, and that as the MD heating temperature goes up, the plasma temperature was prone to go down by about 100 to 250 K, which was contrary to expectations.
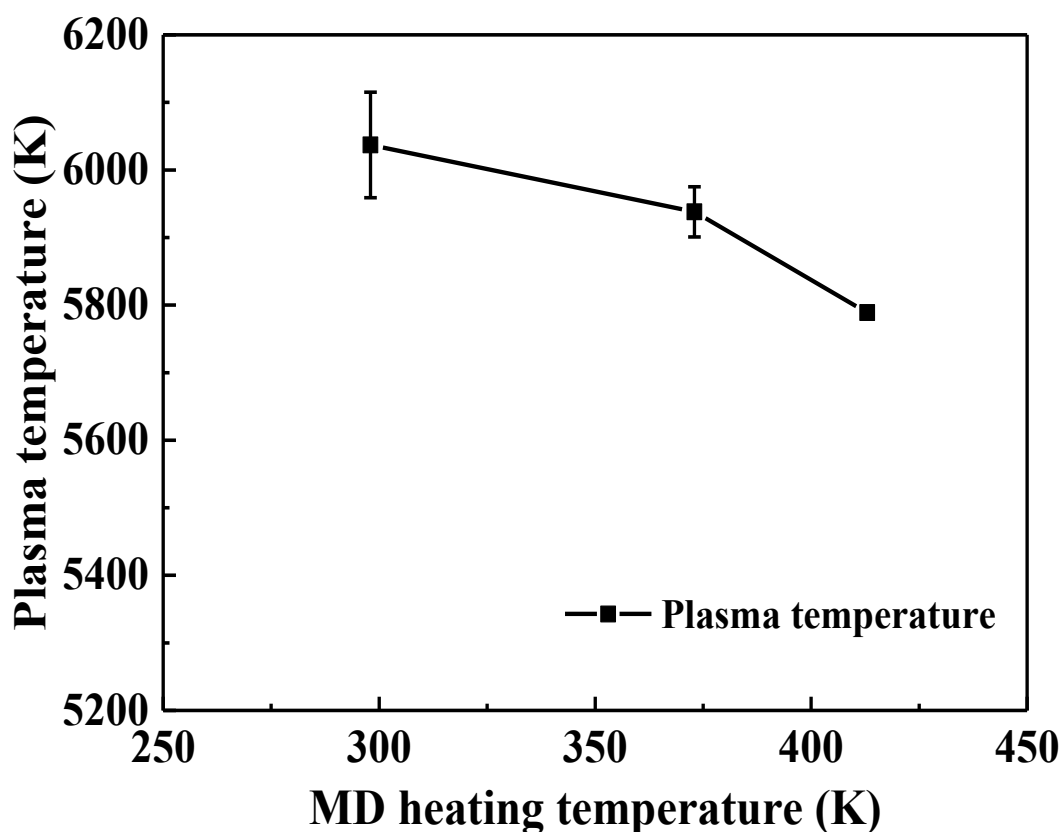
Fig. 4-4   Results of plasma temperature assumption upon heating temperature of MD process.

4.3.3   Examination of improving effect of the sample introduction efficiency — Measurement result of the sample introduction efficiency by the cascade impactor

To examine the change in the aerosol size distribution, the aerosols of the cerium standard solution transported from the MD instrument were directly sampled in each aerosol size using the cascade impactor and quantified using ICP-MS. In this experiment, to eliminate influences on the evaluation of size distribution by the effects of performance of the nebulizer, structure of the spray chamber, and transportation path of the aerosols etc., the size distributions of the aerosols were compared by changing the heating temperature of the MD instrument from 298 K to 413 K (Fig. 4-5(a)). As a result, it was revealed that the total amounts of cerium in the aerosols with the size of less than the cut-off diameter of the spray chamber (ca. 10 μm) was significantly increased by heating of the MD instrument, whereas the average size of the aerosols were not substantially changed as they were 0.26 μm at 298 K and 0.41 μm at 413 K. The average size of these aerosols is depending on the nebulizer, flow rate of the Ar carrier gas, and uptake rate of the sample, etc. For example, K. Kahen et al. [11] reported that the Sauter average diameter ($D_{3.2}$) of the droplets by the laser scattering method was decreased from 12.9

μm to 5 μm or less by combining the micro-flow nebulizer (PFA-100) with the Scott-type spray chamber. Also, P. E. Walters et al. [12] reported that when desolvation was applied at 423 K using an ultrasonic nebulizer without a spray chamber, the droplet size measured with the laser diffraction was decreased to about 3 μm. In this study, because the cyclone-type chamber was used and the cut-off diameter of the cascade impactor was measured, measurement conditions and measurement methods of the droplet size were different from previous reports, so that a comparison cannot be made strictly; however, it was found that the relative tendencies were the same.

Additionally, when the sample introduction efficiency was defined as Eq. 4-3, the efficiency was enhanced from 2.6% at 298K to 12.1% at 413K, i.e., by a factor of about 4.7 times. Thus, it was revealed that the desolvation enabled the transportation of more aerosols than the conventional method (Fig. 4-5(b)).

$$\text{Sample introduction efficiency of solution}(\%) = \frac{\text{Amount of collected sample by CI}}{\text{Amount of uptaked sample}} \times 100 \quad (\text{Eq. 4-3})$$

(a)

(b)
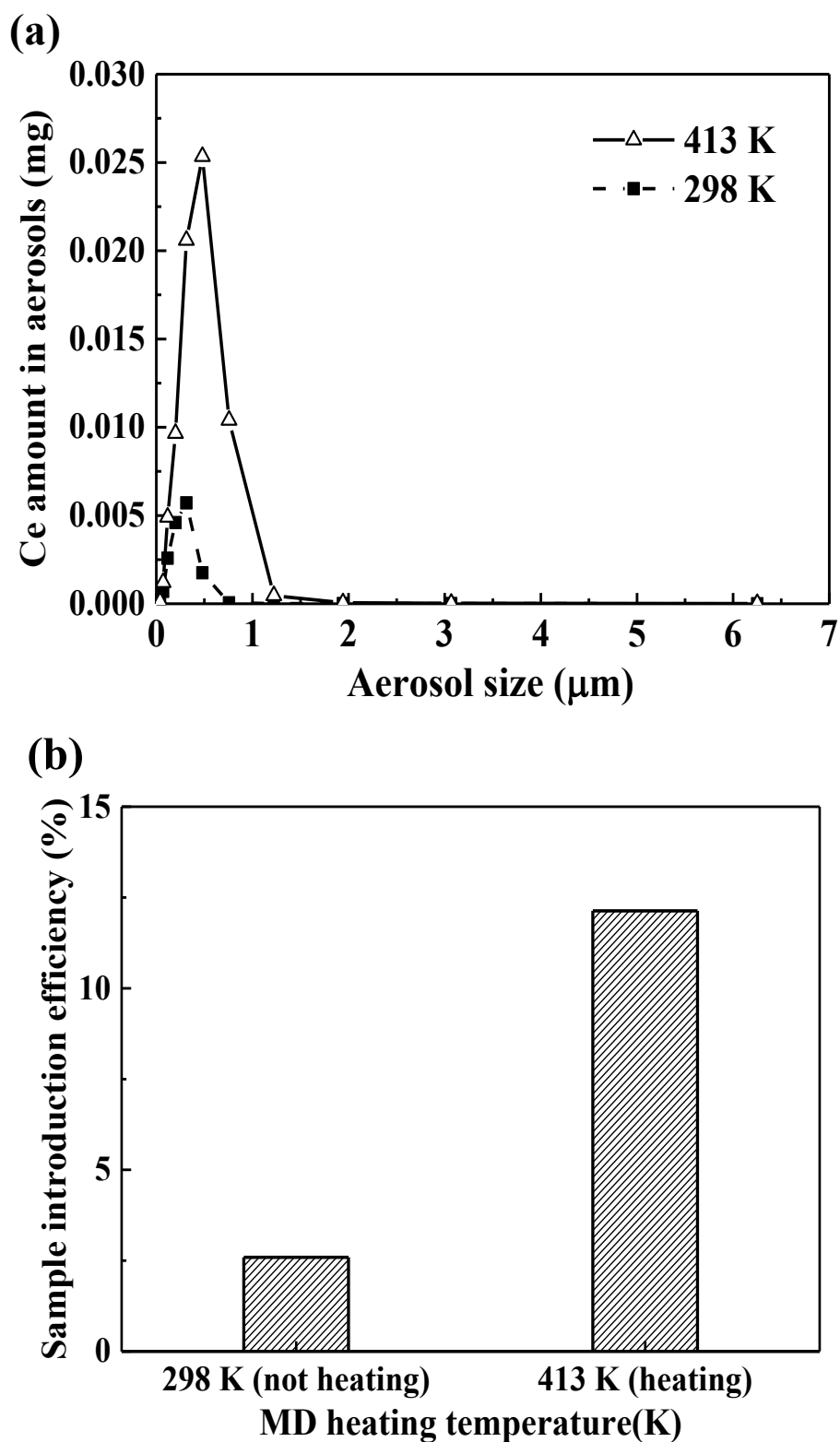
Fig. 4-5   Effect of heating temperature of MD process for aerosol size distribution and introduction efficiency. (a) Aerosol size distribution upon heating temperature of MD process (b) Results of sample introduction efficiency. ■, 298 K; △, 413 K.

4.3.4   Analysis results of the Japanese Iron and Steel Certified Reference Materials for instrumental analysis

The quantified values of Cu, Ni, and V in the Japanese Iron and Steel Certified Reference Materials using the MD-ICP-AES method were summarized in Table 4-4. All measured values agreed well with the certified values, and thus, it was confirmed that this method could be valid for chemical analysis of steel samples. Further, the comparison of the calibration curves between the MD method and the conventional sample introduction method (concentric nebulizer + cyclone-type chamber) was shown in Fig. 4-6.

Table 4-4. Analytical results of CRMs by MD-ICP-AES. (a) JSS154-9, (b) JSS158-1.

(a)   unit: mass%

	Cu	Ni	V
n=1	0.195	0.519	0.294
n=2	0.201	0.533	0.300
Average	0.198	0.526	0.297
Certified value	0.200	0.520	0.300

(b)   unit: mass%

	Cu	Ni
n=1	0.159	0.049
n=2	0.163	0.050
Average	0.161	0.050
Certified value	0.160	0.048
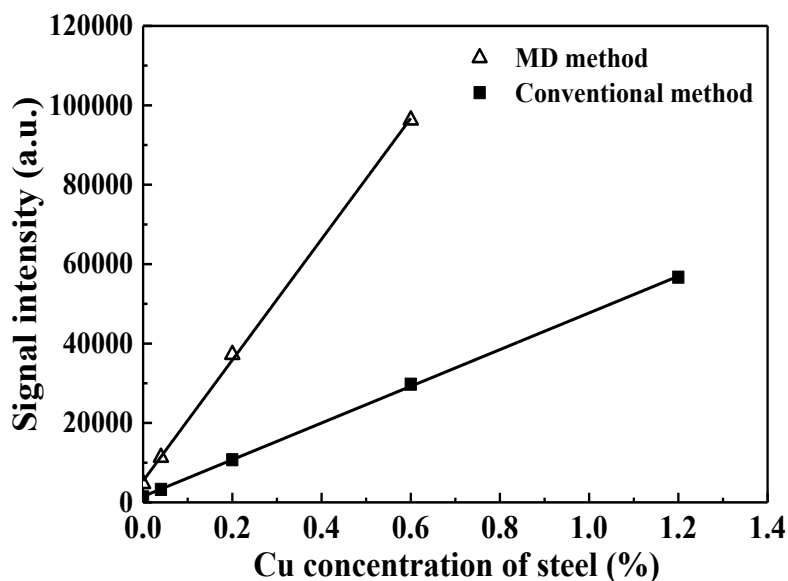
Fig. 4-6 Comparison of Cu (213.598 nm) calibration curve between MD and conventional sample introduction system.

It was found that the slope of the Cu (213.598 nm) calibration curve was increased by a factor of 3.3 times in the MD method. This trend was confirmed in other calibration curves about V and Ni. The slopes of the V (290.882 nm) and the Ni (231.604 nm) calibration curve were increased by a factor of 3.1 times, 2.7 times, respectively (data was not shown). Additionally, the amount of sample uptake using the concentric nebulizer was 1020 μL min^{-1}, while that using micro-flow nebulizer was 116 μL min^{-1} (Fig. 4-7). Thus, it was revealed that micro-flow nebulizer decreased the amount of sample uptake to 11.4 %.
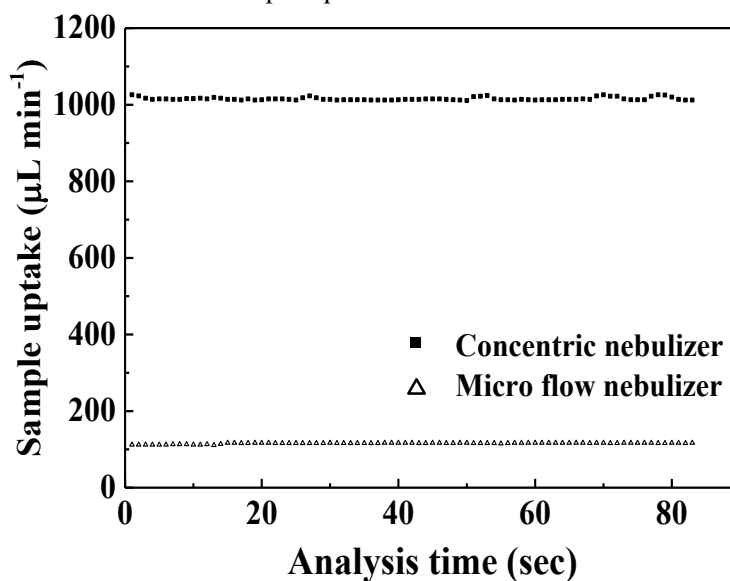
Fig. 4-7 Comparison of sample uptake amounts between concentric nebulizer and micro flow nebulizer.

Chapter 4: Improvement of sample introduction efficiency for ICP-MS using the mistral desolvating sample introduction method

4.3.5   Application to nanoparticle analysis of MD-ICP-MS

Subsequently, it was examined the sample introduction efficiency of nanoparticles. Five of standard gold nanoparticles (AuNPs; primary diameter are 10, 50, 100, 200, and 300 nm, respectively) dispersed in solutions were tested under the same conditions described above. Here, the sample introduction efficiency was calculated from the ratio of gold concentration between dissolved state by acid and dispersed state as nanoparticles as shown in Eq. 4-4.

$$\text{Sample introduction efficiencyof particle (\%)} = \frac{\text{Analyzed value by direct introduction method}}{\text{Analyzed value by acid dissolution method}} \times 100 \quad \text{(Eq. 4-4)}$$

Fig. 4-8 showed the results of sample introduction efficiency for AuNPs with MD-ICP-MS. As a result, no difference was observed at 10 nm size between both solutions, almost 90%. On the other hand, in case of over 100 nm, not-heating MD condition (298 K) showed that the sample introduction efficiency was decreased with increasing particle size, on the contrary, heating MD method (413 K) retained over 85%.
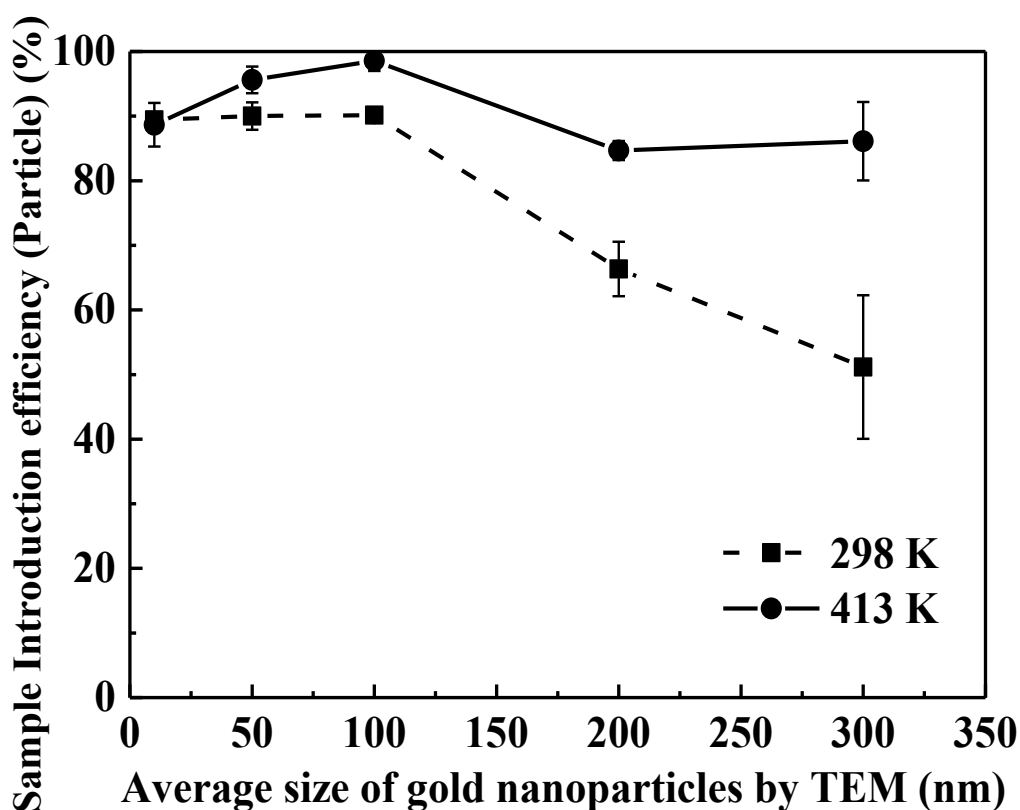
Fig. 4-8   Sample introduction efficiency of each gold nanoparticle. (■:298 K, ●:413 K)

Chapter 4: Improvement of sample introduction efficiency for ICP-MS using the mistral desolvating sample introduction method

4.4 Discussion

As shown below, the experimental results were compared to three hypotheses with regard to the factors for sensitivity enhancement by MD. The dominant factor about sensitivity enhancement by MD was considered. And their applicability for steel analysis was examined.

4.4.1 Suppression effect in generation of polyatomic ion species derived from a solvent

Firstly, the suppression effect on the oxide-ion generation due to solvent removal was suggested. A solvent (water in this study) in each aerosol was separated from the aerosol by evaporation, and concentrated in the cooling section, so that it was selectively removed. Accordingly, the total amount of the solvent that is transported to the plasma must be decreased. Therefore, the reaction between the target element and O_2 in water could be suppressed, resulting in a decrease in the oxide ion and an increase of the target ion. From our experimental results, it was confirmed that the oxide-ion generation ratio decreased slightly by 0.24% due to heating with the MD method. Contrary to this, G. Zhu et al. [13] reported that the ratio of CeO^+/Ce^+ was decreased from 2.5−4% to about 1−2% by lowering the spray chamber temperature from 35°C to 0°C. It could be explained as the effect of solvent removal due to condensation of the solvent vapor by cooling the spray chamber. Also, N. Jakubowski et al. reported that the ratio of YO^+/Y^+ was decreased from 0.54% to 0.14% using a desolvation with a heating section and a cooling section. This result was almost same as our observed result. The effect of heating and cooling in the sample introduction system was summarized as follows.

If only the heating section is equipped, because the transportation amount of the solvent vapor to the plasma is more than the conventional method, oxide ion is generated more; and thus, it is suggested that equipping the cooling section is indispensable to reduce the oxide ion.

There is no report with regard to the extensive study on the relation of oxide-ion generation to the sensitivity; however, the decrease in the oxide-ion generation ratio in these reports was very small, so it was presumed that the sensitivity enhancement effect of more than a factor of 5 times could not be explained only by the suppression effect in oxide-ion generation. Thus, it was suggested that the dominant factor for the sensitivity enhancement effect by the MD method was a factor other than this mechanism.

4.4.2 Effect to the sensitivity due to the change in the plasma state

Secondly, the effect of the change in the plasma state due to the solvent removal was suggested. To confirm the change in the plasma state due to a decrease in the hydrogen atom in

the plasma by desolvation, the plasma temperature was estimated by the Boltzmann plot with ICP-AES.

In past papers, the following findings have been reported. S. E. Long et al. was reported about 900 K decrease in the ionization temperature in case of introducing a mixture of droplets and steam, compared to introducing a mixture of ETV and steam. Besides, N. Jakubowski et al. reported that the solvent load effect was not dependent on the temperature of heating but more on the temperature of cooling, claiming that 80% or more of the solvent can be removed by cooling at 273 K.

To this information, according to the our experimental result, it was found that the plasma temperature tended to drop by about 2°C while raising the MD heating temperature by 1°C. This agrees with the past information; and the reason is discussed as follows. When the heating temperature in the MD instrument was raised, it was presumed that solvent in all aerosol s evaporates to cause decrease in size of the aerosols. At that time, the total amounts of fine aerosols with a size of less than the cut-off diameter of the spray chamber must be increased. This enables more aerosols to be introduced into plasma per unit time. Therefore, the decrease in the plasma temperature can be well explained. Namely, it was presumed that with raising the heating temperature in the MD, the total introduction amount of aerosols increases to cause lowering of the plasma temperature. Besides, this experiment was carried out with the constant temperature of the cooling section at 275 K. Therefore, most of water that was evaporated by desolvation in the heating section was presumably condensed in the subsequent cooling section so as to be transported to the drain section. Thus, it was presumed that the effect of the cooling section on the plasma temperature could be neglected.

In the past reports, dependence of the sensitivity on the change in the plasma temperature has not been discussed in detail; however, because all the present experiments were carried out with the constant cooling temperature, it was presumed that the plasma temperature did not change so much that effect on the sensitivity enhancement was small.

4.4.3   Improving effect on the sample introduction efficiency

Finally, it was suggested that due to the solvent removal effect of the MD method, the amount of the fine aerosols increases. Usually, if a sample solution is sprayed by a nebulizer, aerosols having a wide size distribution are formed. The design of sample introduction system is made such that the plasma can be stabilized by reducing the solvent load. Namely, the large aerosols removed at the spray chamber, only fine aerosols could be introduced into the plasma. Therefore, it is presumed that when the aerosols become smaller by desolvation, more aerosols can be introduced into the plasma to cause enhancement of the sample introduction efficiency, which

leads to an increase in the sensitivity.

From the measurement result of the aerosol size distribution, it was found that the absolute amount of the aerosols with a size of 10 μm or less was drastically increased by heating in the MD instrument while the average size of the aerosols hardly changed. The aerosols measured in this experiment were the aerosols which have passed through the spray chamber so that it could be actually introduced into the plasma. As a whole, the amount of the aerosols with a size of 10 μm or less was increased by heating in MD; and thus, it was presumed that the aerosols which were removed in the spray chamber in advance and not measured were desolvated to cause a size reduction to less than 10 μm so that they can be measured.

Besides, it was confirmed that the sample introduction efficiency was enhanced by a factor of about 4.7 times by heating of the MD instrument, showing that the introduction amount of the aerosols increased. This result almost agrees with the increase by a factor of 2.2 times in the introduction of a slurry sample reported by J. H. D. Hartley et al. And the sensitivity enhancement of cerium in the ICP-MS was a factor of 4.6 times, which is about the same improving effect of the sample introduction efficiency due to the heating in the MD method. Given these facts, this presumably constitutes the largest contribution to sensitivity enhancement.

These examination results were summarized in Table 4-5. In past reports, comparisons were made mainly between the desolvation sample introduction methods (MD method (heating-cooling), or only heating, or only cooling) and usual sample introduction systems (without heating, without cooling); on the other hand, in this report, the effects on the ICP sensitivity with or without heating are compared under the cooling condition at 275 K (constant), so that the comparison condition is different to be exact. As mentioned before, according to the report of N. Jakubowski, most of the solvent vapor is removed only by the effect of cooling; and thus, it is presumed that the influence of polyatomic ion generation ratio and the plasma temperature are improved sufficiently. Accordingly, it is presumed that the improving effect of the sample introduction efficiency due to the heating in the MD method constitutes the largest contribution to sensitivity enhancement.

Table 4-5. Experimental results and influence for ICP sensitivity.

No.	Factor of sensitivity improvement	Our results	Influence for sensitivity
1	Inhibition of poly-atomic ion generation	Approximately 0.2% reduced	Slightly effective
2	Plasma temperature change	100-250 K reduced	Slightly negative
3	Improvement of sample transportation efficiency	Almost 4.7% improved	Most effective

Chapter 4: Improvement of sample introduction efficiency for ICP-MS using the mistral desolvating sample introduction method

4.4.4   Effect of application of the MD method to steel analysis

  Additionally, the results of the Japanese Iron and Steel Certified Reference Materials quantified by the MD-ICP-AES method will be discussed below. When the conventional concentric nebulizer and the micro-flow nebulizer of the MD method are simply compared, the sample uptake amount of the MD method is about one ninth, suggesting the same degree of decrease in the sensitivity. However, as a result of sensitivity comparison between these nebulizers by using the same cyclonic spray chamber, it was revealed that the decrease amount of the relative sensitivity in the micro-flow nebulizer of the MD method is 42% as compared with the conventional concentric nebulizer, which is significantly lower than the expected value of 88.6% (Fig. 4-9).
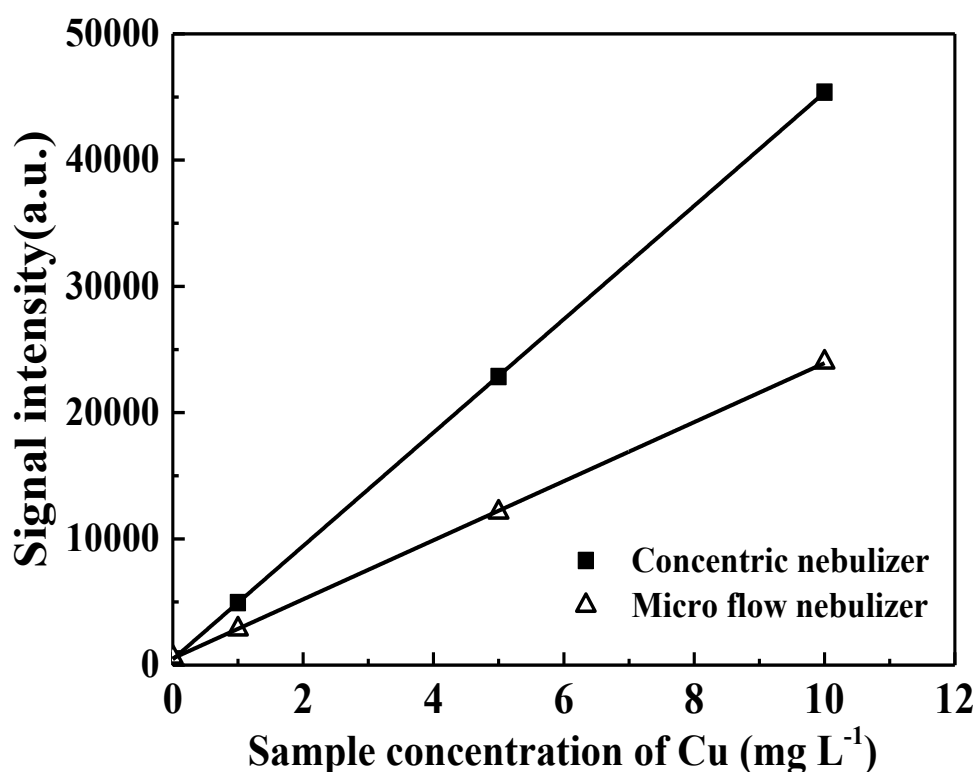
Fig. 4-9   Comparison of sensitivity between concentric nebulizer and micro flow nebulizer measuring Cu 327.396 nm emission line.

  The reason is presumably because the nebulization efficiency of the micro-flow nebulizer is superior to that of the concentric nebulizer. Thus the fine aerosols can be generated more efficiently to cause improvement in the introduction efficiency to the plasma.

  In addition, the sample transportation amount increases by a factor of about 4.7 times by the MD method. Therefore, assuming that the sensitivity of the conventional sample introduction

Chapter 4: Improvement of sample introduction efficiency for ICP-MS using the mistral desolvating sample introduction method

method (concentric nebulizer + cyclone-type chamber) is 1, the relative sensitivity of the MD method is expected to be $(1-0.42)\times4.7\fallingdotseq2.7$ times, which is almost the same as the measured value of 3.0 times. Thus, it can be concluded that by combining the micro-flow nebulizer with the desolvation process of the MD method, not only the sample consumption amount can be reduced to one ninth relative to the conventional method but also the sensitivity can be enhanced by a factor of more than 3 times relative to the conventional method. If this method is applied to the steel analysis for which 0.5 g of the sample dissolution amount was generally required in the past, the amount can be reduced to about 18 mg, about one twenty-seventh relative to the conventional method. Meanwhile, the micro-flow nebulizer used in the MD method employs the same nebulization method as the conventional method, and thus, problems of fouling and clogging due to the iron matrix, having been problematic in the ultrasonic nebulizer, etc. can be avoided. In addition, as mentioned before, the difference in the sensitivity could be explained as only the difference in the sample introduction efficiency, and it was not confirmed that the co-existing iron matrix gives the matrix effect to other element. If the MD method is applied, even in the case that only several milligrams to several tens of milligrams is sampled, for example, a defected part, or a corroded part, etc., of a steel material, wherein the dissolved sample for measurement is small, a high-sensitivity analysis is possible while reducing the sample consumption amount.

4.4.5 Effect of application of the MD method to nanoparticle analysis

Finally, the results of AuNPs analysis using MD-ICP-MS method will be discussed as follows. The nebulization of AuNPs dispersed in solution makes aerosols including nanoparticles, resulted in solvent attached around nanoparticles. As mentioned above, the sample introduction system of ICP-MS and AES has been designed to avoid the introduction of coarse aerosols to the plasma. Therefore, those large aerosols including nanoparticles would be cut off by spray chamber and not transported to ICP-MS, because the increase of nanoparticles size could enlarge aerosols diameter. On the other hand, the heating MD method could vaporize the solvent around nanoparticles selectively, and decrease the size of aerosols including nanoparticles. Thus, it was considered that this method could avoid cutting off by spray chamber, resulted in improvement of sample introduction efficiency.

Also, it was reported that the nanoparticles larger than 500 nm were ionized incompletely and the ionization efficiency was dependent on the elemental composition, which was called as an elemental fractionation effect [14-15]. Moreover, it was necessary to pay attention to a loss of counting mass spectral signal in case of detecting large particles. It was due to the lack of momentary detection ability for the large signal derived from large particles.

Chapter 4: Improvement of sample introduction efficiency for ICP-MS using the mistral desolvating sample introduction method

To achieve more accurate quantification analysis of nanoparticles using MD-ICP-MS method without acid dissolution, not only the sample introduction efficiency but also the ionization efficiency of nanoparticles, and time-resolution for detecting mass spectral signal must be improved more.

4.5　Conclusions

Sensitivity enhancement mechanism upon application of the MD method to ICP-MS/AES was studied, and three factors for the sensitivity enhancement mechanism were examined.

(1) It was confirmed that the oxide ion generation ratio in ICP-MS was slightly decreased (0.24%) by the heating process of the MD method.

(2) The plasma temperature of ICP estimated from the Boltzmann plot method was about 6000 K, and by raising the chamber heating temperature in the MD method, the plasma temperature dropped by about 100 to 250 K.

(3) The aerosols were refined by the MD method, so that the aerosols with a diameter of 10 μm or less, the cut-off diameter of the spray chamber, were drastically increased. Because of this, the transportation efficiency of the aerosols was increased by a factor of about 4.7 times, and thus, it was revealed that this constitutes the largest contribution to the sensitivity enhancement effect.

From the above, it was revealed that the improving effect of the sample introduction efficiency by refinement of the aerosols in (3) mentioned above is a dominant factor for sensitivity enhancement by the MD method.

In addition, it was revealed that the measurement result by MD-ICP-AES agrees well with the certified values of the Japanese Iron and Steel Certified Reference Materials. These results indicate that MD-ICP-AES enables accurate analysis for steel samples. Additionally, MD-ICP-AES provides that the high sensitivity of a factor of about 3 times can be achievable even under the condition that the sample consumption amount is reduced to one ninth. From these results, it is presumed that the sample dissolution amount may be reduced to about one twenty-seventh relative to the conventional method. Thus, MD method can be applied for the case of sampling only several milligrams to several tens of milligrams from a defected part or a corroded part, etc., further study about sample introduction technique is expected to enable the application for various steel samples.

Moreover, it was showed that the MD-ICP-MS analysis could improve the sample introduction efficiency for nanoparticle dispersed samples. The tested AuNPs are introduced over 85% efficiency. From these results, the quantification analysis for particles over 100 nm using AF4-ICP-MS was expected to become more accurate.

Chapter 4: Improvement of sample introduction efficiency for ICP-MS using the mistral desolvating sample introduction method

4.6   References

1. K. Inagaki and K. Chiba: *Bunseki*, **2**(2009), 62.

2. K. Inagaki, S. Fujii, A. Takatsu, and K. Chiba: *J. Anal. At. Spectrom.*, **26**(2011), 623.

3. K.W. Olson, W.J. Haas Jr., and V.A. Fassel: *Anal. Chem.*, **49**(1977), 632.

4. V.A. Fassel and B.R. Bear: *Spectrochim. Acta*, **41B**(1986), 1089.

5. A. Montaser, ed.: "Inductively Coupled Plasma Mass Spectrometry", Wiley-VCH, New York, (1998), 173.

6. N. Jakubowski, I. Feldmann, and D. Stuewer: *Spectrochim. Acta*, **47B**(1992), 107.

7. S.E. Long and R.F. Browner: *Spectrochim. Acta*, **43B**(1988), 1461.

8. J.H.D. Hartley, S.J. Hill, and L. Ebdon: *Spectrochim. Acta*, **48B**(1993), 1421.

9. T. Takahashi and S. Murayama: "Emission Spectroscopic Analysis of Liquid Sample", Japan Scientific Societies Press, Tokyo, (1993), 14.

10. NIST: *Atomic Spectra Database Lines Form,* http://physics.nist.gov/PhysRefData/ASD/lines_form.html, (accessed 2012-10-18).

11. K. Kahen, K. Jorabchi, C. Gray, and A. Montaser: *Anal. Chem.*, **76**(2004), 7194.

12. P.E. Walters and C.A. Barnardt: *Spectrochim. Acta*, **43B**(1988), 325.

13. G. Zhu and R.F. Browner: *J. Anal. At. Spectrom.*, **3**(1988), 781.

14. M. Guillong and D. Günther: *J. Anal. At. Spectrom.*, **17**(2002), 831.

15. M. Guillong, H. Kuhn, and D. Günter: *Spectrochim. Acta,* **58B**(2003), 211.

Chapter 5

Development of sulfur-free surfactant for titanium and vanadium nanoparticle characterization in steel using AF4-ICP-MS

Chapter 5. Development of sulfur-free surfactant for titanium and vanadium nanoparticle characterization in steel using AF4-ICP-MS

5.1 Introduction

In Chapter 3 and 4, the measurement method for nanoparticles using AF4-ICP-MS was investigated from the view of the fundamental studies using AuNPs, AgNPs as standard nanoparticles. As a result, the accuracy for size measurement was improved by the development of broadening coefficient in Chapter 3. Additionally, the quantification analysis of particle concentration was improved dramatically for sub-micrometer particle over 100 nm by using the MD method in Chapter 4.

Here, in this Chapter 5, the application of AF4-ICP-MS analysis for precipitates in steels would be investigated. Especially, this Chapter 5 was focused on the AF4-ICP-MS analysis for nanocarbides because it was reported that some nanocarbides (the carbides of niobium, titanium, vanadium, and molybdenum etc.) have been introduced in steels for obtaining specific mechanical properties [1-3]. However, AF4-ICP-MS analysis has certain problem regarding the spectral interference. For example, because $^{48}Ti^+$, $^{51}V^+$, and sulfur molecular ion species ($^{32}S^{16}O^+$, $^{34}S^{16}O^1H^+$) have almost similar mass-to-charge ratios, quadrupole-type ICP-MS cannot distinguish each ion with sulfur molecular ion species [4]. It was necessary to reduce sulfur molecular ion species concentration or improve the sensitivity of Ti and V. In general, the collision/reaction cell or cool plasma method was applied as a method of overcoming the spectral interference between Ti, V, and sulfur molecular ion species [5]. However, in the case of the collision/reaction cell method, the ion-transmission efficiency of Ti and V is decreased by injecting He for collision gases or O_2 for reaction gases. The O_2 reaction method also generated new ion species (e.g., $^{48}Ti^{16}O^+$) from Ti to change the mass-to-charge ratio. However, a new spectral interference for nickel and zinc can be generated. In the case of cool plasma (e.g., RF 800 W), the plasma temperature and electron density are usually lower than the hot plasma (e.g., RF 1400 W); therefore, the ionization efficiency and sensitivity of titanium and vanadium are insufficient to determine the concentration of trace amounts of each element. Therefore, a common way to solve the spectral interference is the removal of interference components, such as sulfur, from the samples.

Some surfactants must be used to achieve nanoparticle dispersion in the solution for the determination of the actual size distribution and element analysis *via* AF4-ICP-MS. However, if the surfactant contained sulfur, the actual concentration of titanium and vanadium could not be determined *via* ICP-MS because the spectral interferences for $^{48}Ti^+$ and $^{51}V^+$ caused a great decrease of the signal-noise ratio. This is caused by the sulfur molecular ion species (e.g.,

Chapter 5: Development of sulfur-free surfactant for titanium and vanadium nanoparticle characterization in steel using AF4-ICP-MS

$^{32}S^{16}O^+$ and $^{34}S^{16}O^1H^+$). For the actual detection of titanium carbides (TiC) and vanadium carbides (VC) and their size distribution measurement *via* AF4-ICP-MS, sulfur-free surfactants must be used to disperse each particle in the solution.

In this Chapter 5, to disperse TiC and VC after the treatment of steel using the SPEED method as described in subsection 1.2.2 and to determine each concentration and size distribution with high sensitivity using AF4-ICP-MS, sulfur-free surfactants were investigated. First, several surfactants were investigated for the separation ability in AF4 using gold nanoparticles (AuNPs) with different particle sizes to discuss the resolution of particle size measurement. Second, the zeta potentials of AuNPs, TiC, VC, and membrane surface of an AF4 separation channel were investigated when each surfactant was added into suspension. Finally, TiC and VC extracted from a steel sheet were analyzed *via* AF4-ICP-MS to confirm the effects of using a sulfur-free surfactant for the AF4-ICP-MS analysis.

5.2 Experimental

5.2.1 Nanoparticle samples and reagents and chemicals

Three surfactants, namely sodium dodecyl sulfate (SDS, purity ≥95.0%, FUJIFILM Wako Pure Chemical Corporation, Japan); sodium cholate (SC, purity ≥98.5%, FUJIFILM Wako Pure Chemical Corporation); and citric acid (CA, purity ≥98.0%, FUJIFILM Wako Pure Chemical Corporation), were used for the dispersion of nanoparticles and promotion of electric repulsive force between nanoparticles and the AF4 membrane. Acetyl acetone (AA, special grade, FUJIFILM Wako Pure Chemical Corporation); tetra methyl ammonium chloride (TMAC, purity ≥98.0%, Tokyo Chemical Industry Co., Ltd.); and methanol (special grade, FUJIFILM Wako Pure Chemical Corporation) were used for the extraction of particles from steel samples *via* the SPEED method. TiC (total carbon ≥19.2%, average diameter = 1 – 2 μm, FUJIFILM Wako Pure Chemical Corporation) and VC (total carbon ≥16.3%, average diameter = 1 – 3 μm, FUJIFILM Wako Pure Chemical Corporation) were used for measuring the zeta potential.

Commercial AuNPs with different primary particle size were purchased from nanoComposix (USA). Table 5-1 shows the average diameter and dispersive agents of each AuNP. The AuNP concentration in water was adjusted to 50 μg mL^{-1} and used for the calibration of AF4. To verify the AF4 separation ability when using the AF4 carrier solution with different surfactants and organic acids, AuNP-5 and AuNP-2 were used. Ultrapure water (>18 MΩ: Milli-Q water purification system type and Elix UV10, Millipore Corp., USA) was used for diluting the solution samples and preparing AF4 carrier solution.

Chapter 5: Development of sulfur-free surfactant for titanium and vanadium nanoparticle characterization in steel using AF4-ICP-MS

Table. 5-1   Specifications of all AuNPs

Sample	Average diameter (nm)	Dispersant
AuNP-2	2.1 ± 0.3	Glutathione
AuNP-4	4.4 ± 0.8	Tannic acid
AuNP-5	5.5 ± 0.5	Lipoic acid
AuNP-7	6.7 ± 0.7	Tannic acid
AuNP-10	10.4 ± 0.7	Tannic acid

5.2.2   Dynamic laser scattering (DLS) method for characterization of particle size

The hydrodynamic diameter of AuNPs was also measured using the dynamic light scattering method (Zetasizer NanoS, Malvern Panalytical Ltd., UK) in AF4 carrier solution. Gold concentration was adjusted from 2.54 mM to 5.08 mM. The measurement was repeated thrice at 298 K.

5.2.3   Zeta potential measurement system

The zeta potentials on the surface of nanoparticles and membrane of the AF4 separation channel were measured using ELSZ-1 (Otsuka Electronics Co., Ltd., Japan). To measure the zeta potential of the AF4 membrane, a flat-plate cell unit was used. Apparent electrophoretic mobility was measured at different depths in the cell unit using a polystyrene latex particle (ca. 500-nm diameter) whose surface was modified by hydroxypropyl cellulose (molecular weight 30000) as a monitor particle (zeta potential: ca. 0 mV). The zeta potential on the membrane surface was calculated using the obtained data for an electro-endosmosis profile *via* Mori and Okamoto's equation (Eq. 5-1) [6].

$$U_{obs}(Z) = AU_0(Z/b)^2 + \Delta U_0(Z/b) + (1-A)U_0 + U_p \quad (\text{Eq. 5-1})$$

where $U_{obs}(Z)$ is the apparent velocity measured at the position Z, Z is the distance from a center of cell units, $A = 1/[(2/3) - (0.420166/k)]$, $k = a / b$ is the ratio of the side length a and b of cross-section of cell ($a > b$), U_p is the true mobility of a particle, U_0 is the average velocity of a solvent at both the upper and lower sides of cell units, and ΔU_0 is the solvent velocity difference between the upper side and lower side of cell units.

Chapter 5: Development of sulfur-free surfactant for titanium and vanadium nanoparticle characterization in steel using AF4-ICP-MS

5.2.4   Field emission-transmission electron microscopy (FE-TEM)

For performing TEM observations of nanoparticles in the steel sheet, mechanical polishing of the surface was first conducted up to one quarter depth from the surface. Then, chemical polishing was conducted using a colloidal silica abrasive to remove surface pollution from the sample. Crystal orientation of the steel sheet was identified using electron backscatter diffraction (EBSD; Quanta3D FEG, FEI Inc., USA) to observe the steel sheet from $<001>_\alpha$ direction. The thin-film sample for TEM observation was fabricated using the FIB lift-out method [7]. After processing using FIB, the thin-film sample was polished by Ar ion beam to remove any damage to the sample caused during FIB processing. This sample was observed in STEM mode using field emission-TEM (FEI Titan^3 60-300 (FEI Inc.)) under an acceleration voltage of 300 kV and convergence angle of 30 mrad.

5.2.5   Sample preparation using the electrolytic extraction method for steel

To disperse nanoparticles in steels into a solution, the extraction process of particles from steel samples *via* the SPEED method was conducted as follows. First, the steel sheet containing nanometer-sized carbides was cut into a 25 mm × 25 mm × 2 mm square to be used as an anode sample. The weight of this anode sample was about 10.0 g. Table 5-2 displays the chemical composition of the steel sheet.

Table. 5-2   Chemical composition of a steel sheet

(mass %)

C	Si	Mn	P	S	Ti	V	sol-Al	N
0.093	0.06	0.48	0.001	0.001	0.20	0.26	0.027	0.0012

Then, the steel anode sample was placed in the electrolytic extraction system. Next, 0.98 M AA and 91.24 mM TMAC were mixed into the methanol solution with 1.73 mM SDS or 1.16 mM SC, and this solution (SPEED solution) was used for the electrolytic extraction, which was conducted in two steps under a constant 500-mA current. The first step was operated for 15 min to remove surface pollution and the oxide layer from the sample. To separate surface pollution and the oxide layer from the sample, a second step was conducted for 120 min in another electrolytic solution containing the same components. After 120 min of electrolytic treatment, almost 1.0 g of the steel anode sample was dissolved into the solution and nanometer-sized carbides in the sample were dispersed into the electrolyte solution.

Chapter 5: Development of sulfur-free surfactant for titanium and vanadium nanoparticle characterization in steel using AF4-ICP-MS

5.2.6 AF4-ICP-MS

AF4 instrument same as chapter 3 was used also in this chapter. Additionally, the online elemental information of the separated nanoparticles by AF4 was obtained using ICP-quadrupole MS (XSeries II, Thermo Fisher Scientific, USA). This instrument was directly connected to the PEEK tube at the outlet from the UV detector of the AF4 system. The solution with nanoparticles was introduced to this system using a sample introduction system with a self-aspirating nebulizer PFA-ST (Elemental Scientific Inc., USA) and a spray chamber apex Q desolvating system equipped with a heater and Peltier chiller (Elemental Scientific Inc.). The operating conditions of the AF4−UV−ICP-MS system are summarized in Table 5-3.

Table. 5-3   Operating conditions of AF4-UV-ICP-MS. (a) AF4-UV, (b) ICP-MS

(a) Wyatt Eclipse AF4 Operating condition of instrument		
Elution solvent in AF4	1.73 mM SDS, 1.16 mM SC, 5.20 mM CA, or Ultrapurewater	
Separation channel type	Asymmetric diamond shaped long channel (Length = 275 mm)	
Spacer thickness in separation channel	490 μm	
Material of membrane in separation channel	Regenerated cellulose (RC; cut-off 5 or 30 kDa)	
Injection volume of each sample	50 μL (AuNPs), 100 μL (metal carbide in steel sample)	
Absorbance wavelength at UV detector	254 nm	
Separation condition in AF4 analysis		
Fractionation time	Elution time	1 minute
	Focusing time	1 minute
	Focus +Injection time	2 minutes
	Focusing time	1 minute
	Elution time	30 minutes
Fractionation step, flow and volume	Injection flow (V_i)	0.2 mL min^{-1}
	Channel flow (V_{out})	1.0 mL min^{-1}
	Cross flow (V_c)	4.0→0 mL min^{-1} (linear gradient for an elution time)
	Focus flow (V_f)	3.0 mL min^{-1}

Chapter 5: Development of sulfur-free surfactant for titanium and vanadium nanoparticle characterization in steel using AF4-ICP-MS

(b) Thermo Xseries 2 ICP-MS Operating condition of instrument	
RF power (W)	1400
Nebulizer flow (L min^{-1})	0.93
Cooling gas (L min^{-1})	15
Auxiliary gas (L min^{-1})	0.87
Sampling depth (mm)	15
Selected mass-charge ratio of each element (m/z)	Ti (47), Ti (48), V (51)
MD heater temperature (K)	413
MD cooling temperature (K)	275
Duration time at each m/z (msec)	100

Prior to the AF4 measurements, the membrane was conditioned with AF4 carrier solution containing different surfactants for at least 30 min. For the calibration of particle size distribution measurement using this AF4 system, gold nanoparticles (AuNPs), whose primary diameters were determined using TEM, were used. Thereafter, the size distribution of nanometer-sized carbides extracted using the SPEED method was measured *via* AF4. The gold concentration in diluted suspension was adjusted from 5 to 25 μg mL^{-1} using AF4 carrier solution containing different surfactants. Before the AF4 separation, all sample solutions with nanoparticles were percolated using a PTFE syringe filter having 1.0-μm pore size and 30-mm diameter (GE Healthcare Life Sciences, USA) to remove large particles and aggregates. After the filtration, each sample was injected into the AF4 separation channel using an auto sampler. Finally, a five-point adjacent average smoothing of AF4-ICP-MS data on the size distribution of each element was performed using the OriginLab pro software (OriginLab Corporation, USA).

Chapter 5: Development of sulfur-free surfactant for titanium and vanadium nanoparticle characterization in steel using AF4-ICP-MS

5.3   Results and Discussion

5.3.1   Selection of surfactants for the AF4 measurement of AuNPs

First, the size distribution of AuNP-5 in the AF4 carrier solution containing different surfactants and organic acid was measured *via* DLS (Fig. 5-1). Compared with the mean size displayed in Fig. 5-1(a) in water without the addition of surfactant, the mean hydrodynamic diameter of AuNP-5 (mean primary diameter: 5.5 ± 0.5 nm) was decreased with the addition of SDS and SC as surfactants, as shown in Figs. 5-1(b) and 5-1(c). Conversely, CA caused an increase in the hydrodynamic diameter of AuNP-5, as shown in Fig. 5-1(d). Therefore, it was revealed that SDS and SC were effective for the dispersion of AuNP-5. Contrastingly, CA promoted an aggregation of AuNP-5. To discuss these results, the zeta potential of AuNPs in solution containing different surfactants was measured *via* laser Doppler electrophoresis. Fig. 5-2 shows the results of the zeta potential measurement of AuNPs. SDS, SC, and ultrapure water without surfactant yielded a high absolute value of zeta potential for AuNP-5 and AuNP-2, whereas CA yielded a low absolute value of zeta potential. Since SDS and SC yielded and maintained a high absolute value of zeta potential of AuNPs in solution, the stable dispersion of AuNPs could be kept. On the contrary, the low absolute value of zeta potential promoted the particle aggregation with the addition of CA.
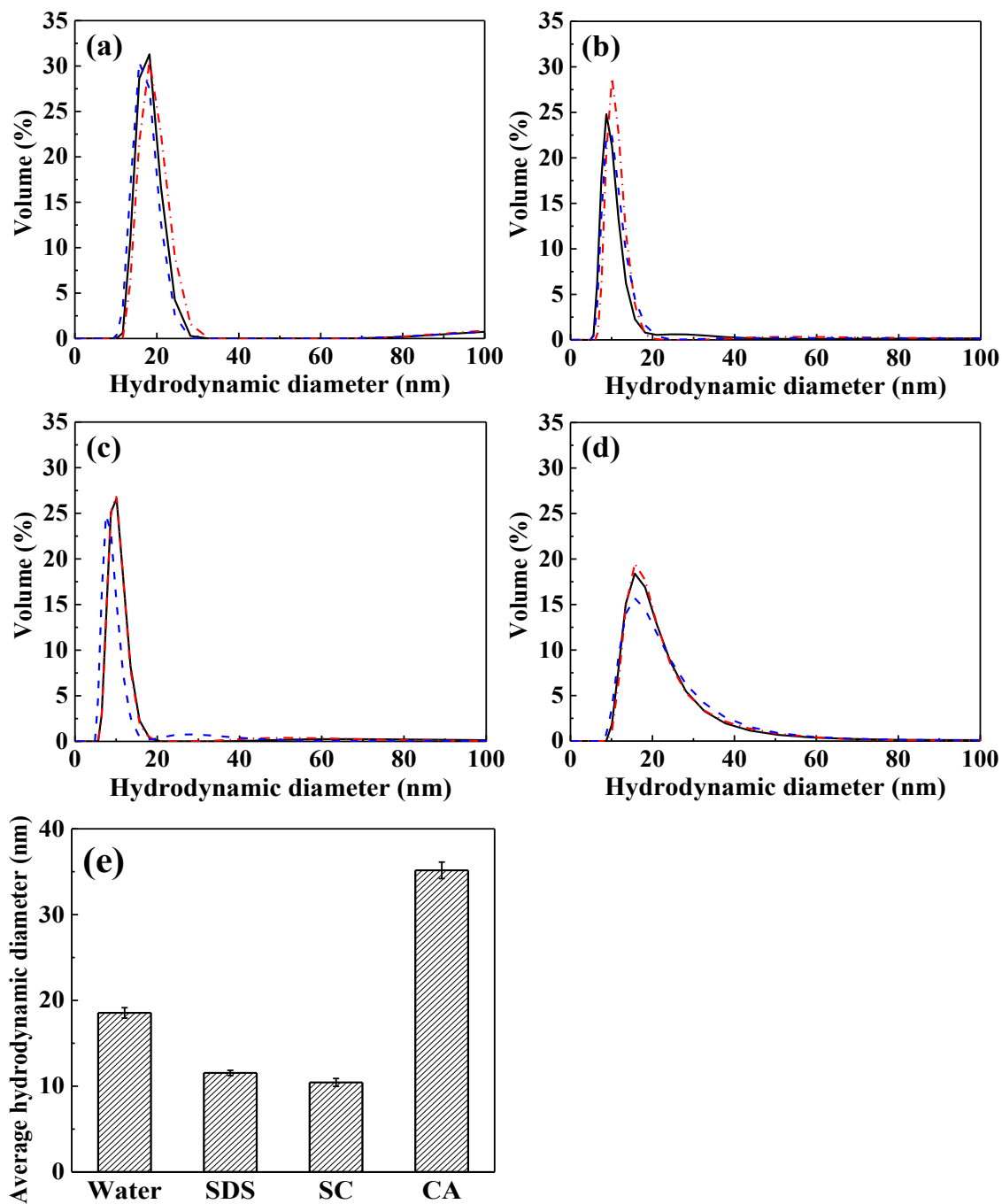
Fig. 5-1   Size distribution and average diameter of AuNP-5 (mean primary diameter: 5.5 ± 0.5 nm) using DLS, which was repeated thrice (N = 1 – 3). The size distribution of AuNP-5 with (a) ultrapure water, (b) 1.73 mM SDS, (c) 1.16 mM SC and (d) 5.20 mM CA and (e) the average hydrodynamic diameter of AuNP-5 with each solution.
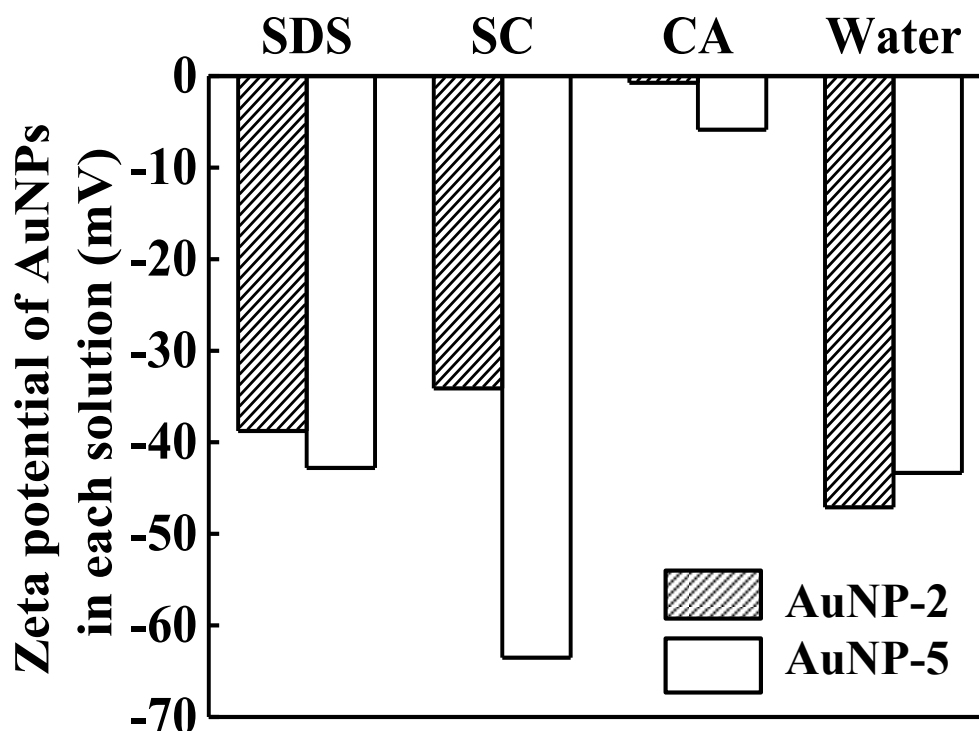
Fig. 5-2   Zeta potential of AuNPs in each solution. The concentration of SDS, SC and CA was adjusted to 1.73 mM, 1.16 mM and 5.20 mM, respectively. Both zeta potentials were different between AuNP-2 (left hatched bar) and -5 (white bar) because of different dispersants.

5.3.2   Separation of AuNPs using the AF4 system in different aqueous solutions

The AF4 separation performance was investigated using the AuNP mixture containing different surfactants and organic acids. In this experiment, the mixture of AuNP-2 and AuNP-5 had equivalent mole ratios. AF4 carrier solutions containing either 1.73 mM SDS, 1.16 mM SC, or 5.20 mM CA were prepared. Fig. 5-3 shows the results of the AF4 separation of the AuNP mixture containing different surfactants. SDS and SC could separate AuNP-2 and -5 *via* AF4. Contrastingly, the AuNP-2 and -5 mixtures could not be separated in CA solution and ultrapure water. Sötebier *et al.* reported that a part of silver nanoparticles (AgNPs) were absorbed on the polyethersulfone (PES) membrane surface during AF4 separation and that the recovery ratio of nanoparticles was $55.65 \pm 0.82\%$ [8]. AuNPs might be strongly absorbed on the RC membrane surface of the AF4 separation channel in the case of using the AF4 carrier solution with CA. The AuNP mixture was also detected as one broad elution peak in the case of using ultrapure water as the AF4 carrier solution. These results must be investigated in detail to reveal the influence of the AF4 carrier solution component on the AF4 separation.
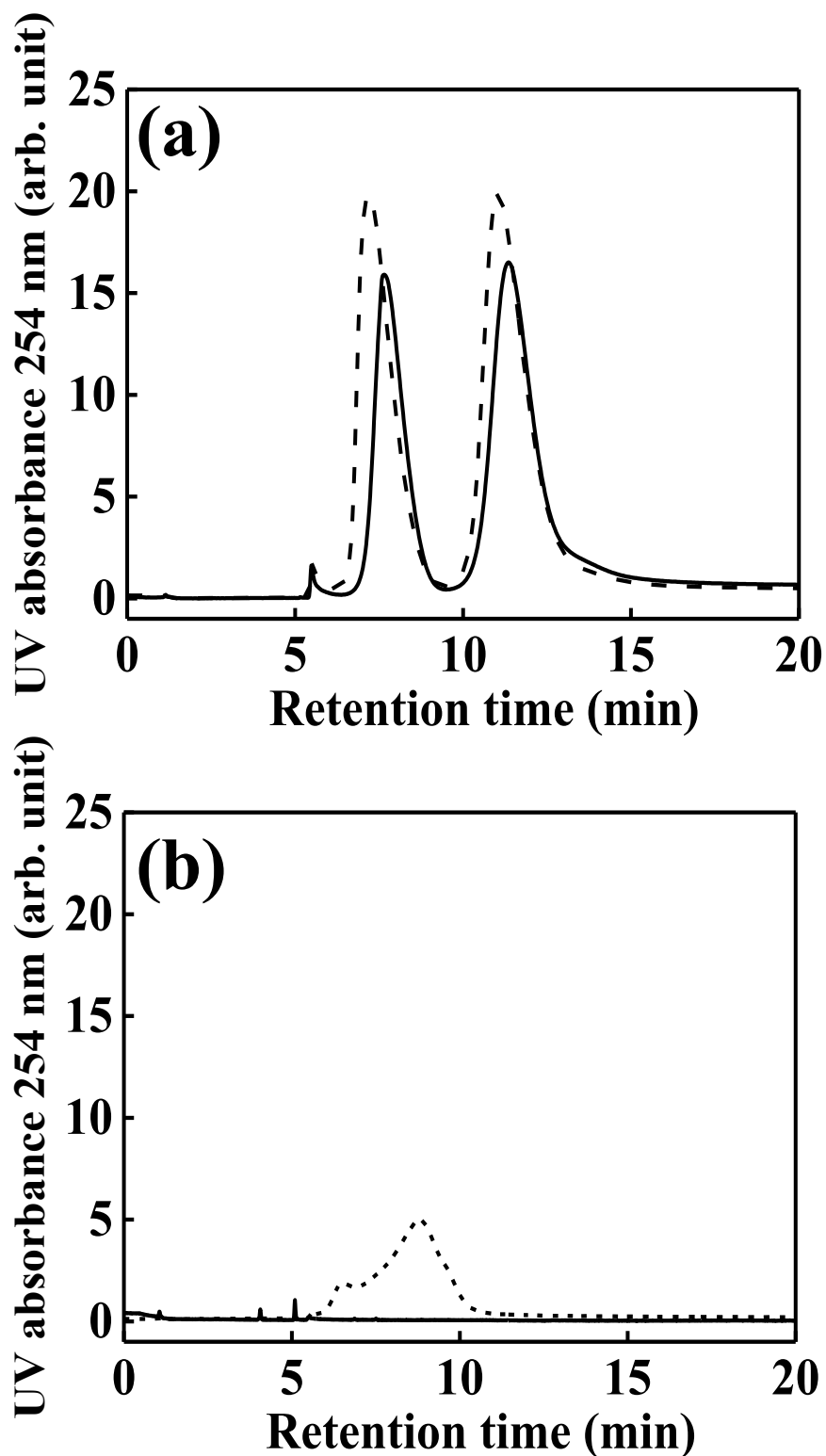
Fig. 5-3 Separation of two types of AuNPs by AF4 using RC 30 kDa membrane and AF4 carrier solutions. (a) 1.73 mM SDS (straight line) and 1.16 mM SC (dotted line) and (b) 5.20 mM CA (straight line) and water (dotted line).

Chapter 5: Development of sulfur-free surfactant for titanium and vanadium nanoparticle characterization in steel using AF4-ICP-MS

5.3.3　Measurement of zeta potential on the membrane in various aqueous solutions

The zeta potential of the membrane surface in the AF4 separation channel was investigated to survey the relation between the AF4 carrier solution component and the AF4 separation performance. In previous literature [9, 10], it was reported that the zeta potential on the membrane surface has a considerable influence on the AF4 separation performance. Based on these studies, the zeta potential on the RC 30 kDa membrane was measured at each AF4 carrier solution. Fig. 5-4 shows the results of the zeta potential on the RC membrane with each AF4 carrier solution.
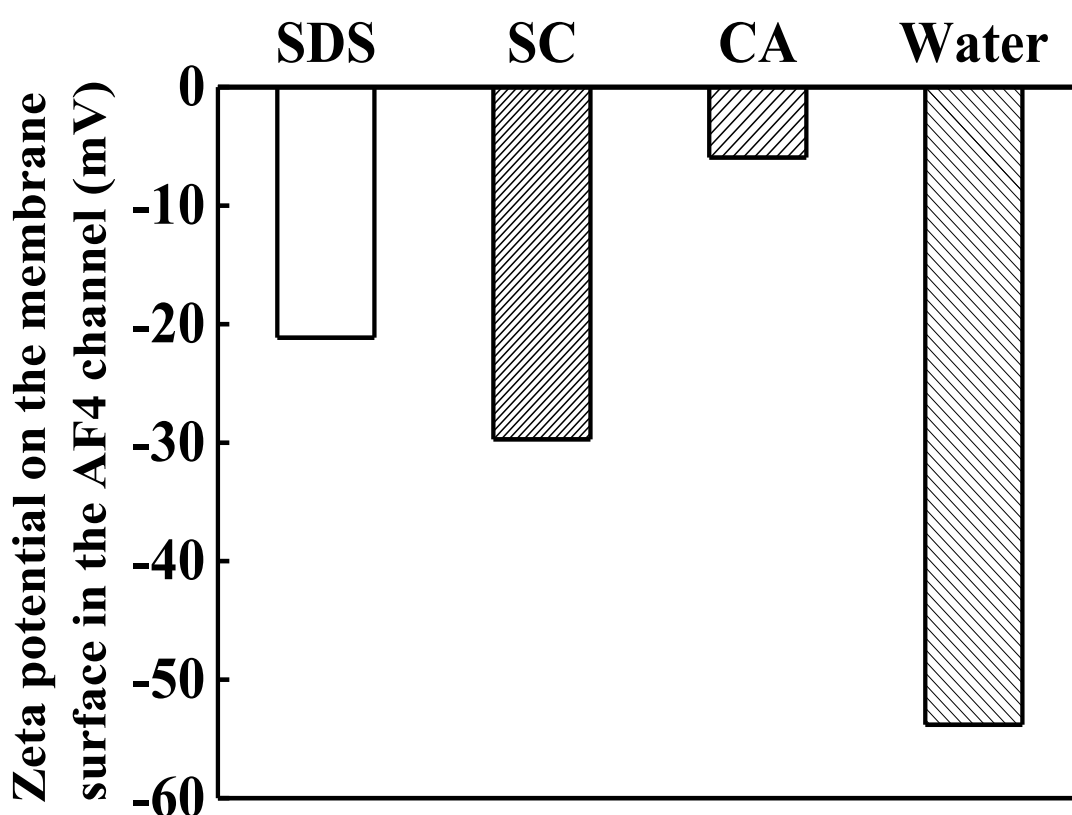
Fig. 5-4　Zeta potential on the RC 30 kDa membrane surface using different solutions.

It was revealed that SC and SDS have an approximately equivalent zeta potential from −20 to −30 mV. Contrastingly, CA had a zeta potential of less than −10 mV and ultrapure water had a zeta potential higher than −50 mV. It was thought that this difference of zeta potential occurred because the cation derived from surfactants existed near the membrane surface. AuNP separation was achieved successfully with the proper zeta potential on the membrane from −20 to −30 mV; zeta potential that is too low or high on the membrane might influence the AF4 separation of the nanoparticles. It was assumed that the zeta potential on the membrane surface

has an influence on AF4 separation as follows.

Since the low absolute value of zeta potential on the membrane surface causes a weak electrostatic repulsion between the membrane and the nanoparticles, the nanoparticles might be physically absorbed on the membrane due to the van der Waals interaction and the nanoparticles may remain undetected by each AF4 detector. Contrastingly, a too high absolute value of zeta potential on the membrane surface gives a strong electrostatic repulsion between the membrane and the nanoparticles. While the focusing process is under operation, the nanoparticles receive too strong an electrostatic repulsive interaction on the membrane that might influence the diffusion mobility in the AF4 separation channel, and the nanoparticles might not follow the AF4 separation principle propounded by Giddings [11]. Therefore, the zeta potential has to be adjusted to the optimum value for accurate AF4 separation performance of the nanoparticles.

5.3.4　Separation of TiC and VC in the steel sheet *via* the AF4 system using aqueous solutions

First, titanium and vanadium carbides ((Ti, V) C) in the steel sheet were observed using FE-TEM and their chemical components were analyzed using EDS. Fig. 5-5 shows a high-angle annular dark field scanning TEM (HAADF-STEM) image and EDS spectra of a thin-film sample.

There were several fine precipitated nanoparticles along the interphase boundary lines of a grain. Titanium and vanadium were selectively detected from these nanoparticles using the EDS analysis. Because the EDS spectra of the nanoparticles involved the EDS signals around the nanoparticles, the steel matrix was also detected at the same time. The difference of these signal intensities was not observed between the nanoparticles and the steel matrix. Thus, iron, silicon, and manganese were identified as solid solute elements in the steel sheet.
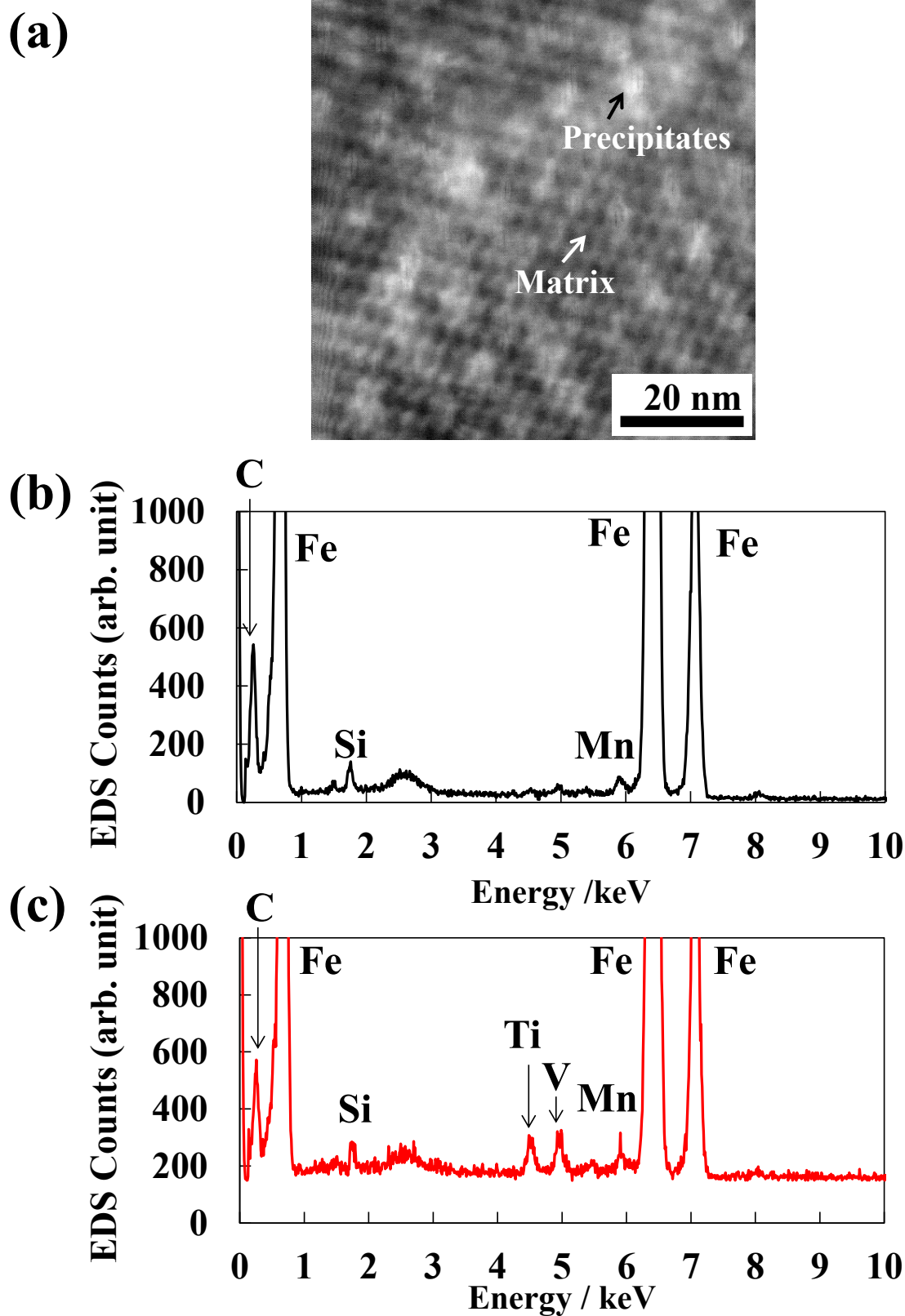
(a)

(b)

(c)

Fig. 5-5   Observation and elemental analysis of a thin-film steel sheet *via* FE-TEM-EDS. (a) HAADF-STEM image and EDS spectra of (b) the matrix and (c) precipitates.

Chapter 5: Development of sulfur-free surfactant for titanium and vanadium nanoparticle characterization in steel using AF4-ICP-MS

Additionally, the nanoparticles extracted from the steel sheet using the SPEED method were collected on the nuclepore membrane filter and measured by X-ray diffraction (XRD), as shown in Fig. 5-6. The XRD result indicated only titanium and vanadium carbides for nanoparticles. Additionally, the chemical compounds involving iron were not detected within the XRD detection limit. Based on the above EDS and XRD results, the main components of nanoparticles were identified as (Ti, V) C_2 [12].
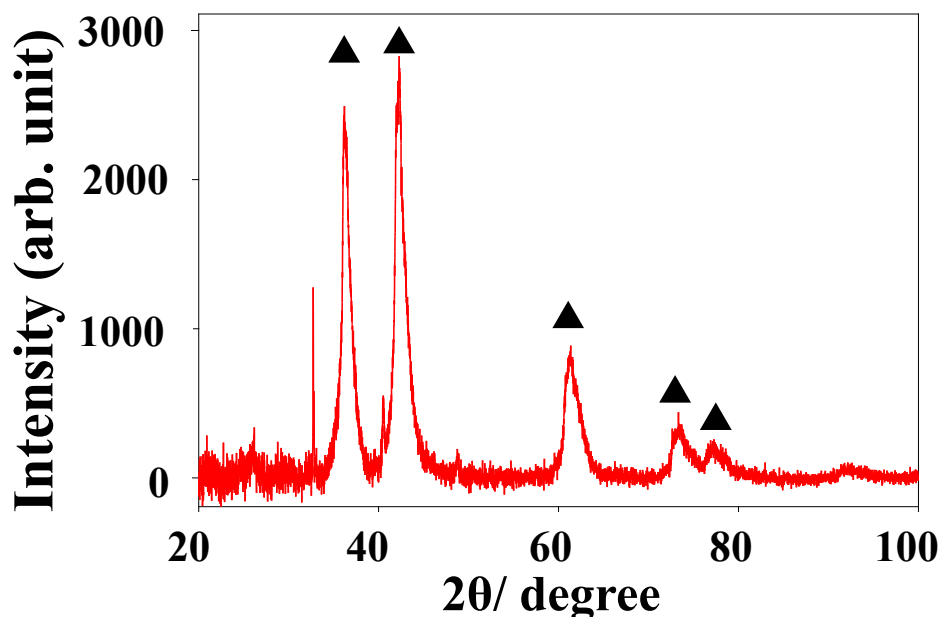

Fig. 5-6   XRD pattern of nanoparticles extracted from the steel sheet using the SPEED method. The peaks of black triangles showed the compound of (Ti, V) C_2.

Second, the application of AF4-ICP-MS analysis with sulfur-free surfactant was conducted. At first, to investigate the influence of particle dissolution to the SPEED solution, TiC and VC reagents were used for the gravimetric analysis. These reagents were immersed in another SPEED solution with chelating agent and electrolyte for two hours. And then, these reagents were collected on the nuclepore membrane filter with suction filtration, and the changes in weight were measured. As a result, the weight of particles was almost unchanged and the recovery was 98.7% and 96.5%, respectively. It was thought that the loss of a few percentages in the recovery was due to the sample loss at the suction filtration. Thus, the influence of particle dissolution was negligible. Next, (Ti, V) C_2 was extracted from the steel sheet using the SPEED method prior to the AF4-ICP-MS analysis. Thereafter, the size distribution and the elemental component of these solution samples were measured using AF4-ICP-MS under the conditions summarized in Table 5-3. The 1.73 mM SDS and 1.16 mM SC solutions were used for the AF4-ICP-MS measurement to facilitate good dispersion of nanoparticles and prevention of adhesion on the RC membrane. The cut-off diameter of molecular weight did not affect the

Chapter 5: Development of sulfur-free surfactant for titanium and vanadium nanoparticle characterization in steel using AF4-ICP-MS

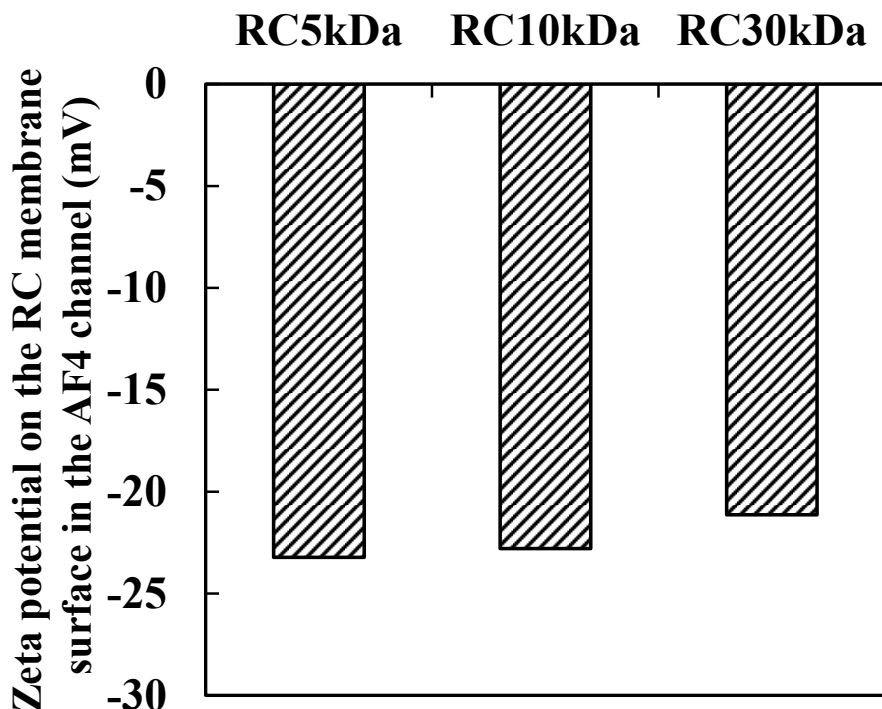zeta potential on the membrane in the AF4 separation channel, as shown in Fig. 5-7.

Fig. 5-7   Zeta potential on the membrane with each the cut-off diameter of molecular weight in the AF4 separation channel. 1.73 mM SDS was used for AF4 carrier solution.

Fig. 5-8 shows the results of the size distribution measurements in different surfactant solutions performed using AF4-ICP-MS. Mass-to-charge ratio (m/z) of titanium was set to 47 due to a high detection limit at m/z 48 in the case of the SDS solution in Fig. 5-8(a). This phenomenon was caused by the mass spectral interference by $^{32}S^{16}O^+$ generated from sulfur in the SDS solution. In Ar plasma, sulfur often reacts with oxygen, resulting in the generation of sulfur molecular ion species such as $^{32}S^{16}O^+$ and $^{34}S^{16}O^1H^+$. Thus, it is necessary to remove sulfur molecular ion species for the sensitive detection of titanium and vanadium by ICP-MS. Herein, a titanium isotope was selected for the removal of the influence of sulfur molecular ion species, but the natural abundance of ^{47}Ti was one-tenth of ^{48}Ti. The detection sensitivity was not good in ICP-MS. However, the approach using titanium isotope was better than the ^{48}Ti detection in the presence of a high sulfur matrix. $^{34}S^{16}O^1H^+$ caused the mass spectral interference at m/z 51 in the case of the vanadium detection using ICP-MS. However, it was not preferable to use the vanadium isotope of m/z 50 because most of vanadium exists as m/z 51 (natural abundance 99.75%) and 5.4% of titanium exists as the isotope of m/z 50. For this reason, m/z 51 was selected in the case of vanadium. Therefore, the ^{47}Ti and ^{51}V mass spectra corresponding to (Ti, V) C_2 were not detected by AF4-ICP-MS and had a signal intensity almost similar to only AF4 carrier solution with SDS. Conversely, ^{47}Ti, ^{48}Ti and ^{51}V were detected by

Chapter 5: Development of sulfur-free surfactant for titanium and vanadium nanoparticle characterization in steel using AF4-ICP-MS

AF4-ICP-MS in the case of the SC solution. The ^{47}Ti, ^{48}Ti and ^{51}V detection could be achieved at a high sensitivity because SC has no sulfur in its molecular structure. Therefore, the existence of sulfur could be a reason for the difference in (Ti, V) C$_2$ detection when using SDS and SC solutions. Furthermore, the removal of these matrix components could be the best way to eliminate mass spectral interferences.
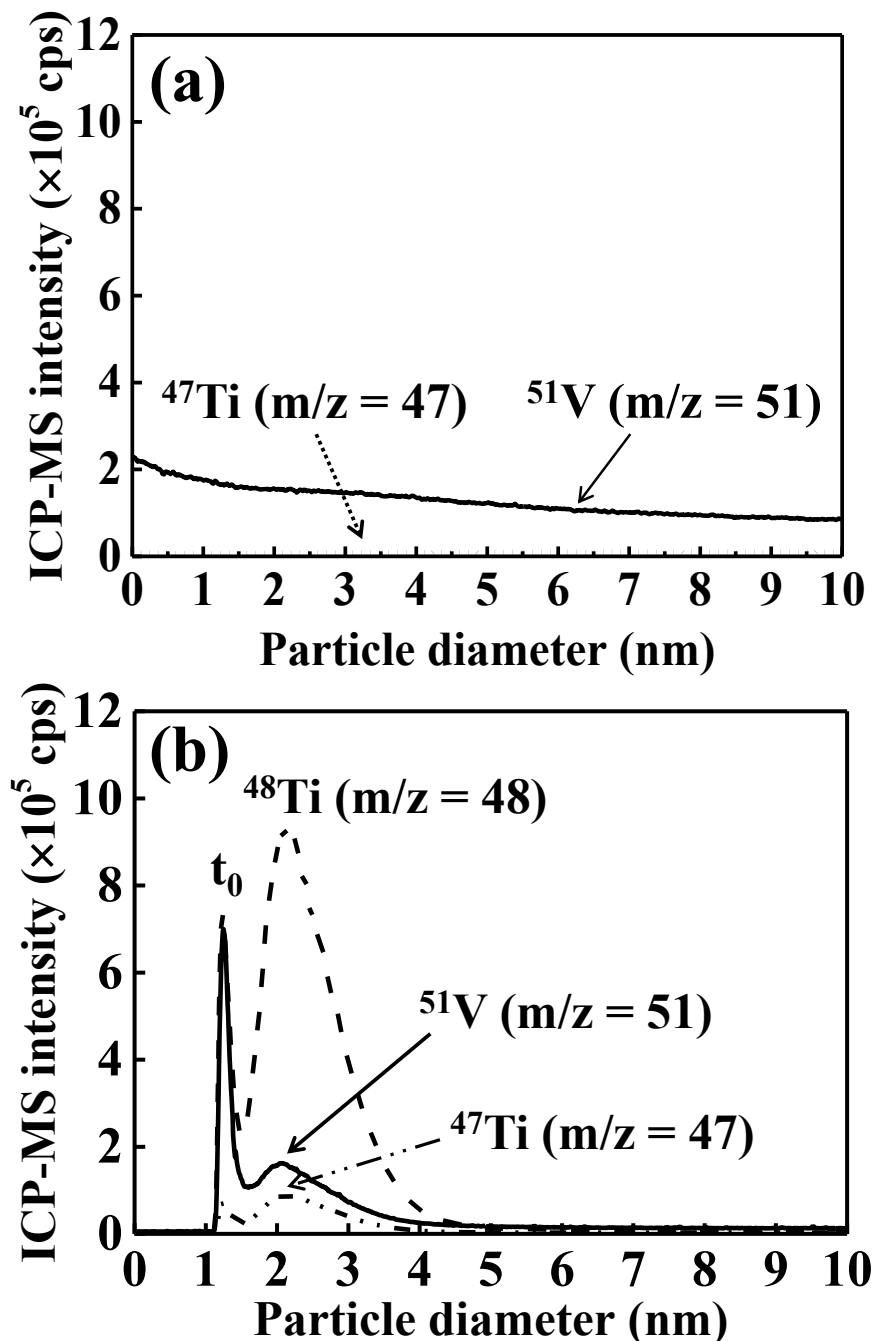
Fig. 5-8   Size distribution measurements of titanium and vanadium carbides in the steel sheet
via AF4-ICP-MS using (a) RC 5 kDa membrane with 1.73 mM SDS solution and
(b) RC 30 kDa membrane with 1.16 mM SC solution.

Chapter 5: Development of sulfur-free surfactant for titanium and vanadium nanoparticle characterization in steel using AF4-ICP-MS

Finally, it was considered whether these surfactants influenced the dispersion state of (Ti, V) C_2 and the interaction between the AF4 membrane in the solution. The suspensions of TiC and VC reagent powder were prepared by the addition into 1.73 mM SDS and 1.16 mM SC aqueous solutions. Each suspension was fully vortexed and sonicated to disperse particles. Then, the zeta potential of the carbides was measured using the laser Doppler electrophoresis method. Fig. 5-9 shows the results of the zeta potential of the carbides in each solution.
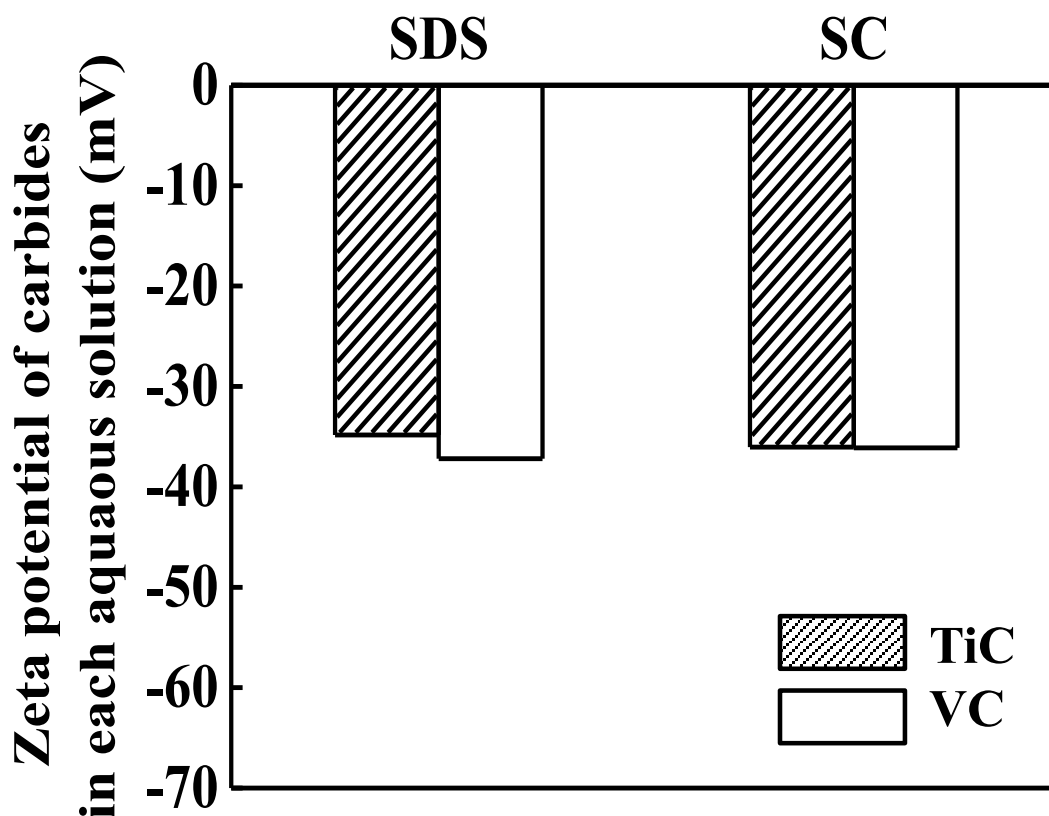
Fig. 5-9   Zeta potential of titanium carbides (TiC) and vanadium carbides (VC) using SDS and SC solutions. The left hatched bar showed TiC, the white bar showed VC. The concentration of SDS and SC was adjusted to 1.73 mM and 1.16 mM, respectively.

Each carbide particle had a zeta potential from −30 to −50 mV with the addition of surfactants. Additionally, the hydrodynamic diameter of TiC and VC reagents was measured in both aqueous solution and SPEED solution with 1.16 mM SC by DLS. The hydrodynamic diameter of carbides in both solutions was almost consistent to the primary diameter of reagent powder, as shown in Fig. 5-10. Therefore, both the carbides were considered to be dispersed by the anionic surfactants in both solutions in a similar manner to AuNPs. Furthermore, it was discovered that SC was an effective surfactant for TiC and VC detection using AF4−ICP-MS.

Fig. 5-10   Hydrodynamic diameter of TiC and VC reagents measured by DLS in ultrapure water (white bar) and SPEED solution (left hatched bar) with 1.16 mM SC. The measurements were repeated twice. The error bar showed standard deviation.
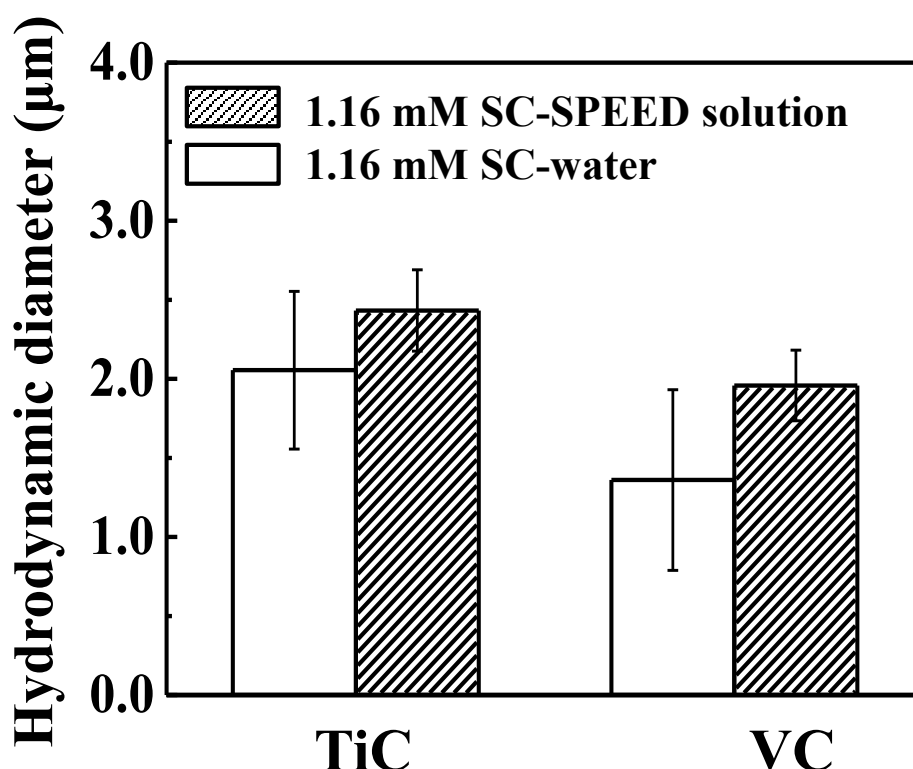
5.4   Conclusions

The optimum selection method of the surfactant used in AF4-ICP-MS to sensitively detect TiC and VC in steels was developed herein. The best approach to measure target nanoparticles using AF4-ICP-MS is summarized as follows.

(1) Zeta potential of the particles was controlled above −30 mV for avoiding particle aggregation.

(2) For AF4-ICP-MS, zeta potential of the membrane in AF4 separation channel from −20 to −30 mV was preferable to prevent the particle adhesion on the membrane surface.

(3) The AF4-ICP-MS carrier solution must be selected to avoid mass spectral interference between component elements of the target nanoparticles and polyatomic ion species generated from their matrices.

Only SC, selected as the sulfur-free surfactant, could detect the trace amounts of (Ti, V) C in steels by removing the sulfur matrix from the sample solution. Thus, the developed sulfur-free surfactant was useful for the AF4–ICP-MS analysis of micro-alloy (titanium and vanadium) precipitates in steels.

Chapter 5: Development of sulfur-free surfactant for titanium and vanadium nanoparticle characterization in steel using AF4-ICP-MS

5.5   References

1. C. Klinkenberg, K. Hulka, and W. Bleck: *Steel Res. Int.*, **75**(2004), 744.

2. P. Michaud, D. Delagnes, P. Lamesle, M.H. Mathon, and C. Levaillant: *Acta Materialia*, **55**(2007), 4877.

3. C.Y. Chen, H.W. Yen, F.H. Kao, W.C. Li, C.Y. Huang, J.R. Yang, and S.H. Wang: *Mater. Sci. Eng. A*, **499**(2009), 162.

4. T. W. May and R. H. Wiedmeyer: *At. Spectrosc.*, **19**(1998), 150.

5. J. Takahashi and N. Yamada: *Bunseki Kagaku*, **53**(2004), 1257.

6. S. Mori and H. Okamoto: *Flotation*, **27**(1980), 117.

7. L. A. Giannuzzi, J. L. Drown, S. R. Brown, R. B. Irwin, and F. A. Stevie: *Microsc. Res. Tech.*, **41**(1998), 285.

8. C. A. Sötebier, F. S. Bierkandt, S. Rades, N. Jakubowski, U. Panne, and S. M. Weidner: *J. Anal. At. Spectrom.*, **30**(2015), 2214.

9. N. Bendixen, S. Losert, C. Adlhart, M. Lattuada, and A. Ulrich, *J. Chromatogr. A*, **1334**(2014), 92.

10. T. K. Mudalige, H. Qu, and S. W. Linder: *Langmuir*, **33**(2017), 1442.

11. J. C. Giddings: *Science*, **260**(1993), 1456.

12. H. Goretzki, *Phys. Status Solidi B*, **20**(1967), 141.

Chapter 6

General conclusions

Chapter 6: General conclusions

General conclusions

The major objective of this research is to develop the analytical method for the size distribution and number concentration of precipitates whose sizes are ranged from several nanometers to several hundred nanometers in steels. There are some improvement and findings for the pre-treatment for the extraction of precipitates from steel using SPEED method in Chapter 2 and the analytical method for the precipitates in steels using AF4-ICP-MS in Chapter 3, 4, and 5. The summary was descried as follows.

In Chapter 2, the analysis method of chemically unstable sulfides in steels was investigated. There were problems to extract the copper sulfides (Cu_xS) stably from steels using SPEED method with 4% MS electrolyte which was recommended in the past report. It was reported that because MnS stable in the steel matrix becomes easily decomposable in an aqueous solution and Cu^{2+} ion easily forms sulfides (named as artificial sulfides) in an aqueous solution with sulfur, it reacts with MnS in a methanol (non-aqueous solvent) electrolyte, which has the characteristics similar to an aqueous solution, resulting in forming artificial sulfides. From our research about the mechanism of artificial sulfides formation, it was found that the greater the differences in the δpK_{sp} value of the sulfide solubility product, the more readily metal ions react with MnS. Moreover, in order to prevent the formation reaction of artificial sulfides, the electrolyte with the addition of a Cu ion chelating agent was developed (named as CUSH (Cu ion selective holding) electrolyte). This Cu ion chelating agent was confirmed to be effective for the above purpose. Additionally, the combination use of bubbling by argon gas was more effective in increasing the effectiveness of Cu ion chelating agents for the quantitative analysis. Therefore, using the developed CUSH electrolyte, it could be observed fine particles *in-situ* in the steel matrix and could be accurately and quantitatively analyzed the particle size and composition of sulfides.

In Chapter 3, prior to the application to steels, the accuracy of size measurement by AF4 was investigated using gold nanoparticles (AuNPs). The measurement accuracy was confirmed by comparing the AF4 results with those of TEM and small-angle X-ray scattering (SAXS). As a result, it was revealed that the average size measured by AF4 was almost same as TEM and SAXS. Additionally, for AF4 analysis, a peak broadening phenomenon occurred because of the diffusion of particles in the AF4 separation channel. Based on these results, the correction method for the FWHM of size distribution measured by AF4 analysis was developed using a broadening coefficient defined as the FWHM ratio of AF4/TEM. When the broadening coefficient was applied to the evaluation using AF4 for NbC in steels, it was effective for measuring semi-quantitatively their size and amounts. Therefore the applicability of the FWHM correction method in the AF4 analysis was confirmed.

Chapter 6: General conclusions

In Chapter 4, the detection efficiency for nanoparticles was considered in the case of the application of steel samples to AF4-ICP-MS analysis. It is known that the solid sample direct introduction to ICP has lower efficiency than that of liquid sample. Additionally, sample introduction method itself is very low efficiency. In order to improve the sample introduction efficiency of nanoparticles to ICP, it was investigated whether the Mistral Desolvation (MD) method which has heating-cooling process was effective to the above purpose. First, the selective evaporation and condensation was achieved by MD method, resulting in the dramatic increase of the aerosols smaller than 10 μm and 4.7 times improvement of the liquid sample introduction efficiency. Next, the measurement accuracy of MD method was investigated by applying the analysis of the Japanese Iron and Steel Certified Reference Materials. It was revealed that the measurement result by MD-ICP-AES agrees well with the certified values. Additionally, MD-ICP-AES provides that the high sensitivity of a factor of about 3 times can be achievable even under the condition that the sample consumption amount is reduced to one ninth. From these results, it was suggested that the sample dissolution amount may be reduced to about one twenty-seventh relative to the conventional method. Finally, it was also showed that the MD-ICP-MS analysis could improve the sample introduction efficiency for nanoparticle dispersed samples. The tested AuNPs are introduced over 85% efficiency. From these results, the quantification analysis for particles over 100 nm using AF4-ICP-MS was expected to become more accurate.

In Chapter 5, the application of AF4-ICP-MS analysis for precipitates in steels was investigated. In case of nanocarbides including titanium and vanadium, AF4-ICP-MS analysis has certain problem regarding the spectral interference due to sulfur matrix of surfactants. For the actual detection of titanium carbides (TiC) and vanadium carbides (VC) and their size distribution measurement *via* AF4-ICP-MS, sulfur-free surfactants must be used to disperse each particle in the solution. To determine the optimum surfactant, several surfactants were investigated for the separation ability in AF4 using AuNPs with different particle sizes. As a result, it was revealed that the zeta potential of the particles and the membrane in AF4 separation channel has a preferable range to achieve good separations. The former is above −30 mV for avoiding particle aggregation and the latter is from −20 to −30 mV for prevention of the particle adhesion on the membrane surface. Additionally, the AF4-ICP-MS carrier solution must be selected to avoid mass spectral interference between component elements of the target nanoparticles and polyatomic ion species generated from their matrices. Only sodium cholate, selected as the sulfur-free surfactant with proper zeta potential, could detect the trace amounts of (Ti, V) C in steels by removing the sulfur matrix from the sample solution. Thus, the developed sulfur-free surfactant was useful for the AF4–ICP-MS analysis of micro-alloy (titanium and vanadium) precipitates in steels.

Chapter 6: General conclusions

Publications

This present thesis is based on the works contained in following;

1. K. Mizukami, D. Itabashi, M. Aimoto, and M. Nishifuji, *ISIJ International*, **60**(2020), 1, 120-127. (Chapter 2)

2. D. Itabashi, R. Murao, S. Taniguchi, K. Mizukami, H. Takagi, and M. Kimura, *ISIJ International*, **60**(2020), 5, to be published. (Chapter 3)

3. D. Itabashi, K. Mizukami, M. Aimoto, and M. Nishifuji, *ISIJ International*, **58**(2018), 6, 1061-1068. (Chapter 4)

4. D. Itabashi, K. Mizukami, S. Taniguchi, M. Nishifuji, and H. Kamiya, *Anal. Sci.*, **35**(2019), 9, 995-1001. (Chapter 5)